NASA-CR-201543

PENNSTATE

1855

FINAL REPORT

PROPULSION ENGINEERING RESEARCH CENTER

FUNDAMENTAL PHENOMENA ON FUEL DECOMPOSITION AND BOUNDARY-LAYER COMBUSTION PROCESSES WITH APPLICATIONS TO HYBRID ROCKET MOTORS

Sponsored by
NASA Marshall Space Flight Center
MSFC, Alabama 35812
Contract No: NAS8-39945

Prepared by
Part I: Kenneth K. Kuo, Yeu-Cherng Lu, Martin J. Chiaverini,
David K. Johnson, Nadir Serin, and Grant A. Risha
Part II: Charles L. Merkle and Sankaran Venkateswaran

A UNIVERSITY SPACE ENGINEERING RESEARCH CENTER

June 30, 1996

106 RESEARCH BUILDING EAST
UNIVERSITY PARK, PENNSYLVANIA 16801

Final Report

On

FUNDAMENTAL PHENOMENA ON FUEL DECOMPOSITION AND BOUNDARY-LAYER COMBUSTION PROCESSES WITH APPLICATIONS TO HYBRID ROCKET MOTORS

(Contract No: NAS8-39945)

Submitted to

Mr. Roger Harwell
NASA Marshall Space Flight Center
Mail Code: PT-21
MSFC, Alabama 35812

Prepared by

**Part I: Kenneth K. Kuo, Yeu-Cherng Lu, Martin J. Chiaverini
David K. Johnson, Nadir Serin, and Grant A. Risha**

Part II: Charles L. Merkle and Sankaran Venkateswaran

Propulsion Engineering Research Center
Mechanical Engineering Department
The Pennsylvania State University
University Park, PA 16802

June 30, 1996

ACKNOWLEDGMENT

The authors would like to thank NASA/MSFC for funding this work under Contract No. NAS 8–39945. The support and encouragement of Mr. Roger Harwell of MSFC and Mr. Marion D. Kitchens of NASA Headquarters are highly appreciated. We would also like to thank Mr. Les Tepe of the Phillips Lab and Dr. David M. Mann of the Army Research Office for supporting the purchase of the Ultrasonic Measurement System from ONERA, France. Under the NATO/AGARD sponsorship, the help of Mr. Franck Cauty of ONERA in the technology transfer of the ultrasonic pulse–echo technique to the research team is also greatly appreciated. The authors also wish to thank TUBITAK–SAGE of Turkey and the NATO Fellowship Program for sponsoring Mr. Nadir Serin for his participation in this project at PSU. We are highly appreciative of the NASA Traineeship to support Mr. Martin Chiaverini's doctoral research activities on hybrid rocket propulsion. The assistance of Mr. George Harting, an Air Force Palace Knight graduate student, in setting up the test facility is very much appreciated.

PART I: EXPERIMENTAL INVESTIGATION

Kenneth K. Kuo, Yeu-Cherng Lu, Martin J. Chiaverini
Nadir Serin, David K. Johnson, and Grant A. Risha
Propulsion Engineering Research Center
The Pennsylvania State University
University Park, PA 16802

PART I: EXPERIMENTAL INVESTIGATION

TABLE OF CONTENTS

LIST OF FIGURES

LIST OF TABLES

NOMENCLATURE

Symbols	
A	area
A^*	throat area
B	blowing parameter
c	speed of sound
c_f	skin friction coeff.
C_H	Stanton number
D	diameter
E_a	activation energy
f_m	fuel/air mixture ratio
G	mass flux
h	port height
H	heat of reaction
ΔH	total heat of vaporization
k	rate constant
K	concentration
Le	Lewis number
N_p	particle number density
O/F	oxidizer to fuel mass ratio
P	pressure
P_r	Prandtl number
Q	heat flux
r	regression rate
R	gas constant
R_u	universal gas constant
Re_x	length Reynolds number
Re_D	diameter Reynolds number
t	time
T	temperature
u	velocity
V	voltage
w	web thickness
x	axial location
Y	mass fraction
z	depth

Greek Symbols	
ρ	density
μ	viscosity
κ	absorption coeff
ε	emissivity
σ	Stefan Boltzmann const
γ	ratio of specific heats
τ	propagation time

Subscripts	
c	convective
e	boundary layer edge
f	fuel
g	gas
o	oxidizer
rad	radiative
x	axial
w	wall
∞	freestream

I.1 Introduction

All chemically powered rockets and spacecraft produce thrust in the same basic manner: chemical reactions between the propellant components release thermal energy in the combustion chamber which is then converted to kinetic energy as the combustion products expand through the nozzle. The overall thrust level and efficiency of the rocket depend to a large degree on the specific choice of fuel and oxidizer, which are the two reacting components of the chemical propulsion system. When both the fuel and oxidizer are stored in liquid form, the rocket is called a liquid bi–propellant rocket. Liquid oxygen (LOX), hydrogen peroxide, and nitrogen tetroxide represent commonly used liquid oxidizers, while liquid hydrogen (LH_2) and kerosene are often employed as liquid fuels. When the fuel and oxidizer are combined in solid form, either chemically in the case of homogenous propellants, or physically in the case of heterogeneous propellants, the rocket is called a solid propellant rocket. Ammonium perchlorate and ammonium nitrate are commonly used oxidizers in solid form, while solid fuels include polyethylene (PE) and Hydroxyl–terminated polybutadiene (HTPB), which is often loaded with small aluminum particles to enhance burning [I.1].

Traditionally, nearly all rockets that produce thrust via chemical reactions have utilized one of the two above–mentioned systems: liquid propellant systems or solid propellant systems. However, a third type of chemical propellant system stores the fuel in one phase and the oxidizer in another, and is called the liquid–solid, or, more commonly, the hybrid rocket. The hybrid rocket represents a type of amalgam of the liquid and solid propellant rockets, yet it has important and distinguishing features common to neither of the other systems. Figure I.1.1 illustrates the basic differences between these three types of chemically–powered rocket systems.

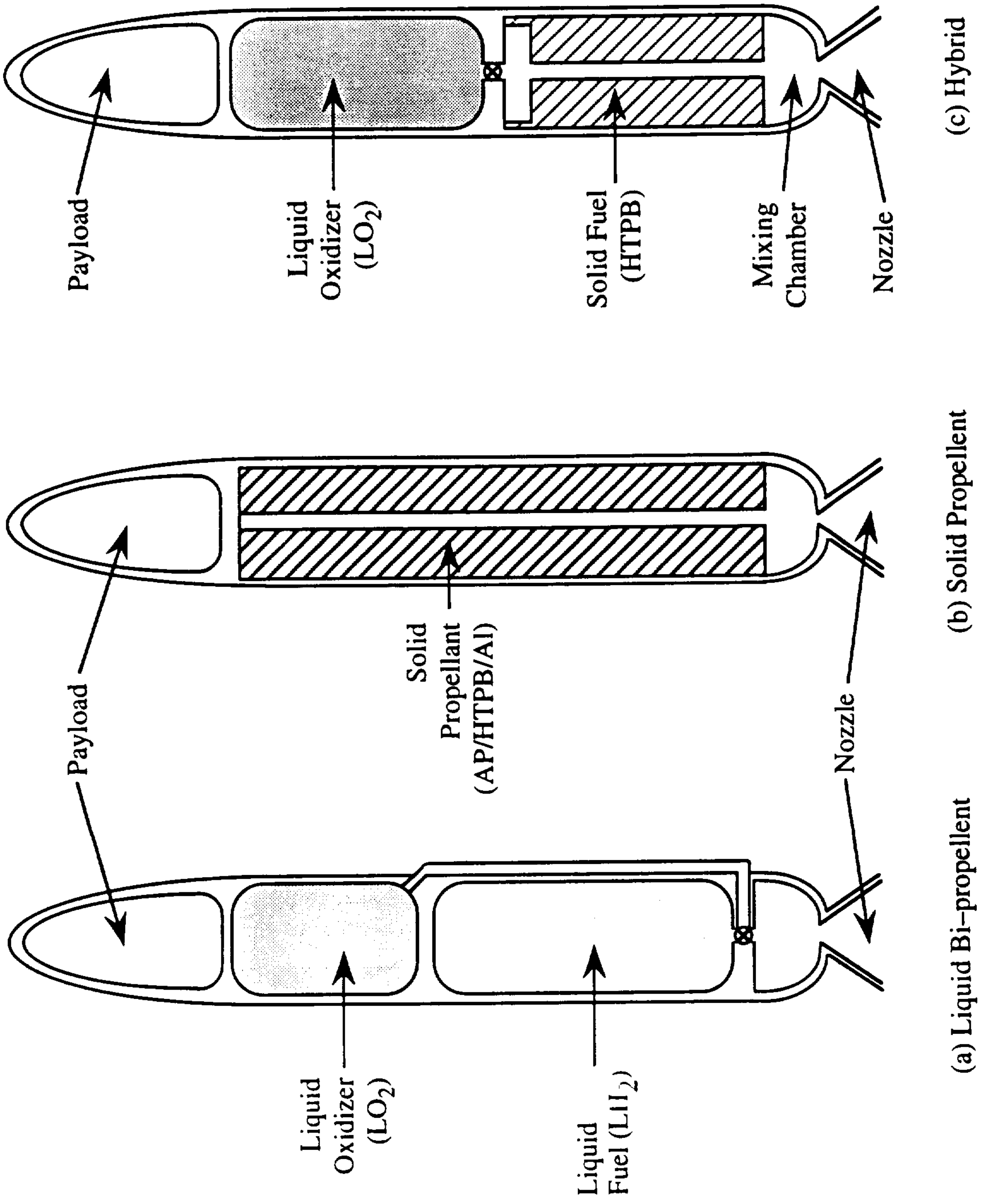

Figure I.1.1 Three types of chemically–powered rockets

Several different types of hybrid rockets exist, and are shown in Figure. I.1.2. The classical hybrid rocket employs a solid fuel grain and a liquid oxidizer [I.2]. The liquid oxidizer is injected into the head–end of the solid fuel grain through a pre–combustion chamber which serves to vaporize the oxidizer and allow it to enter the combustion port in a non–preferential manner. The pyrolyzed gaseous fuel and oxidizer mix and react along the length of the fuel grain and undergo final mixing in the aft combustion chamber. The hot product gases are then expelled out the nozzle to generate thrust. The reverse hybrid motor shown in Fig. I.1.2b works in much the same manner as the classical hybrid except that a liquid fuel and a solid oxidizer react to form the combustion products. Generally, the classical hybrid requires a total liquid mass to solid mass ratio of about 2, while the reverse configuration has a mass ratio of about 0.5 [I.2]. In the gas generator version, shown in Fig. I.1.2c, the solid fuel grain is loaded with a small amount of solid oxidizer, forming a very fuel–rich solid propellant. Oxidizer is then injected into the afterburner section to mix and burn with the fuel–rich gases generated by the solid grain. Finally, the system shown in Fig. I.1.2d combines aspects of the classical and gas–generator hybrids as oxidizer is injected into both the head–end of the fuel grain and the aft mixing chamber. Other configurations, such as a reverse gas generator using solid oxidizer and liquid fuel, are also possible [I.2].

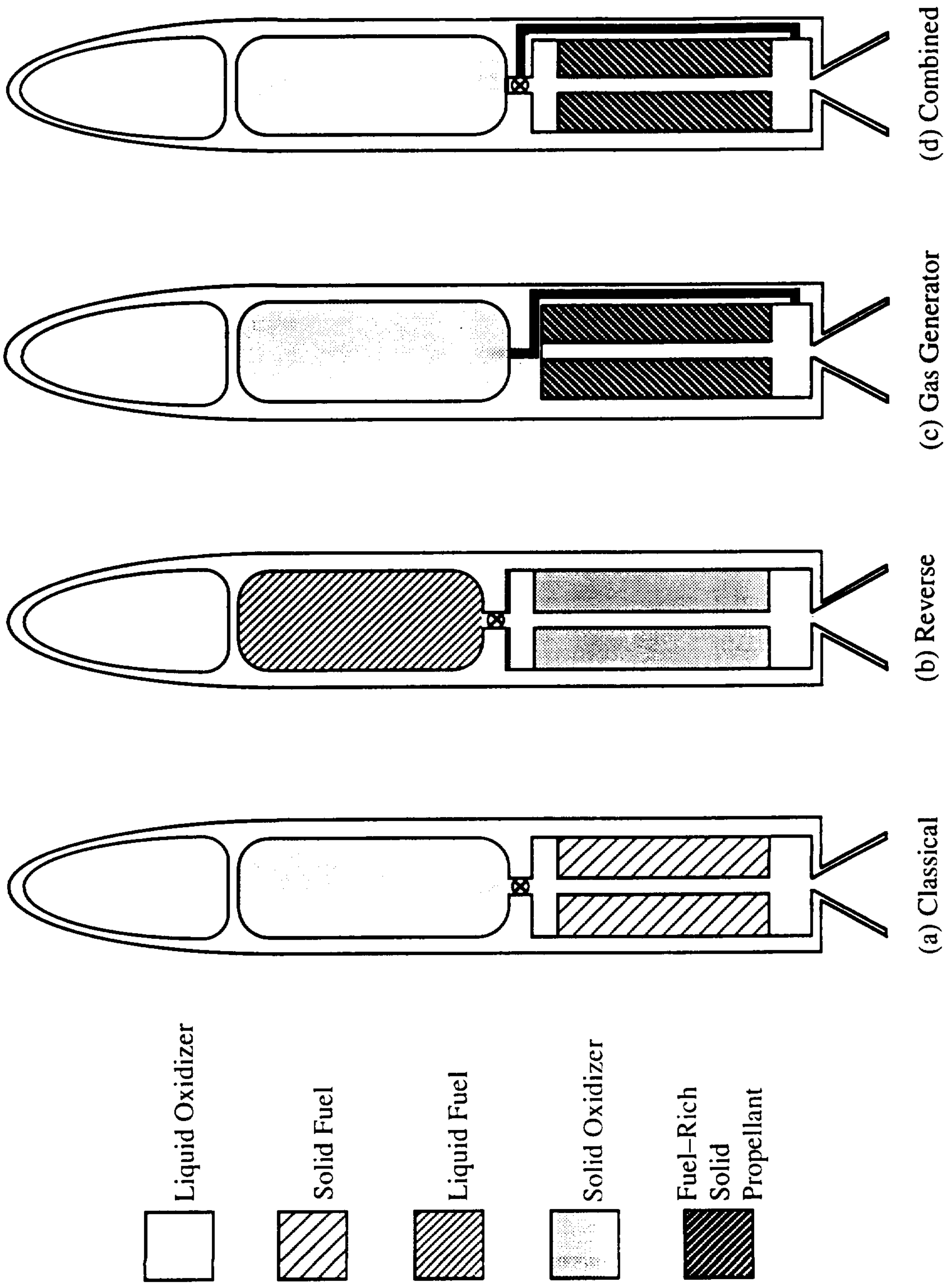

Figure I.1.2 Four different design configurations of hybrid rockets

Of all the concepts shown in Fig. I.1.2 the classical hybrid rocket has received the most attention and will be the focus of this work. Because they store fuel and oxidizer in separate phases, classical hybrid systems offer several important advantages over their liquid and solid rocket counterparts that make them attractive alternatives for commercial, military, and scientific applications. First, unlike solid propellant rockets, hybrid rockets are insensitive to cracks and imperfections in the solid fuel grain because, as will be discussed later, very little oxidizer actually reaches the fuel surface. Therefore, hybrids are much safer than solid–propellant rockets [I.3]. In addition, solid fuels are not hazardous for storage and transportation, unlike liquid fuels such as hydrogen, which is very volatile. Second, because only the oxidizer is stored in liquid form, hybrids require only half as much feed–system hardware as liquid propellant rockets. This gives them improved reliability over liquid propellant rockets. Third, hybrid rockets can easily be throttled for thrust control, maneuvering, motor shutdown and restart by adjusting only the oxidizer flow while avoiding the necessity of matching hydraulic characteristics with the fuel, as must be done for liquid propellant rockets. Fourth, the solid–phase fuel provides a convenient and efficient media for the addition of a variety of additives for purposes such as plume signature tailoring for military applications and metal particles for high–energy missions [I.3]. Fifth, hybrid rockets pose almost no explosion hazard during manufacture, transport, ground–test, and storage since the fuel and oxidizer are separated both physically and by phase. This arrangement also allows for easier and safer clean–up in the event of an oxidizer spill. Finally, hybrid rockets, as opposed to solid rockets, can have environmentally clean designs without hydrogen chloride, aluminum oxide, etc... in their exhaust. Because of their inherent safety, hybrid rockets should be very economic to both manufacture and launch [I.4].

From a performance standpoint, hybrid rockets are comparable to both liquid and solid–propellant rockets [I.1]. As shown in Table I.1.1, hybrid rockets typically have greater specific impulse than solid rockets and greater density specific impulse than liquid rockets. The values for common propellants are shown in parentheses. Though hybrid rockets usually have slightly lower specific impulse than the best liquid rockets, high–energy combinations such as beryllium–loaded HTPB fuel and liquid FLOX (combination of fluorine and oxygen) may produce Isp's in the neighborhood of 500 seconds. This fuel/oxidizer system could not be used during Earth–based launch because of toxicity limitations, but an upper stage could employ such propellant combinations to optimize performance [I.4].

Table I.1.1 Performance of chemical rocket systems

System	Isp (sec)	ρ Isp (g–s/cm^3)
Liquid Bi–Propellant	260–410 (LOX/H_2: 390)	100–430 (LOX/H2: 100)
Classic Hybrid	280–380 (LOX/HTPB: 330)	300–520 (LOX/HTPB: 350)
Solid Propellant	190–270 (AP/HTPB: 270)	290–470 (AP/HTPB: 470)

Despite the safety and performance advantages discussed above, and by what can perhaps best be described as an "accident of history" [I.3], large–scale rocket development in the 20th century has focused almost entirely on either all–liquid propellant or all–solid propellant rockets. However, the classical hybrid rocket is not a particularly recent idea; indeed, the concept of storing the fuel and oxidizer separately was explored early in this century [I.3].

During the late 1930's to the late 1950's several investigations were conducted on hybrid rockets, mainly in an attempt to prove the feasibility of using a fuel and oxidizer separated both physically and by phase. According to Green [I.2], Leonid Andrussow, a Russian cavalry officer in World War I, may have been the first person to conceive the idea of a propellant consisting of both liquid and solid components around 1937. This liquid/solid propellant was later called *lithergol* (from the Greek *lithos*, stone or solid and, *ergon*, work, and the Latin, *oleum*, or oil) by Wolfgang Noeggerath. Between 1938 and 1941, Noggerath was successful in constructing a test motor using a series of perforated coal disks for the solid fuel and gaseous nitrous oxide for the oxidizer. Utilizing a small charge of gunpowder for an igniter, his motor achieved thrust levels of 500 to 1000 N for up to 120 seconds [I.2].

Smith and Gordon of the California Rocket Society designed, built, and static–tested a hybrid rocket during 1938–1941. They also used a carbon as the solid fuel in the form of a bar and gaseous oxygen as the oxidizer. The chamber pressure varied between 100–300 psi, and specific impulses of about 160 sec were achieved [I.2].

Around this time in Germany, Oberth conducted research on a hybrid rocket which used liquid oxygen and graphite as a fuel, but ultimately failed due to the relatively low burning rate of graphite.

During the mid 1940's, the Pacific Rocket Society built a hybrid rocket and performed several static tests using LOX and such eclectic fuels as wood, wax, and rubber. After a number of trial and error test, the Society built and flew a LOX/rubber hybrid rocket in June of 1951 that reached an estimated altitude of 30,000 feet [I.3].

During 1946, Bartel and Rannie studied solid fuel ramjets (which is very similar to a hybrid rocket motor) fuels at the Jet Propulsion Laboratory. Like previous investigators, they also studied the use of carbon as a solid fuel. More importantly, they provided the first theoretical treatment of hybrid combustion, as discussed later [I.2].

Based upon Altman [I.3], Moore and Berman, two investigators at General Electric, performed a series of experiments in the late 1940's that led to the discovery of several important characteristics of hybrid rockets that would eventually be substantiated in later years. Moore and Berman used a hydrogen peroxide oxidizer and a polyethylene solid fuel in a tube burner. They concluded that 1) the fuel grain burned uniformly in the longitudinal direction, 2) cracks in the fuel grain had no effect on combustion (a conclusion also reached by the Pacific Rocket Society), 3) the fuel grain acted as a flameholder so combustion was stable, and 4) throttling could be achieved using a single valve. They also discovered that hydrogen peroxide was not suitable for hybrid rockets because of its inherent thermal instability [I.3].

In 1952, Dembrow and Pompa performed the first experiments on the inverse hybrid rocket configuration, using naphtha (petroleum ether) as the liquid fuel and several solid oxidizers including $KClO_4$, NH_4ClO_4, and NH_4NO_3 [I.2]. Reverse hybrid rockets were also investigated by several groups up through the 1960's. A program at Johns Hopkins University utilized liquid JP hydrocarbon fuel and ammonium nitrate as the solid oxidizer. Other investigators at Thiokol and United Technology's Chemical Systems Division used liquid hydrazine fuels and solid oxidizers of ammonium perchlorate, hydrazinium diperchlorate, and nitronium perchlorate. Unfortunately, none of the reverse hybrid systems seemed practical, and the research was terminated in the early 1960's [I.3].

During the 1960's, ONERA in France and Volvo–Flygmotor in Sweden began investigations of hybrid rockets that eventually led to the development of sounding rockets. The rockets studied by ONERA utilized red fuming nitric acid (RFNA) for the oxidizer and a solid fuel composed of metatoluene, diamine, and nylon. These two components are hypergolic, meaning they ignite on contact. A rocket based on this motor was first flown in April of 1964 and three times in June of 1965. An additional four flights were made in November of 1967 using a slightly improved design. All eight flights reached altitudes of over 100 km and were powered by LEX–02 engines delivering thrust over a range of 2 to 10 kN [I.4].

The Swedish rocket was also based on a hypergolic propellant, composed of nitric acid and a fuel called Tagaform. This vehicle made a successful flight in 1969, attaining an altitude of 80 km [I.4].

One of the most successful application of hybrid rocket technology in the United States occurred around the time of the European flight tests. Working under an Air Force contract, United Technology Center and Beech Aircraft developed the Sandpiper, a target drone utilizing a combination of MON–25 (25% NO, 75% N_2O_4) for the oxidizer and a solid fuel composed of polymethylmetacrylate (PMMA) and magnesium (Mg). Just 18 months after the start of the program, the Sandpiper made six successful flights in January of 1968. The Sandpiper was designed to be launched from an aircraft and fly more than 100 miles at several altitudes and Mach numbers. It had a thrust duration of 300 seconds and could be throttled over an 8:1 range [I.3].

A second target drone called the HAST (High Altitude Supersonic Target) was designed later for a second Air Force program. The propellant was changed to IRFNA (inhibited red fuming nitric acid) and PMMA/Pb. The vehicle's thrust was controlled by throttling over a 10:1 range. A later version of this vehicle built by Teledyne Ryan was successfully completed in the mid–1980's and cruised at Mach 4 at an altitude of 30 km.

Several hybrid research programs were conducted in Germany during the 1970's. Initial efforts at DFVLR (later called the DLR) in Lampolshausen focused on space engines using FLOX and polyethylene, lithium, and lithium hydride solid fuels. Though specific impulses of 340 to 370 seconds were achieved, the research was terminated because these engines could not compete with high–performance liquid rocket engines. After this initial program, research then focused on storable systems using RFNA or nitrogen tetroxide oxidizers and metal–loaded solid fuels of polybutadiene, polyethylene, and PMMA.

In the mid 1980's, several events occurred which increased the propulsion community's interest in large–scale hybrid rocket research and development in the United States. First, growing competition in the communication satellite launching industry, both in the United States and worldwide, stimulated the search for a low–cost alternative to the existing liquid and solid rocket boosters. Second, the well–publicized catastrophic failure of the Space Shuttle Challenger, as well as the loss of a Titan III booster, in 1986, led NASA to sponsor a study of the use of hybrids as Shuttle strap–on boosters [I.3].

The American Rocket Company (Amroc) began development of hybrid rocket boosters in 1985 with a research engine, the H–50, that used liquid oxygen and polybutadiene fuel. The H–50 produced a thrust of 22,000 N. Thereafter, Amroc built successively larger motors, culminating with the H–1800 in 1993. The H–1800 was a rather large motor capable of producing thrust of up to 1.16 MN. This engine was first ground–tested on January 22, 1993 during a 15 sec firing, then again on February 17, 1993. The second test demonstrated the hybrid's ability to be shut down and restarted [I.4].

One of the most recent and active government–industry effort to promote hybrid rocket propulsion was the Joint Independent Research and Development (JIRAD) Team for Hybrid Propulsion Research, assembled in 1990. This group consisted of Amroc (now defunct), General Dynamics (later acquired by Martin Marietta), Martin Marietta (now Lockheed Martin), Rocketdyne, Thiokol, United Technologies, and NASA's Marshall Space Flight Center (MSFC). The goals of the JIRAD group were to develop hybrid boosters for the next generation of U.S. launch vehicles. During this program, a number of successful tests were conducted at NASA's Marshall Space Flight Center [I.4,I.15].

In July 1994, NASA awarded contracts to four teams under a program called Hybrid Propulsion Technology for Launch Vehicle Boosters. The work reported here represents the research activity conducted at the Pennsylvania State University on the fundamental combustion processes associated with hybrid rocket motors. At the Jet Propulsion Laboratory, Strand and his co–workers [I.6,I.7] performed a series of lab–scale slab burner tests to study combustion behavior of GOX and butadiene furl. Under relatively low pressure and mass flux conditions, the radiative energy flux was found to be quite important, on the order of 30% of the total energy flux.

In addition to the brief history of hybrid rocket development discussed above, several influential studies conducted during the 1960's warrant special mention because their results illustrate why further fundamental studies of hybrid combustion behavior are still required today.

In the early to mid 1960's, Marxman, Gilbert, Wooldridge, and Muzzy, working at United Technology Center in Sunnyvale, California, developed a singularly important heat–transfer limited regression rate model which suggested that the solid fuel regression rate depended mainly on convective and radiative heat transfer from the gas phase to the solid fuel surface. Described fully in [I.8], their regression rate equation showed that, in the absence of significant gas–phase radiation, the solid fuel regression rate was primarily a function of the local mass flux, G, and axial position, x, but not the motor pressure. They attempted to verify their theory with a limited number of experimental results.

At about the same time, Smoot and Price [I.9–I.11] conducted a large number of experiments using a lab–scale motor at what was then the Lockheed Propulsion Company in Redlands, California. They found that at low pressures ($p<150$ psi) the average regression rates showed little or no dependence on mass flux but strong dependence on pressure. They attempted to show that heterogeneous reactions on the solid fuel surface caused this behavior, an explanation that was later discounted by Muzzy [I.12]. It should be noted that Smoot and Price's experiments, though prolific, lied outside the range of practical hybrid rocket applications, where both flow rates and pressures would probably be several times greater than those of their labscale slab burner.

In the last three decades since Marxman et al [I.8,I.13,I.14] and Smoot and Price [I.9–I.11] performed their pioneering works, different theories, correlations, and numerical procedures have commonly been proposed to explain solid–fuel regression and burning behavior. Various schools have attributed the regression rate–limiting mechanism to different controlling parameters, including the rate of convective heat transfer from the flame to the solid–fuel burning surface, radiative heat–transfer rate to the surface, homogeneous reaction rates in the gas–phase, heterogeneous reaction rates on the fuel surface, rate of bond breaking of polymer chains in the solid fuel, and, quite recently by Brill [I.15,I.16], rate of desorption of polymer fragments from the fuel surface and into the gas phase. Though important observations and advancements have been made, the literature has historically lacked a sufficient amount of realistic empirical data for model validatiaon. In order to validate a comprehensive model, many detailed measurements are needed, including regression rate, fuel surface temperature and subsurface temperature profiles, species concentration profiles in the reacting boundary layer. Simultaneous measurement of these physical quantities are prohibitively difficult. Even accurate measurement of instantaneous regression rates is not always achievable. Some advanced instrumentations were developed. For example, Dijkstra and Korting [I.17] and Lengellé et al [I.18] used the ultrasound pulse–echo method for measuring the regression rate of solid fuel. Houser and Peck [I.19] used an interrupted burning technique for determining the regression rate of solid fuel.

The presence of so many different types of models and correlations gives strong justification for obtaining more detailed experimental data for model validation and regression behavior prediction. A more fundamental understanding of the complex processes involved in hybrid combustion is definitely needed in order to resolve the differences among various approaches and to develop a comprehensive theory. Furthermore, development of more reliable and accurate regression–rate correlations with applicability to broad ranges of operating conditions is needed for assisting the design of large–scale hybrid motors.

The work described in this report represents an attempt to meet some of these demands. The research program has focused on the following specific objectives: 1) determination of instantaneous and average solid fuel regression behavior under various operating conditions with different oxidizer mass flux, motor pressure, fuel formulation, and combustor port geometry, 2) measurement of solid fuel surface temperature and subsurface temperature profiles, 3) evaluation of the effects of several additives, including carbon black and ultra–fine aluminum powder, on burning behavior, 4) development of empirical correlations to relate regression rate to both operating conditions and port geometry, and 5) assembly of a database for validating the numerical model being developed at PSU.

After a review of some pertinent hybrid literature in Section I.2, the hybrid test rig, diagnostic devices, data acquisitions systems, and solid fuel are given a detailed description in Section I.3. Section I.4 presents sample motor pressure, solid fuel temperature, regression rate, and empirical correlation results and also discusses data reduction techniques. Finally, Section I.5 discusses conclusions of the current phase of the project and presents recommendations and plans for future work.

I.2 Review of Pertinent Hybrid Rocket Combustion Research

This section summarizes and discusses different types of regression rate models that have been developed by several researchers during previous investigations of hybrid rocket combustion. Various types of regression–rate analyzes can be loosely grouped into categories identified by the controlling mechanism such as heat–transfer limited analyzes, mass–diffusion limited analyzes, pressure dependent analyzes, gas–phase reaction limited analyzes, and solid–phase reaction limited analyzes. These analyzes are useful in guiding the development of correlations.

I.2.1: Heat and Mass Transfer Limited Regression Rate Models

I.2.1.1: Bartel and Rannie's Analysis

Perhaps the earliest analysis to consider most of the essential features of hybrid combustion was that of Bartel and Rannie [I.2]. Bartel and Rannie considered the one–dimensional axial flow of air through a tube of fuel. The turbulent air enters the tube (having diameter D) with a velocity U_o, density ρ_o, pressure p_o, and stagnation temperature T_o. Carbon was the fuel used. Bartel and Rannie thought that the diffusion or transport of oxygen to the fuel surface is the controlling mechanism for supporting the fuel regression process. They assumed that the mass addition due to fuel burning was negligible in comparison to the air mass flux down the tube length, and that fuel and oxygen were completely mixed at each station along the tube. However, they did not consider the location of the diffusion flame. By examining the rate of heat added to the gas flowing through an elemental cross section they obtained the following expression

$$m_f'' = (C_f G\, f_m/2)\exp(-2C_f x/D) \tag{I.2.1}$$

where m_f'' represents the mass burning rate of fuel per unit area (or $\rho_f r$), C_f the friction coefficient on the fuel surface, G the average mass flux down the tube, f_m the fuel/air ratio of the reaction, x the distance along the tube from the entrance, and D the tube inner diameter. According to this expression, the fuel burning rate decreases exponentially with axial position along the tube. They also used the well–known pipe flow correlation of friction coefficient with Reynolds number: [i.e., $C_f=0.046Re_D^{-0.2}$]. When this expression is substituted into Eq. (I.2.1), the familiar $G^{0.8}$ dependency is obtained, since Re_D can be written as GD/μ.

I.2.1.2: Emmons' Analysis

Emmons also obtained a solution for the boundary–layer combustion of a gaseous oxidizer flowing over a solid fuel surface, though he did not necessarily have in mind hybrid rocket propulsion as an application of the problem. Emmons assumed a laminar flame zone of finite thickness in the boundary layer [I.2]. He then transformed the energy, momentum, and species equations into similar Blasius–type equations by assuming unity Prandtl, Lewis, and Schmidt numbers. His exact numerical solution was

$$m_f'' = \rho_e u_e Y(B)/Re_x^{1/2} \tag{I.2.2}$$

where Y(B) is a function of the Spalding mass transfer number B (which Emmons calls the heat ratio) which can be defined for the present application as the ratio of the thermal energy of unit mass of the core flow to the thermal energy required at the surface to put unit mass of fuel into the boundary layer, or

$$B = [(Ko_e - Ko_s)H/n_o + c_p(T_e - T_s)]/[L + c_s(T_s - T_i)] \tag{I.2.3}$$

where Ko is the oxidizer concentration, H the heat of reaction per mass of fuel, n_o the O/F ratio, T the temperature, L the heat of phase change, c_p the specific heat of the gas, and c_s the specific heat of the solid, the subscript e indicates the outer edge of the boundary layer, subscripts s and i represent the surface and initial conditions. For the range of $0.5 < B < 5$, Emmons found

$$m_f'' = \rho_e u_e[0.18 + \log10(B + 0.7)]/Re_x^{1/2} \tag{I.2.4}$$

where $\rho_e u_e = G$. Notice from this expression that m_f'' is proportional to $G^{0.5}$ due to the assumed laminar nature of the flow. The boundary layer involved in practical hybrid systems is probably mostly turbulent due to the de–stabilizing influence of mass injection at the solid surface as well as the high Reynolds number of the oxidizer flow.

I.2.1.3: Houser and Peck's Analysis

Houser and Peck, in 1963, made a useful contribution with their measurement of the *instantaneous* regression rate of a cylindrical hybrid fuel grain of several polymeric fuels burning with GOX [I.19]. They burned cylindrical blocks of varying total length having an initial inner diameter of 1 in. Most tests were conducted with PMMA (plexiglas) as the solid fuel. They also used chromel–alumel thermocouples of either 25 or 15 μm diameter. The instantaneous regression rates were deduced at several axial positions at various flow rates, using an interrupted burning technique. Houser and Peck found that the instantaneous inner radius of the combustor port followed a double–power law formulations of the form

$$\mathrm{rad}(t) = A + Bt^{0.8} + Ct^{0.3} \tag{I.2.5}$$

so that the instantaneous regression rate at a particular axial location can be found by taking the time–derivative of Eq. (I.2.5)

$$r(t) = 0.8B/t^{0.2} + 0.3C/t^{0.7} \tag{I.2.6}$$

No theoretical significance was given to this equation. The researchers made no attempt to account for the surface heat–up time just following ignition, and their best–fit equation given by Eq. (I.2.6) does not apply at zero time where the regression rate goes to infinity. Also, Houser and Peck were unable to obtain accurate data for times less than 10 seconds. Despite these shortcomings, they were possibly the first to recognize the importance of obtaining the regression rates as a function of both axial position and time. Houser and Peck also showed experimentally that the regression rate decreases with time due to an increase in port area (and corresponding decrease in port mass flux) and increases with axial distance due to an increase in mass flux from fuel addition. Furthermore, they showed that the measured fuel surface temperatures were the same for both translucent fuel grains and opaque fuel grains processed with carbon black. These particular results will be substantiated later in this report.

I.2.1.4: Marxman, Gilbert, Wooldridge, and Muzzy's Analysis

Probably the most thorough and influential heat–transfer theory of hybrid combustion was developed by Marxman, Gilbert, Wooldridge, and Muzzy at the United Technology Center in Sunnyvale, California during the early to mid 1960's. References [I.8] and [I.13] discuss their analysis and experiments in detail. According to their postulation, a flame sheet is established in the boundary layer which serves to separate the boundary layer into two zones: one zone above the flame where the temperature and velocity gradients are opposite in direction and one zone below the flame where the gradients are in the same direction. The upper zone is oxidizer rich while the lower zone is fuel rich. The flame occurs at a position where the concentrations of each are sufficient for combustion to occur [I.8]. Since Marxman and Gilbert believed that heat transfer from the flame to the fuel surface was the controlling mechanism of hybrid combustion, they applied an energy flux balance at the fuel surface to obtain an expression for the fuel regression rate. The energy balance led to the equation

$$\rho_f r = Q_w / \Delta H \tag{I.2.7}$$

where ρ_f is the solid fuel density, r the regression rate, Q_w the heat transfer per unit area to the wall (which may include both convective and radiative components), and ΔH the total energy required to heat the solid fuel from its initial temperature to the surface temperature and to decompose and vaporize a unit mass of solid fuel. Physically, Eq. (I.2.7) states that the enthalpy "blowing" from the fuel surface into the gas–phase equals the total heat flux incident on the fuel surface. This analysis ignores both thermal radiation transmitted and heat conducted into the solid fuel.

In order to derive a useful equation for the regression rate from Eq. (I.2.7), Marxman and Gilbert made several important simplifications to the problem. First, they assumed that the boundary–layer flow was turbulent over most of its length due to the de–stabilizing effect of fuel injection at the surface. Second, they reason that Reynolds analogy (which states that the transport of energy and momentum in a boundary layer are similar) and Le=Pr=1 hold in both the upper and lower boundary layer zones, but not necessarily in the flame sheet itself. Third, they assume that the velocity profile in the boundary layer is unaffected or only slightly affected by the presence of wall blowing and combustion, so that standard friction coefficient for a turbulent boundary layer remains valid. By employing these assumptions, they obtain an equation for the regression rate given by

$$\rho_f r = C\, G\, Re_x^{-0.2} (C_H / C_{Ho}) (u_e / u_c) (h_f - h_w) / \Delta H \tag{I.2.8}$$

where C is a function of the mainstream Mach number (about 0.03 for the low Mach numbers encountered in hybrids), G the total mass flux, C_H the Stanton number, C_{Ho} the Stanton number in the absence of blowing, u_e the velocity at the edge of the boundary layer, u_c the velocity at the flame, h_f the stagnation enthalpy at the flame temperature, h_w the enthalpy at the wall in the gas phase, and ΔH the total heat of gasification as in Eq. (I.2.7). The ratio of Stanton numbers, C_H/C_{Ho}, represents the fraction of heat transferred to the surface by convection when compared to the case with no blowing. This ratio may be lower than 0.2 [I.8]. The velocity ratio, u_e/u_c, is determined by the flame position in the boundary layer. If radiative heat transfer is also important, as may be the case with metalized fuels [I.13], an additional term may be added to the right side of Eq. (I.2.8):

$$r_{rad} = \sigma\varepsilon_w(\varepsilon_g T_f^4 - \alpha_g T_w^4)/(\rho_f \Delta H) \tag{I.2.9}$$

where σ represents the Stefan–Boltzmann constant, ε_w the emissivity of the wall, ε_g the emissivity of the gas at the flame temperature T_f, and α_g the absorptivity of the gas at the wall temperature T_w.

In Ref. [I.13] Marxman et al. present methods to obtain some of the factors comprising the right side of Eq. (I.2.8), which are not known *a priori* for a given hybrid system. Using the integral technique of boundary layer theory, the authors show that the velocity ratio may be obtained from

$$u_c/u_e = [O/F(h_f - h_w)/\Delta H]/[K_{OXe} + (O/F + K_{OXe})(h_f - h_w)/\Delta H] \tag{I.2.10}$$

where O/F symbolizes the oxidizer to fuel mass ratio and K_{OXe} is the mass fraction of oxidizer in the freestream core flow, which, for a hybrid motor using GOX as the oxidizer, would equal unity. Marxman et al assume that O/F ratio and the $(h_f - h_w)/\Delta H$ factor are independent of position and constant for a given oxidizer/fuel combination. The Stanton number ratio was found to be

$$C_H/C_{Ho} = 1.2B^{-0.77} \tag{I.2.11}$$

for $5 \le B \le 100$, where

$$B = (\rho v)_w/[\rho_e u_e(c_f/2)] = (u_e/u_c)(h_f - h_w)\Delta H \tag{I.2.12}$$

is the mass transfer number. When the Prandtl number is equal to 1 and the radiation term in Eq. (I.2.9) is negligible, the B parameter can be approximated by the last expression given in Eq. (2.12). The mass transfer number B is a very important parameter in hybrid combustion. It represents both the similarity parameter for a boundary layer with injection and a thermodynamic parameter of the system.

When B=constant and Le=1, the velocity, species concentration, and enthalpy profiles are similar everywhere in the turbulent boundary layer [I.13].

Marxman, Wooldridge, and Muzzy reduced their regression rate equation (Eq. I.2.8) to a simplified form by combining Eq. (I.2.8), (I.2.11), and (I.2.12), thus obtaining

$$\rho_f r = 0.036\, G\, (Re_x)^{-0.2} \alpha\, B^{0.23} G^{0.8} x^{-0.2} \qquad \text{(I.2.13)}$$

for hybrid combustion with no radiative heat transfer. Again, specifying the oxidizer/fuel combination essentially fixes B. The authors explain that, since B is raised to a small power, even large changes in $(h_f - h_w)$ or ΔH produce only minor changes in the regression rate. The physical reasoning behind this observation is that, in the Marxman et al analysis, the regression rate of the solid fuel is coupled tightly to the aerodynamics of the reacting boundary–layer flow. Increasing $(h_f - h_w)$, for example, would tend to increase the regression rate. In turn, however, the increase in fuel mass addition creates stronger blockage of the convective heat transfer to the surface, which tends to decrease the regression rate. In this case, the fuel regression rate depends primarily upon G, the total mass flux. Since G at some location x depends on both the oxidizer flow entering the combustion port as well as all fuel injected upstream of location x, the local regression rate depends on the regression rate at all upstream locations. In addition, G decreases as the port area increases during burning. Therefore, one expects the regression to increase with axial position along the fuel grain, while decreasing with time.

For systems wherein radiative heat transfer to the fuel surface may be important, such as in the case of a solid fuel grain with a high metal loading, one must find a blowing parameter due to radiative heat transfer, B_{rad}. For this parameter, Marxman et al. obtained

$$B_{rad}/B = 1 + (Q_{rad}/Q_c)(B_{rad}/B)^{0.77} \qquad \text{(I.2.14)}$$

where

$$Q_c = 0.036\, G\, \Delta H\, (Gx/\mu)^{-0.2} B^{0.23} \qquad \text{(I.2.15)}$$

and

$$Q_{rad} = \sigma \varepsilon_w (\varepsilon_g T_f^4 - \alpha_g T_w^4) \qquad \text{(I.2.16)}$$

while B remains as defined previously. Estimating B_{rad}/B as $\exp(1.3Q_{rad}/Q_c)$ (which is approximately true over a wide range of Q_{rad}/Q_c), the authors obtained a modified version of Eq. (2.8):

$$\rho_f r = [Q_c \exp(-Q_{rad}/Q_c) + Q_{rad}]/\Delta H \tag{I.2.17}$$

which accounts for the increase in regression rate due to radiative heat transfer. This equation reduces to Eq. (I.2.8) if $Q_{rad}=0$. Note from Eq. (I.2.17) that an increase in radiative heat transfer results in a decrease in convective heat transfer due to the corresponding increase in mass blockage. If $Q_{rad}=Q_c$, then $\rho_f r$ increases by about 35% over that for $Q_{rad}=0$. More importantly, though, about 75% of the total heat transfer to the surface comes from radiation, so the system behaves in a manner much different than that of a non–radiating case.

In his 1972 paper [I.12], Muzzy provided an excellent summary of some of the major implications of the theoretical heat–transfer limited model developed by Marxman, Gilbert, Wooldridge, and Muzzy during the mid 1960's. In the first part of the paper he emphasized the following significant concepts:

(1) The regression rate depends only weakly on the enthalpy difference between the flame and the fuel surface because of the mass blockage effect, so many different types of solid fuels have similar regression rates. For the same reason, the burning rates of hybrid fuel grains are not sensitive to ambient temperature.

(2) The regression rate depends strongly on port geometry. A change in regression rate at an upstream position can propagate along the entire length of the fuel grain since local regression rate depends upon the regression rate at all upstream positions. This implies that optimal hybrid motor design requires complete understanding of internal ballistic behavior.

(3) Only a strong radiation source will significantly increase the regression rate. Weak radiative transfer to the surface, on the order of half the convective heat transfer, results in a small (about 10%) net increase in regression rate [I.12].

I.2.1.5: Other Analyzes Including Gas–Phase Thermal Radiation

Several researchers have considered the influence on regression rate of thermal radiation from the gas–phase to the solid fuel surface. It should be stated at the outset that a fair amount of confusion and disagreement exist in the literature regarding the importance of thermal radiation in determining the regression rate. Marxman et al's treatment of this subject was given above and suggests that weak radiation has little or no influence on regression rate. This situation is expected in non–metalized solid fuels. Their experiments also indicated that the radiative transfer to the solid fuel surface amounted to about 5 to 10% of the convective heat transfer.

Estey, Altman, and McFarlane also considered radiative heat transfer in a more recent publication [I.20]. They employ a radiative flux term of the form

$$Q_r = \sigma T_g^4 \left(1 - e^{-\kappa P D}\right) \tag{I.2.18}$$

which is similar to that suggested by Muzzy [I.12]. The parameter κ represents the gas–phase absorption coefficient. The term in parentheses in Eq. (I.2.18) is the emissivity of the gas phase, which increases as the product of pressure and diameter (or hydraulic diameter) increases due to the nature of the inverse exponential function. Marxman et al. states that for a plexiglas/oxygen system, the gas–phase emissivity is about 0.02 [I.13]. Altman concludes that the addition of a radiative transfer term for metal–loaded fuels improves empirical correlations, while for pure hydrocarbon fuels classical convective heat transfer theory works best.

Strand et al [I.7] provides a treatment of radiative heat transfer in a recent study. He considered radiation from both the gas and a soot particle cloud that forms shortly after ignition. For the gas–phase contribution, Strand uses Eq. (I.2.18), but also includes an empirical expression for κ as a function of pressure

$$\kappa = 9.33\times10^{-4} - 6.19\times10^{-6}\, P + 1.79\times10^{-8}\, P^2 \tag{I.2.19}$$

which was obtained from radiation measurements of a high–energy non–metalized solid propellant, where P was measured in psig.

The thermal radiation emanating from the particle cloud was represented by

$$Q_{r,\text{cloud}} = \sigma T_g^4 \left(1 - e^{-a_p N_p}\right) \tag{I.2.20}$$

where N_p represents the particle number density and a_p a multiplier constant. The term a_pN_p depends on the weight fraction of the radiating particles, and appears to be difficult to evaluate, considering the analysis given in [I.7]. In contrast to the previous researchers mentioned, Strand concludes that particle radiation from powdery soot is a significant source of energy driving solid fuel regression. Also, he states that variations in gas radiation with pressure and O/F ratio should be accounted for in future works. Experimentally, it was found that radiative heat flux accounted for about 30% of the total heat flux, which represents a much larger fraction than found by other researchers. However, it should be noted that Strand's motor, like most lab–scale burners, operated at the lower pressure (up to 315 psi) and lower oxidizer mass flux (up to 0.15 lb_m/in^2–s) ranges of interest.

In contrast to Strand's findings, Salita [I.21] states that neither gas–phase radiation nor radiation from soot particles should be important in hybrid combustion of both metalized and pure hydrocarbon fuels. According to Salita, soot particles do not appear in hybrids because of the highly–oxidative core flow. In addition, the boundary layer along most of the fuel grain is said to be thin so that the radiation from the flame zone is optically thin and has very low emissivity. In practice, solid fuels made by high molecular weight polymers should produce large amounts of soot particles, which could shield the fuel surface from radiative heating generated in the diffusion flame zone.

I.2.2: Pressure–Dependent Regression Rate Analyzes

I.2.2.1: Smoot and Price

Besides Marxman and his associates, several other groups were actively pursuing hybrid combustion research during the 1960's. Smoot and Price [I.9–I.11] performed over 150 experiments with a laboratory–scale slab burner at what was then the Lockheed Propulsion Company in Redlands, California. They [I.9] developed a theory of hybrid regression rate by extending the work of Barrere and Moutet [I.22] to include the effects of condensed species at the wall. Like previous researchers, Smoot and Price also found that the regression rate should *theoretically* depend on $G^{0.8}$.

Smoot and Price performed experiments using solid fuels of butyl rubber, Polybutadiene–acrylic acid (PBAA) copolymer, and polyurethane (PU). They varied the oxidizer composition from 100% fluorine to 100% oxygen. Not surprisingly, Smoot and Price found that average regression rates were higher when a larger ratio of fluorine to oxygen was used for the oxidizer. They also discovered that at low total mass fluxes ($<0.07\ \mathrm{lb_m/in^2}$–s) the average regression rates of the butyl rubber solid fuel slabs followed the $G^{0.8}$ law. However, at higher total mass fluxes, the regression rate became essentially independent of mass flux, but strongly dependent on total operating pressure. This trend was observed for butyl rubber burning with 100% fluorine. At the relatively low operating pressures involved (<150 psia), the regression rates always fell below that predicted by the $G^{0.8}$ theory. Increases in pressure push the regression rate toward the line predicted by the heat transfer theory. At 1000 psi, the 0.8 line was reached. Note that for practical hybrid rocket motors, the operating pressure would most likely be at least 500 psi, far above those Smoot and Price used in their experiments discussed in ref [I.9]. Smoot and Price found similar results with the other solid fuels and oxidizers mentioned previously.

Smoot and Price defined three different regions of regression rate dependence. In low–mass flux region I, the regression rate was controlled entirely by heat transfer and depends on $G^{0.8}$. For medium–mass fluxes in region II, the regression rate depended on both flow rate and pressure, with increasing pressure causing increasing regression rate at constant mass flux. In this region,

$$r = (aG^{0.8}\, bp^n)/(aG^{0.8} + bp^n) \tag{I.2.21}$$

where p represents the motor pressure and a, b, and n are empirical constants. In region III, the regression rate depends solely on operating pressure, such that $r=ap^n$, like a solid propellant grain. This region corresponds to high mass fluxes [I.9].

Smoot and Price also studied the regression rate behavior of solid fuel grains loaded with metal particles. In Ref [I.10] they present the results of an experimental investigation conducted using a LiH (lithium hydride)/butyl rubber/oxygen/fluorine system. They varied the solid fuel composition from 100% butyl rubber to 90% LiH and the oxidizer composition from 100% fluorine to 100% oxygen. Smoot and Price found that in the low total mass flux regime ($G<0.04\ \mathrm{lb_m/in^2}$–s), the average regression rate increased significantly only if the amount of LiH in the grain was greater than about 50% [I.10]. This is the same region where they found 100% butyl rubber grains to regress according to the $G^{0.8}$ law, as discussed previously. At higher mass flux levels, where the operating pressure influenced the regression rate, the solid fuel regression rate displayed much more sensitivity to the LiH mass fraction. Smoot and Price postulated that the observed change in regression rate LiH mass fraction sensitivity resulted from the transition from one controlling mechanism to the other. They also found that increasing the percentage of LiH reduced the pressure dependence.

Smoot and Price suspected that either gas–phase oxidizer–fuel reactions or heterogeneous reactions between oxidizer and fuel at the fuel surface were responsible for the dependence of regression rate on pressure that they observed [I.11]. After performing a series of experiments wherein they varied the fluorine partial pressure independently of the total pressure by using oxygen and nitrogen as diluents, Smoot and Price found that the solid fuel regression rates depended significantly on the partial pressure of fluorine, but not on the total pressure. They eventually concluded that oxidizer diffusion to the fuel surface and subsequent first–order heterogeneous reactions were responsible for the pressure dependence, and derived the following equation:

$$P_{o\infty}/\rho_f r = \{33P_{\infty}(x/\mu)^{0.2}Sc^{2/3}\,[\exp(B_1\lambda)-1]/G^{0.8}B_1\lambda\} + 1/k \qquad (I.2.22)$$

where $P_{o\infty}$ is the partial oxidizer pressure in the freestream (psia), P_{∞} the total freestream pressure, S_c the Scmidt number, B_1 the blowing parameter, λ the weight fraction of gaseous products from fuel decomposition, and k a kinetic rate constant. The symbols x and μ have their usual meanings. It should be noted that Smoot and Price's experimental work, though exhaustive, lied outside the range of practical hybrid rocket applications, where both flow rates and pressures would probably be an order of magnitude greater than those of their lab–scale slab burner.

I2.2.2: Marxman and Wooldridge's Analysis

Marxman and Wooldridge also studied the effect of pressure on regression rate [I.12]. They showed that heterogeneous reactions at the solid fuel surface could not by themselves account for the pressure sensitivity observed by Smoot and Price. Marxman and Wooldridge attributed regression rate pressure dependence to finite–rate gas–phase and heterogeneous reactions occurring in the turbulent boundary layer. In order to account for the pressure dependence, they derived the following equation:

$$r/r_{\infty} = (2t_m/t_r)^{0.5}\,[1 - t_m/t_r\,(1 - e^{-tr/tm})]^{0.5} \qquad (I.2.23)$$

where r_∞ is the reference state regression rate given by the heat–transfer limited analysis, Eq. (I.2.13) or Eq. (I.2.17), t_r represents a characteristic reaction time, and t_m a characteristic mixing time. The value of t_m/t_r can be approximated by

$$t_r/t_m = C_1 G^{0.8} x^{-0.2}/P \qquad \text{(I.2.24)}$$

where C_1 is an empirical constant that depends on the particular fuel–oxidizer system.

I.2.2.3: Muzzy's Analysis

In his review article [I.12], Muzzy states that for non–radiative systems with large values of t_r/t_m (i.e., low pressures and/or high G values), Eqs. (I.2.13), (I.2.23), and (I.2.24) can be combined to give:

$$r = C_2 P^{0.5} G^{0.4} x^{-0.1} \qquad \text{(I.2.25)}$$

in the region of operating conditions where chemical kinetics are an important factor in determining regression rate (i.e., low pressure and/or high G values). Notice from Eq. (I.2.26) that when kinetics become important, the regression rate has a weaker dependence on total mass flux than that predicted by the heat–transfer limited model, where r depends on $G^{0.8}$.

Figure I.2.1 summarizes some of the results discussed in the above sections. At medium mass fluxes, the regression behavior is dominated by convective heat transfer, and theoretically follows Eq. (I.2.8) or (I.2.13). In this regime, neither radiation nor kinetics influence the regression rate. At very high mass fluxes and low pressures conditions, the dependency of the gas–phase reaction rates on pressure can have a significant effect on regression rate. When the motor pressure is lower than a threshold value, the regression rate will be lower than that predicted by convective heat–transfer analysis. As pressure increases, the reaction rate increases, and the regression rate approaches the convectively predicted value.

Pressure has the opposite effect on the other end of the mass flux spectrum. At low mass fluxes, the effect of gas–phase radiation becomes important. Because of the complicated interaction between mass blowing *from* the fuel surface and convective and radiative heat transfer *to* the fuel surface, only a very strong radiation source will significantly influence the regression rate at anything higher than low mass fluxes. In the low mass flux regime, the effect of radiation becomes important. As the product of pressure and motor inner diameter (pD) increases, the effect of radiation becomes more prominent at a given mass flux. The pD term gives a measure of the gas optical density as described in [I.23,I.24]. When pD is high, the gas emits thermal radiation more efficiently, and therefore the regression rate increases to higher values than predicted by simple convective theory.

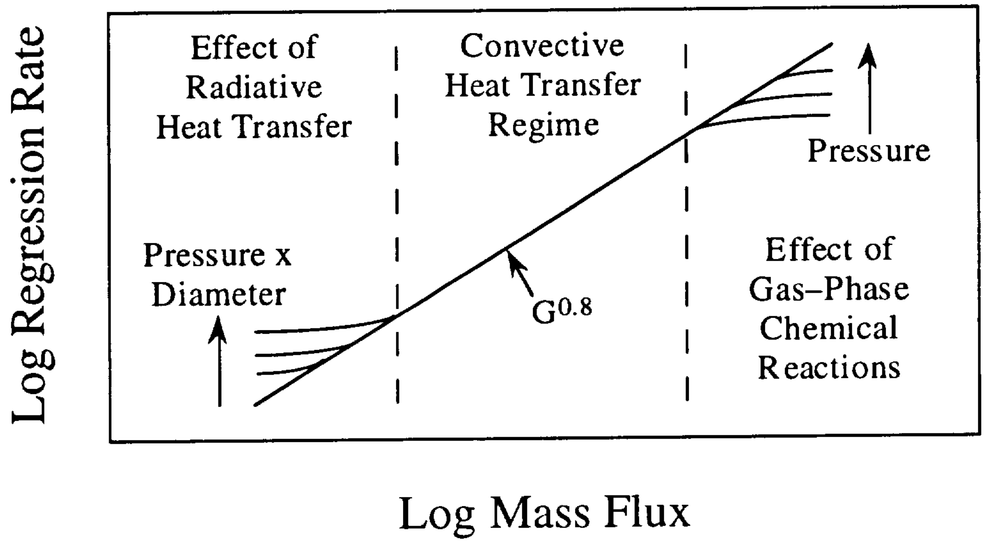

Figure I.2.1 Regimes of regression rate dependence

I.2.3: Regression Rate Analyzes based on Polymer Decomposition

I.2.3.1: Ramaholli's Analysis

Ramaholli [I.25] developed a pressure–sensitive analysis, called FSV (*f*ragment *s*ize *v*aporizing), to explain the solid fuel regression rate. He believed that the regression rate was governed by solid–fuel surface degradation, and that the fuel depolymerized into small fragments. He also believed that unburned oxidizer may diffuse across the flame sheet and participate in heterogeneous reactions on the solid fuel surface.

Ramaholli's specific equations for regression rate are somewhat complicated and not particularly important for the present discussion. However, it should be noted that his theory predicts exactly the opposite trends predicted by heat–transfer limited analysis like that of Marxman's discussed in previous sections. Ramaholli also states in Ref [I.25] that Marxman's model works well for "low" mass fluxes, but does not work for "high" mass fluxes, based upon the results of Smoot and Price's experiments. He never defines exactly what is meant by "low" and "high" values of the mass flux, but as already stated, the operating conditions of the Smoot and Price hybrid motor were well below what can be expected in booster–size hybrid motors, and therefore it would appear that Ramaholli's observations are in error. Furthermore, Ramaholli's own motor had a maximum operating pressure of 70 psi [I.25], which is not very realistic. In a later paper [I.26], Ramaholli et al. present a very limited amount of data which indicated that the regression rate increased with oxidizer mass flux and decreased with port diameter, but exhibits no obvious trends with respect to pressure. Again, the motor oxidizer mass flux and pressure had low maximum values of 0.1 lb_m/in^2–s and 156 psi, respectively.

I.2.3.2: Brill and Arisawa's Analysis

Following the initial study by Chen and Brill [I.27], Brill and Arisawa [I.15,I.16], at the University of Delaware, performed a series of experiments to determine the decomposition products of Hydroxyl–Terminated Polybutadiene (HTPB). Flash pyrolysis of uncurred R–45M, the pre–polymer of HTPB, was performed under various heating rates, temperatures, and pressures in an Argon environment. According to Brill, using R–45M rather than cured HTPB is justified because during rapid thermal decomposition, such as occurs in a hybrid rocket motor, the urethane bonds between the cross linking agent (such as Isonate 143L) and the pre–polymer cleave first. The HTPB acts like an uncurred polymer when it decomposes. T–Jump/FTIR spectroscopy was used to determine the gaseous pyrolysis products [I.15,I.16].

Thirteen gaseous products, representing about 70% of the mass of the original sample, were identified in the study. Of these thirteen products, 95 to 98% of the measured masses were attributed to six major products: butadiene (BD), ethylene (ET), trans–butadiene oligomer (t–BDO), 4–vinyl 1–cyclohexene (4–VCH), 1,5–hexadiene (1,5–HD), and cyclopentane (CP).

Brill and Arisawa reach several important conclusions in their study. First, at pressures at or below 2 atm and temperatures below about 515 to 560 °C, the pyrolysis of polybutadiene compounds was dominated by bulk–phase reactions in the polymer, such as bond breaking and polymer chain reorganization. However, for low pressures ($p<2$ atm) and high temperatures ($560 < T < 609$°C), or for higher pressures ($p=11$ atm) and all temperatures tested ($T>465$ °C), the rate of gaseous product evolution was controlled by formation and *desorption* of higher molecular weight fragments from the fuel surface. The authors state that the temperature where the transition between controlling mechanisms (from bulk phase kinetics to desorption kinetics) occurs corresponds to the temperature where the bulk–phase pyrolysis reactions probably reach their maximum rate. This temperature is determined by the pressure, with higher pressures corresponding to lower transition temperatures. Therefore, for modeling the combustion processes of rockets containing HTPB, the kinetics of desorption from the surface should be used instead of the bulk–phase chemical decomposition kinetics [I.16].

Note that Brill and Arisawa's results do no conflict with the above convective, radiative, and kinetic theories because polymer decomposition may not be the rate–limiting step in the overall combustion process in a hybrid rocket motor. Brill and Arisawa's work describes the pyrolysis behavior of the HTPB, not the overall combustion process which includes other physical processes such as those described by Marxman et al, Smoot and Price, Strand, and others.

I.3 Experimental Method of Approach

This Section discusses the method of approach used to obtain the desired results, which are presented in the Section I.4. First, the hybrid test rig and its operation is described. In later sections, the diagnostic equipment used to measure the parameters of interest is explained. A discussion of the solid fuel processing techniques are given at the end of the chapter.

I.3.1: Hybrid Test Rig Design and Setup

A schematic diagram of the overall hybrid test rig is shown in Figure I.3.1. The test rig includes a 2–D slab motor, a gaseous oxygen supply system, an ignition system, and a computer control system (not shown for clarity). Each subsystem is discussed below individually.

I.3.1.1: Hybrid Motor Analog Design Analysis

In order to assist the design of the test motor, a computer code was developed that utilized a zero–dimensional, time–dependent continuity equation coupled with data from the NASA Chemical Equilibrium and Transport (CET–86) code to determine fuel regression rate, oxidizer–to–fuel mass ratio, chamber pressure, and gas temperature as a function of time for a given design geometry. The equation

$$dM/dt = m_{ox} + m_{fuel} - m_{out} \tag{I.3.1}$$

represents conservation of mass for the hybrid motor. The first term on the right side of the equation, m_{ox}, the oxidizer mass flow rate was treated as a parameter to be varied. The second term can be represented by

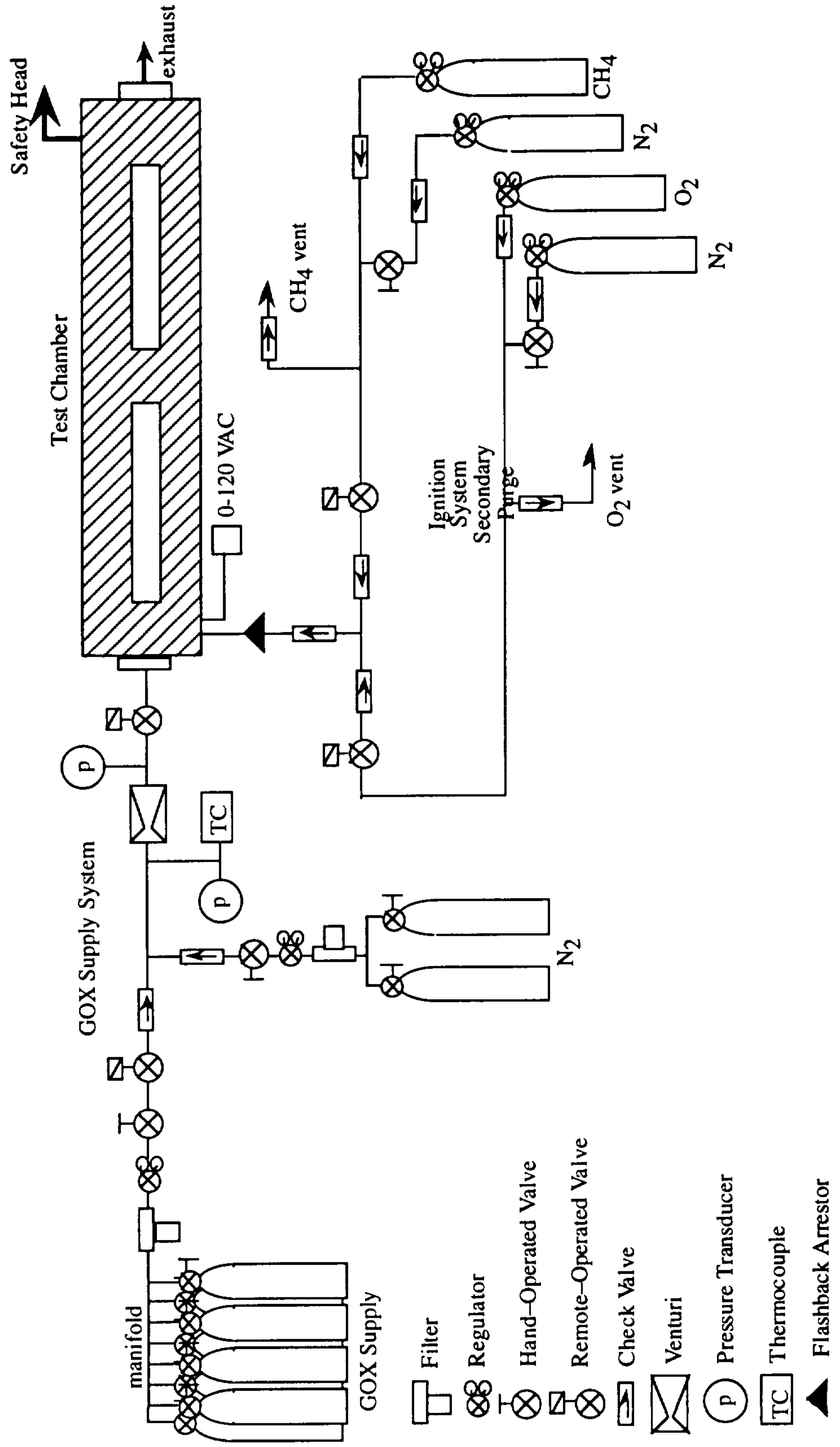

Figure I.3.1 Schematic Diagram of Hybrid Test Rig

Figure I.3.1 Schematic diagram of hybrid test rig

$$m_{fuel} = \rho_f A_b r \qquad (I.3.2)$$

where ρ_f is the solid fuel mass density, A_b is the total burning area for both slabs, and r is the solid fuel regression rate. Note that, in general, r is a function of time. From [I.1], the global regression rate, r, can be represented as

$$r = aG_o^b \qquad (I.3.3)$$

where G_o is the oxidizer mass flux, essentially m_{ox}/A_{port}, and a and b are constants that depend on the particular fuel/oxidizer combination. For the GOX/HTPB propellant, a=0.104 b=0.681 when G_o has units of lb_m/in^2–s. For a two slab motor, the time rate of change in distance between the two slabs, dh/dt, is equal to twice the regression rate, 2r. Also, the port area, A_{port}, is equal to w·h(t), where w is the width of the fuel slabs. Substituting into Eq. (I.3.3), one obtains

$$dh/dt = 2a(m_o/w \cdot h(t))^b \qquad (I.3.4)$$

This equation can be easily integrated using separation of variables to obtain an expression for r as an explicit function of time. Thus, knowing the oxidizer mass flow rate allows one to obtain the global regression rate and the corresponding fuel mass flow rate. The instantaneous oxidizer–to–fuel mass ratio, O/F, is simply m_{ox}/m_{fuel}.

The quasi–steady motor pressure can be obtained by setting the storage term to zero in Eq (I.3.1) and using the choked flow mass flow rate in place of m_{out}:

$$m_{out} = \Gamma(\gamma)\, p_c\, A^*/(RT)^{1/2} \qquad (I.3.5)$$

where γ is the ratio of specific heats, p_c the chamber pressure, A^* the exit nozzle throat area, R the specific gas constant, and T the gas bulk temperature. The CET–86 chemical equilibrium code was used to obtain individual polynomial equations of g, R, and T as a function of O/F ratio for a gaseous oxygen/HTPB fuel system. In this manner, the quasi–steady chamber pressure was found as a function of m_{ox} for a particular throat area using Eqs (I.3.1) through (I.3.5).

In order to meet a range of possible test conditions, parametric studies were conducted with the code to determine the effect of oxidizer flow rate, nozzle diameter, and test time on global motor operating characteristics such as chamber pressure, O/F ratio, solid fuel regression rate, and burned fuel web thickness. Based partially upon the results of the study, a windowed 2–D hybrid motor was designed. Figure I.3.2 shows an exploded view of the motor, including main body, window assemblies, GOX injector, nozzle assembly, graphite inserts, and fuel slabs. The main body of the motor was constructed of stainless steel and weighed approximately 315.5 kg (700 lbs). With a safety factor of 2.5, the test rig was designed to operate at a maximum pressure of 1000 psi. In addition to the safety factor consideration, a 1450 psi burst diaphragm was installed to prevent any damage to the motor in the case of an over–pressurization. The operating chamber pressure of the motor was partially controlled using interchangeable graphite exit nozzles. The motor has an overall length of 1,067 mm, width of 178 mm, and height of 254 mm.

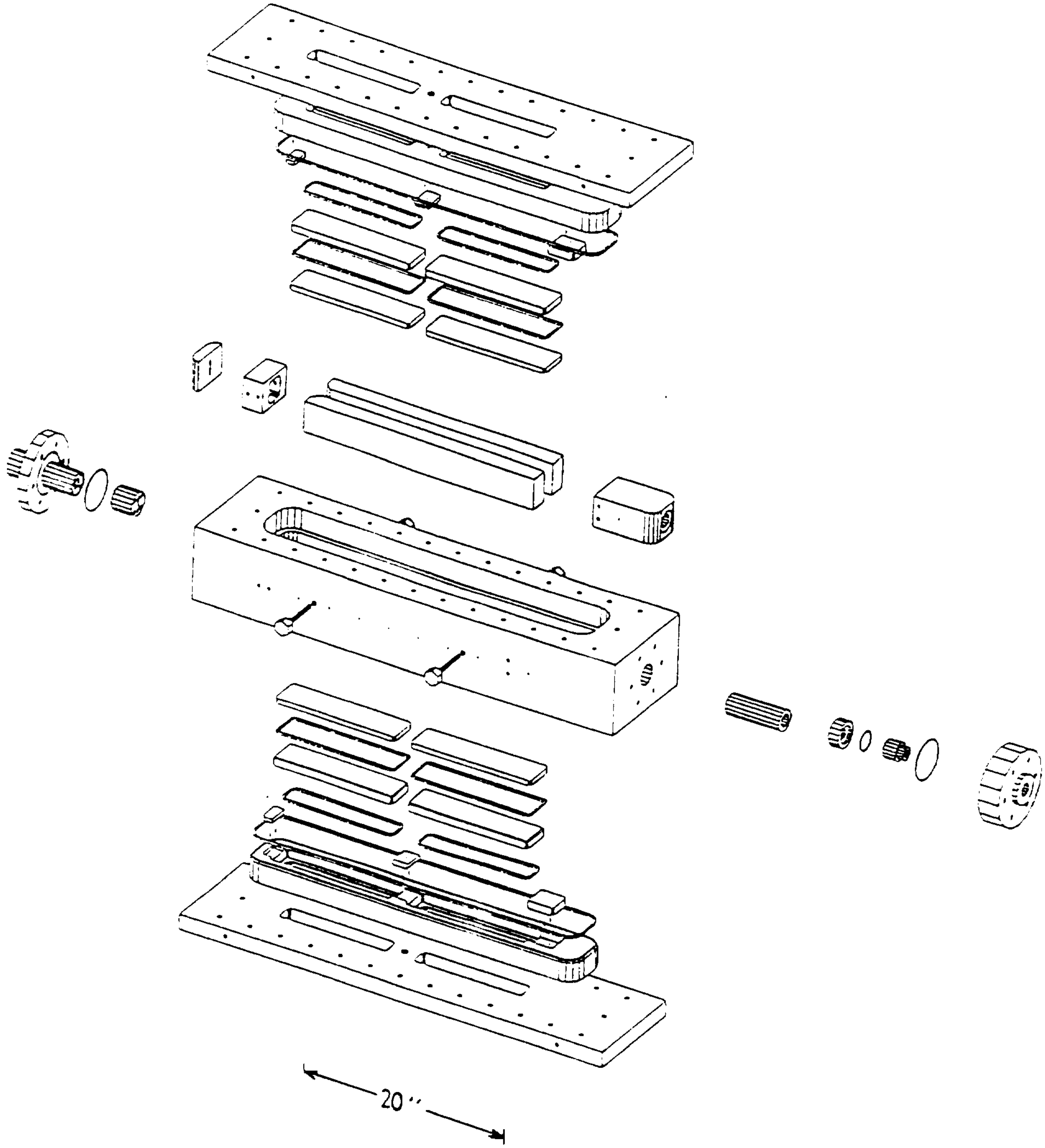

Figure I.3.2 Exploded view of motor

The motor can be operated with either two opposing fuel slabs or one fuel slab with an opposing inert slab. All tests discussed here utilized two opposing fuel slabs. The fuel slabs are 584 mm (23 in) long and 76 mm (3 in) wide. They typically had a thickness of between 1.68 and 1.75 inches. Figure I.3.3 illustrates the geometry of the fuel slabs and sample holders, which are used to hold the fuel slabs in place during a test run. The sample holders have a length of 20 in, width of 2.25 in, and thickness of 1 in. All sample holders were manufactured with 7 thermocouple ports along the longitudinal centerline.

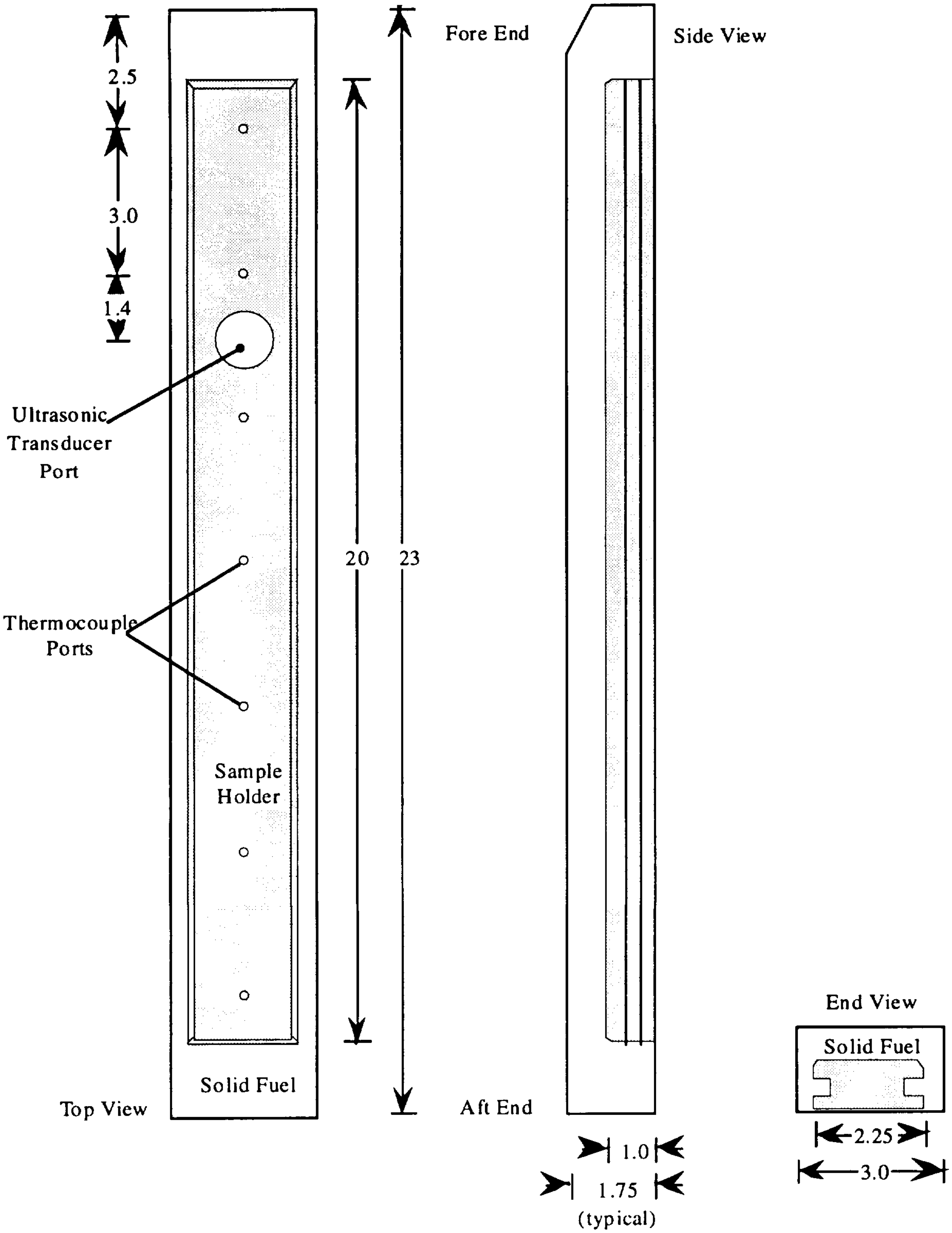

Figure I.3.3 Fuel slab sample holder geometry
(All dimensions given in inches)

The first thermocouple port occurs 1 inch from the front edge of the sample holder and a 3 inch intervals thereafter. In addition to the thermocouple ports, two sample holders were also manufactured with a port for the ultrasonic transducer. One sample holder had the ultrasonic transducer port located 5.4 inches downstream from the front edge of the sample holder (shown in Figure I.3.3) while the port was located 8.4 in downstream in the second sample holder. Since the sample holders could also be reversed in the fuel mold, the ultrasonic transducer could be selected from one of four locations: 6.9, 9.9, 13.1, and 16.1 inches downstream from the fore end of the fuel slab.

I.3.1.2: Gaseous Oxygen Supply System

Gaseous oxygen (GOX) was used as the oxidizer for all test firings. The gaseous oxygen supply system (shown in Fig I.3.1) consisted of a main feed line and a nitrogen purge line. Remotely operated ball valves were used to initiate and terminate the flow of oxygen, while a critical flow venturi was used to maintain a steady mass flow of GOX through the main line. The venturi had an adjustable throat area so that the GOX mass flow rate could be easily selected.

For a given test, the desired flow rate was preset by adjusting the throat area of the venturi and the regulator setting of GOX supply line. The exact GOX flow rate was determined after the test by using the measured data from an upstream thermocouple and two pressure transducers located on either side of the venturi. The data from calibration of the venturi provided curvefits relating the GOX mass flow rate to the upstream flowing pressure for a given venturi throat setting. Thus, measuring the pressure just upstream of the venturi during a test allowed the GOX mass flow rate to be easily deduced.

Filters and check valves in the GOX and nitrogen supply lines were employed to prevent any back flow and contamination of the system. The GOX supply system can deliver a maximum oxygen mass flow of about 0.8 lb_m/s.

I.3.1.3: Ignition System

The ignition system consisted of a pair of high–pressure gaseous oxygen/methane pre–mixed torches and a pair of solid–propellant sticks to produce pilot flames in the upstream region of the solid fuel slabs. Flashback arrestors were used to prevent the occurrence of flame flashback in the pre–mixed sections of the igniter lines. The solid–propellant sticks were ignited electrically using nichrome wires connected to an AC transformer. Remotely operated solenoid valves were used to control the flow of oxygen and methane. Check valves and vents were installed in order to prevent the contamination of the gas bottles and any over pressurization of the system. Gaseous nitrogen was used to purge the ignition system after each test. In order to ignite the fuel slabs for a test, the torches were first activated by opening the remotely operated solenoid valves. Then the solid propellant sticks were ignited by switching on a power supply attached to the nichrome wires. The pilot flames ignited the torches, which in turn ignited the solid fuel slabs. The power to the nichrome wires and the ignition system solenoid valves were switched off just after ignition. After the initial system check–out tests, it was determined that successful ignition could be achieved using only the pilot flames generated by the solid–propellant sticks without activating the CH_4/O_2 torches. Thereafter, the ignition gas–supply lines were used primarily as an auxiliary nitrogen purge system, which was activated at the end of each test.

I.3.2: Instrumentation

The hybrid motor analog was instrumented with a variety of diagnostic equipment to measure the parameters of interest. Figure I.3.4 shows a schematic of the motor with the locations of some of the diagnostic equipment, indicating pressure transducers (P), thermocouples (TC), ultrasonic transducer (UST), and windows for use with the real–time X–ray radiography system. Though a maximum of seven thermocouple ports are available for solid–phase temperature measurement, Fig I.3.4 illustrates only four locations for clarity. Table I.3.1 below lists the instruments used to measure the parameters of interest.

Table I.3.1 Diagnostics of the Hybrid Motor Analog

INSTRUMENT	MEASURED QUANTITY
Setra Pressure Transducer	Quasi–steady pressure
Kistler Pressure Transducer	Dynamic pressure
25 μm Thermocouple	Surface temperature, Subsurface thermal wave
Mass Balance	Total fuel mass consumed
Caliper	Averaged burned web thickness
Ultrasonic Transducer	Propagation time through fuel web thickness
X–Ray Radiography System	Instantaneous burned web thickness
Video Camera	Plume jet and integrity of test motor during firing
Pressure differential across venturi and upstream GOX temperature	GOX flow rate as a function of time

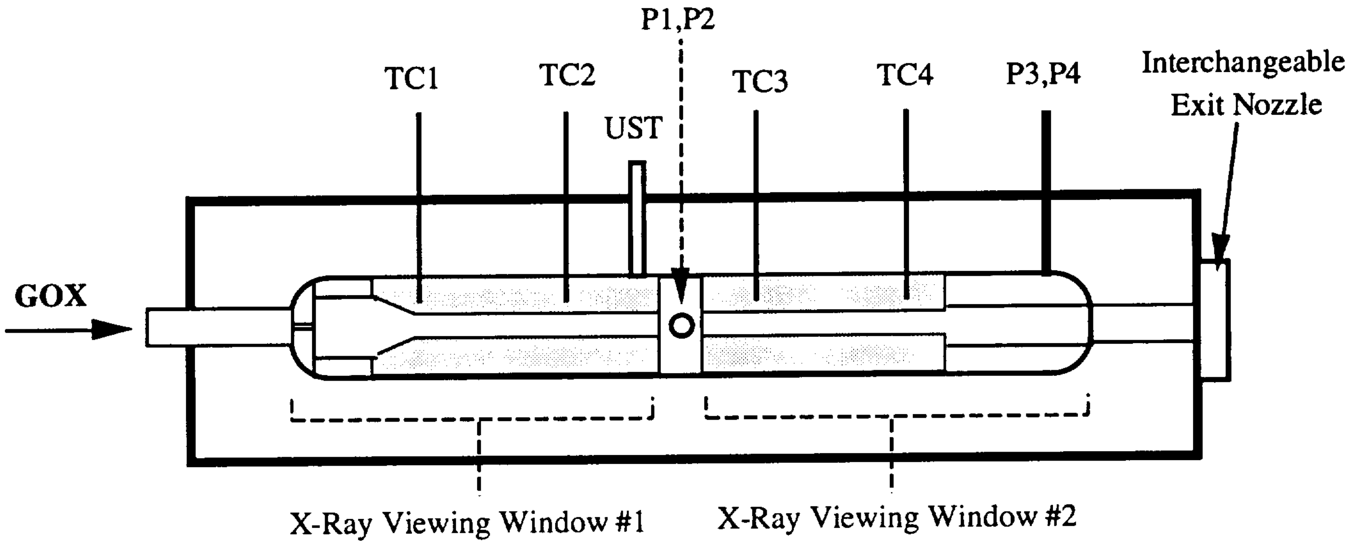

Figure I.3.4 Instrumentation of the Hybrid Motor

I.3.2.1: Motor and GOX Line Pressure Measurements

High–frequency, piezoelectric, Kistler pressure transducers (model 601B1) were used to measure the dynamic motor pressure. The transducer model 601B1 has a rise time of approximately 1 µs, making them suitable for measuring high frequency pressure oscillations, and a maximum pressure rating of 15,000 psi, much higher than the hybrid motor design pressure of 1000 psi. In general, three Kistler pressure transducers were used for each test: one on either side near the midpoint of the motor and one on top of the motor near the back. Though the Kistler pressure transducers require frequent re–calibration and are prone to signal drift, they have very rapid response time for high–frequency applications.

Diaphragm–type, Setra pressure transducers (model 205) were also employed to measure the motor pressure. This type of transducer has a response time on the order of 1 ms and a maximum working pressure of 3000 psi. Usually, a single Setra transducer was placed near the Kistler transducer on the top, rear portion of the motor. The Setra transducer served basically as a back–up pressure measurement device in the unlikely event that the sensitive Kistler transducers provided unreliable signals during the test. Though the Setra model 205 is easier to use than the Kistlers and rarely requires re–calibration, it is not as sensitive to pressure oscillations.

In addition to the Setra 205 transducer used for motor pressure measurement, several Setra pressure transducers were also used for GOX supply line and ignition line pressure measurement. Two model 206 Setra pressure transducers were located on the GOX supply line: one just upstream of the adjustable area, critical flow venture, and one just downstream of this venturi. Knowing the upstream and downstream venturi pressure allows one to determine the exact GOX mass flow rate during the test and also to verify that the venturi remains choked so that the GOX mass flow rate is indeed constant.

I.3.2.2: Solid Fuel Temperature Measurements

Fine–wire thermocouples give accurate measurements of the subsurface thermal wave thickness and burning surface temperature of solid fuels and solid propellants. In order to measure these quantities for the hybrid motor analog, an array of 25 μm, Pt/Pt–10%Rh (S–type) were embedded in the top solid fuel slab during the fuel casting procedure. Thermocouples were manufactured at the High Pressure Combustion Lab using 25 μm wire from Omega.

Figure I.3.5 illustrates a single thermocouple assembly embedded in a fuel slab. The thermocouple assembly consists of two lengths of thermocouple extension wire (one positive lead and one negative lead) threaded through a short length of ceramic insulation tube (about 1.5 in long). A one–inch length of steel tubing was placed over the ceramic insulation to provide mechanical strength. A thermocouple was soldered to the exposed ends of the extension wires. The entire assembly was glued in place in a thermocouple port in the fuel slab holder.

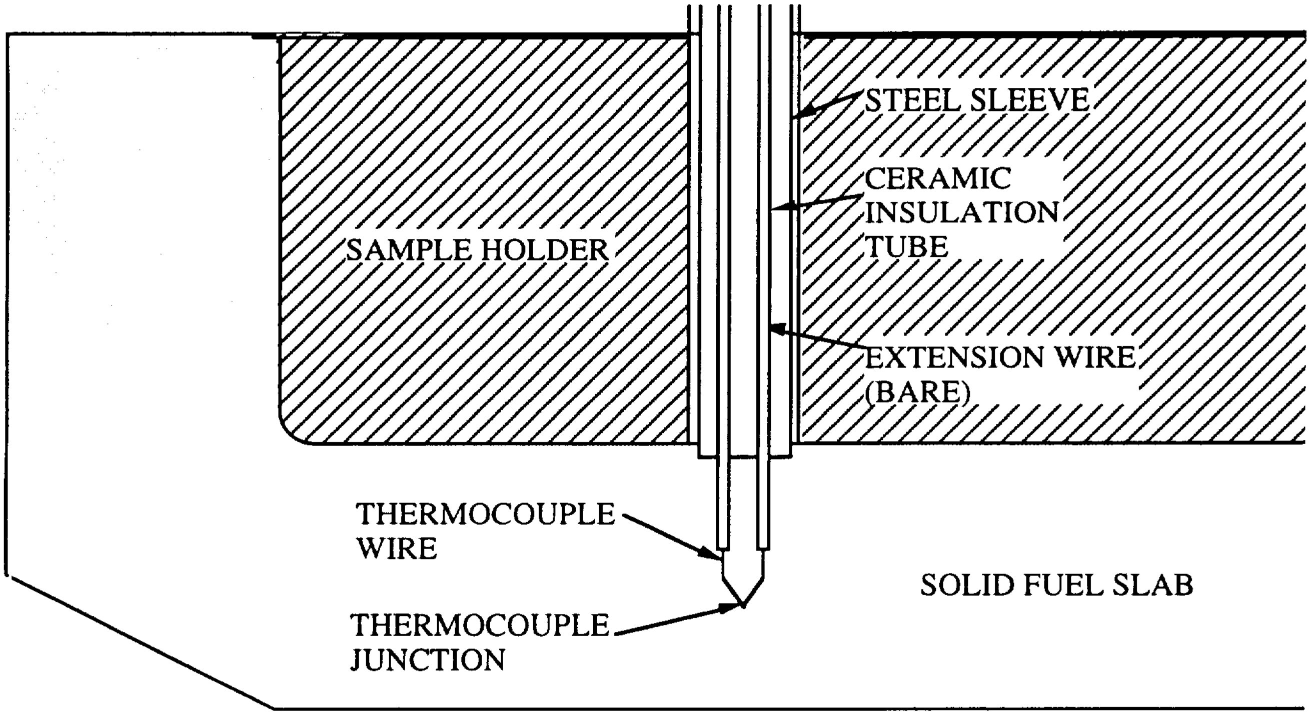

Figure I.3.5 Schematic diagram of a thermocouple assembly

Half of the fuel slab holders were manufactured with thermocouple ports, as shown in Figure I.3.5. Ports were placed at centerline positions corresponding to 2.5″, 5.5″, 8.5″, 11.5″, 14.5″, 17.5″, and 21.5″ from the leading edge of the fuel slab. Generally, six of the seven ports were used to house thermocouple assemblies while one of the ports was utilized for the ultrasonic transducer feedthrough, discussed in the next section. The use of multiple thermocouples allowed measurement of surface temperature and subsurface thermal wave thickness as a function of axial location along the fuel slab.

I.3.2.3: Regression Rate Measurements

Throughout the experimental program four independent techniques were used to measure the solid fuel regression rate. Table I.3.2 lists the methods used to deduce various forms of the regression rate.

Table I.3.2 Diagnostics used to deduce regression rate

Diagnostic Equipment	Type of r	Description
Mass Balance	r	average over entire slab
Caliper	$r(x)$	time–averaged, axially–dependent
Ultrasonic System	$r(t, x_o)$	instantaneous at a single location, x_o
Real–Time X–Ray	$r(t, x)$	instantaneous, axially–dependent over a region

I.3.2.3.1: Mass Balance Regression Rate Measurement

The global (time– and space–averaged over entire fuel slab) regression rate, r, may be obtained by using a mass balance to weigh the fuel slab both before and after the test firing. Since $m = dM/dt = \rho_f A_b r$ for the solid fuel, the equation

$$r = (m_i - m_f)/\Delta t \rho_f A_b \qquad \text{(I.3.6)}$$

where m_i is the initial solid fuel mass, m_f the final solid fuel mass, Δt the burn time of the test, ρ_f the solid fuel density, and A_b the burning surface area, describes the global regression of the solid fuel slab. The burn time was defined as the time between ignition and GOX shut–off. Both these events are easily distinguished on the pressure–time traces from the various transducers used to measure motor pressure. The solid fuel density is known a priori, and the burning surface area is easily calculated from the known geometry of the fuel slab.

The global regression rate represents the simplest type of regression rate obtainable from a test firing. However, since the global measurement gives no information on either the time or axial dependence of the regression rate, it is also the least useful type of regression rate for deducing correlations. Only simple correlations of the form $r = aG_o^n$ may be obtained.

I.3.2.3.2: Caliper Regression Rate Measurement

The time–averaged, axially–dependent regression rate, r(x), was deduced by measuring the fuel web thickness at various axial stations both before and after the test firing. Since r(x)=dw/dt, where w is the web thickness at a location x,

$$r(x) = (w_i(x) - w_f(x))/\Delta t \qquad (I.3.7)$$

where $w_i(x)$ is the initial and $w_f(x)$ the final web thickness measured by the caliper. Eq. (I.3.7) describes the axially–dependent regression rate at a location x. By making measurements at many axial stations, the time–averaged regression rate profile for a particular test firing was obtained. This type of profile indicates where the time–averaged regression rate increases or decreases with respect to axial location.

I.3.2.3.3: Ultrasonic Regression Rate Measurement

The ultrasonic transducer system allows one to measure the *instantaneous* solid fuel regression rate at a particular location along the length of the fuel slab, $r(t, x_o)$. Figure I.3.6 shows a block diagram of the major components of the ultrasonic pulse–echo system. A 1 Mhz–3/4" Panametrics Videoscan ultrasonic transducer (V114–RM) was placed behind the fuel slab within a fuel sample holder. The axial position of the transducer was selected from one of four locations. The transducer emits and receives ultrasound signals, and was connected directly to the Electronic Device for Ultrasonic Measurement (EDUM), acquired from ONERA, France. The EDUM processes the ultrasonic signal. An oscilloscope was connected to the EDUM to provide a real–time visual record of the ultrasonic transducer signal, which was recorded on a video camera during each test run. At the same time, the ultrasonic signal was recorded by the data acquisition unit (Nicolet Multipro Transient Analyzer).

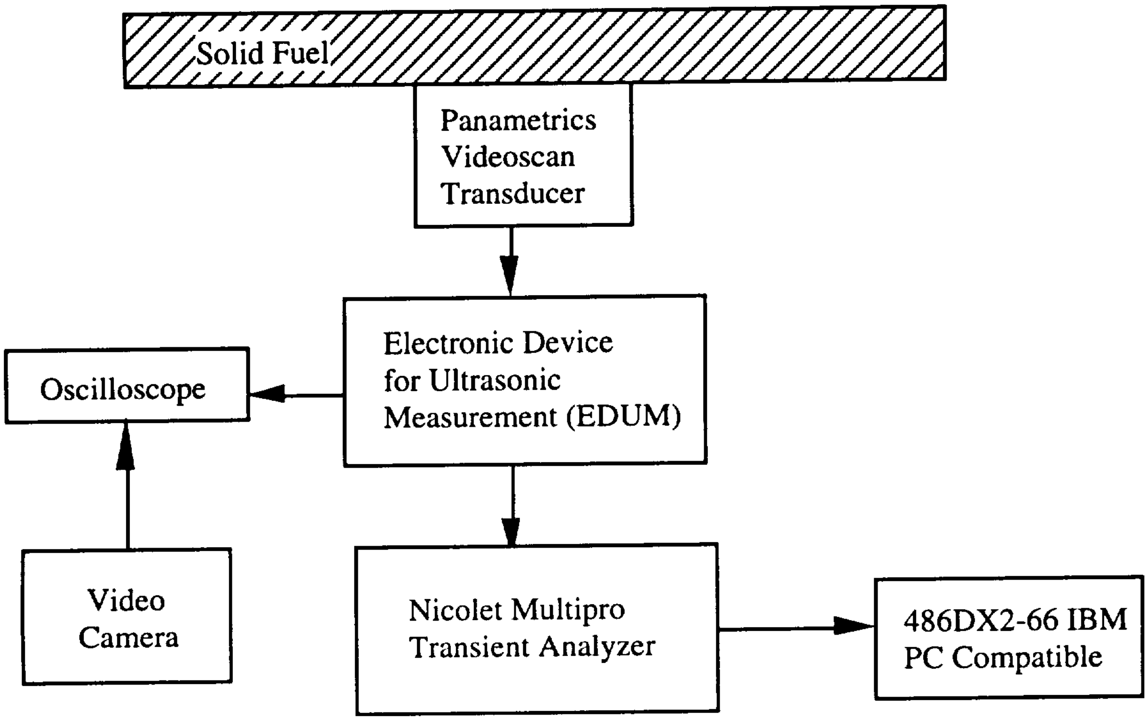

Figure I.3.6 Schematic Diagram of Ultrasonic Pulse–Echo System

Through a pre–test calibration procedure, the ultrasonic transducer's voltage signal was converted to the propagation time of the ultrasound pulse. The propagation time represents the time required for the pulse to travel from the transducer, through the fuel slab to the burning solid–fuel surface, and back to the transducer. As the fuel regressed, the propagation time of the ultrasound pulse decreased continuously due to the reduction of fuel web thickness. Measurement of the time history of this signal allows one to calculate both the instantaneous burned web thickness and the instantaneous regression rate. References [I.17] and [I.28] present in detail the operating principles of the ultrasonic pulse–echo method.

I.3.2.3.4: Real–Time X–Ray Radiography Regression Rate Measurement

The real–time X–ray radiography system was the most useful diagnostic device used to deduce the regression rate. This method allows one to deduce the instantaneous, axially–dependent regression rate r(t,x) over a region of the fuel slab.

Figure I.3.7 shows the schematic diagram of the real–time X–ray radiography system. The motor has two sets of opposing windows. Each window is 280 mm (11 in) long by 44.5 mm (1.75 in) wide for real time X–ray radiography of the solid fuel regression phenomena. During the test, an X–ray tube head emitted high–energy photons which passed through the LEXAN/MXB–360 window assemblies of the motor and then impinged on an image intensifier. Inside the motor, a portion of the X–ray photon energy was absorbed by the solid fuel when X–ray photons passed through the fuel slab region; however, the photons which passed through the port area experience little absorption. Because of this difference in the attenuation of the X–ray photons, the X–ray images displayed contrasting bright and dark regions, which showed the port area and fuel slabs, respectively. The instantaneous fuel web thickness was then deduced from these images using NIH image processing software. The principles of X–ray diagnostics of condensed phase combustion processes are given in Ref. [I.29]

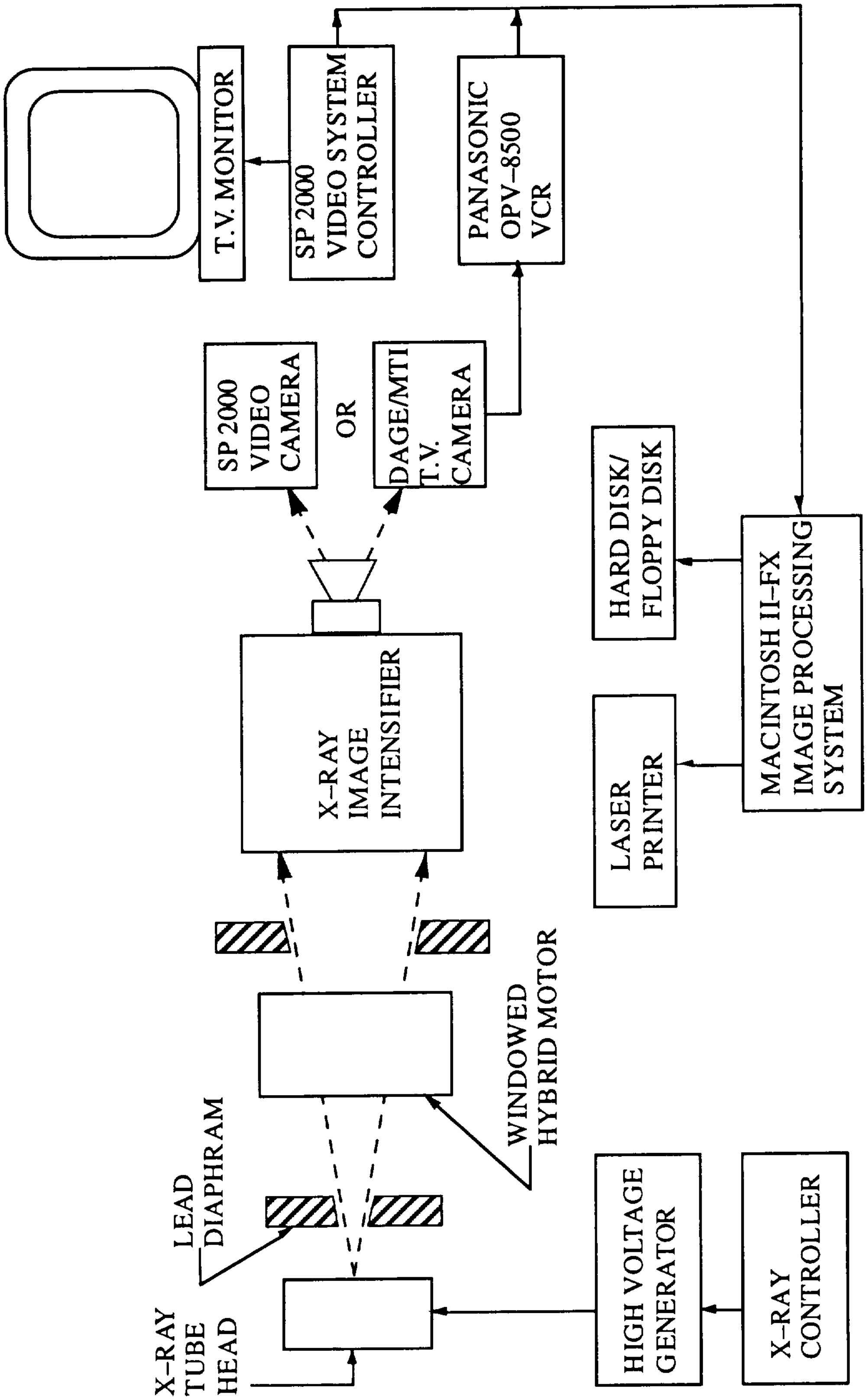

Figure I.3.7 Schematic diagram of real-time X-ray radiography system

Figure I.3.7 Schematic diagram of Real-Time X-Ray Radiography System

In order to obtain the corresponding instantaneous regression rate at a particular x location, the data is fit with an equation of the form

$$w(x) = a + bt^{m} \tag{I.3.8}$$

where w(x) is the instantaneous regressed web thickness at x, t is time, and a, b, and m represent the constants to be determined. The power–law form of Eq. (I.3.8) generally fits the data quite well. Taking the time derivative of Eq. (I.3.8) yields the regression rate:

$$r(x) = bmt^{m-1} \tag{I.3.9}$$

This procedure can be performed at many individual stations along the length of the fuel slabs.

I.3.2.4: Data Acquisition Systems

A few components of the data acquisition system have already been presented in Figs I.3.6 and I.3.7 when discussing the ultrasound and X–ray systems. Figure I.3.8 shows a schematic diagram of the overall data acquisition system utilized during each test firing. The overall system consists of two separate components: one used to collect digital data and one used to record video images. The digital component consisted of the ultrasonic transducer, all types of pressure transducers, and thermocouples connected to the Nicolet Multipro Transient Analyzer, which includes a 16 channel data acquisition board linked to an IBM compatible personal computer and laser printer. This system was used to record and store all digital data. A software package called NicWindows was used to control and trigger the acquisition board and to monitor recorded voltage signals.

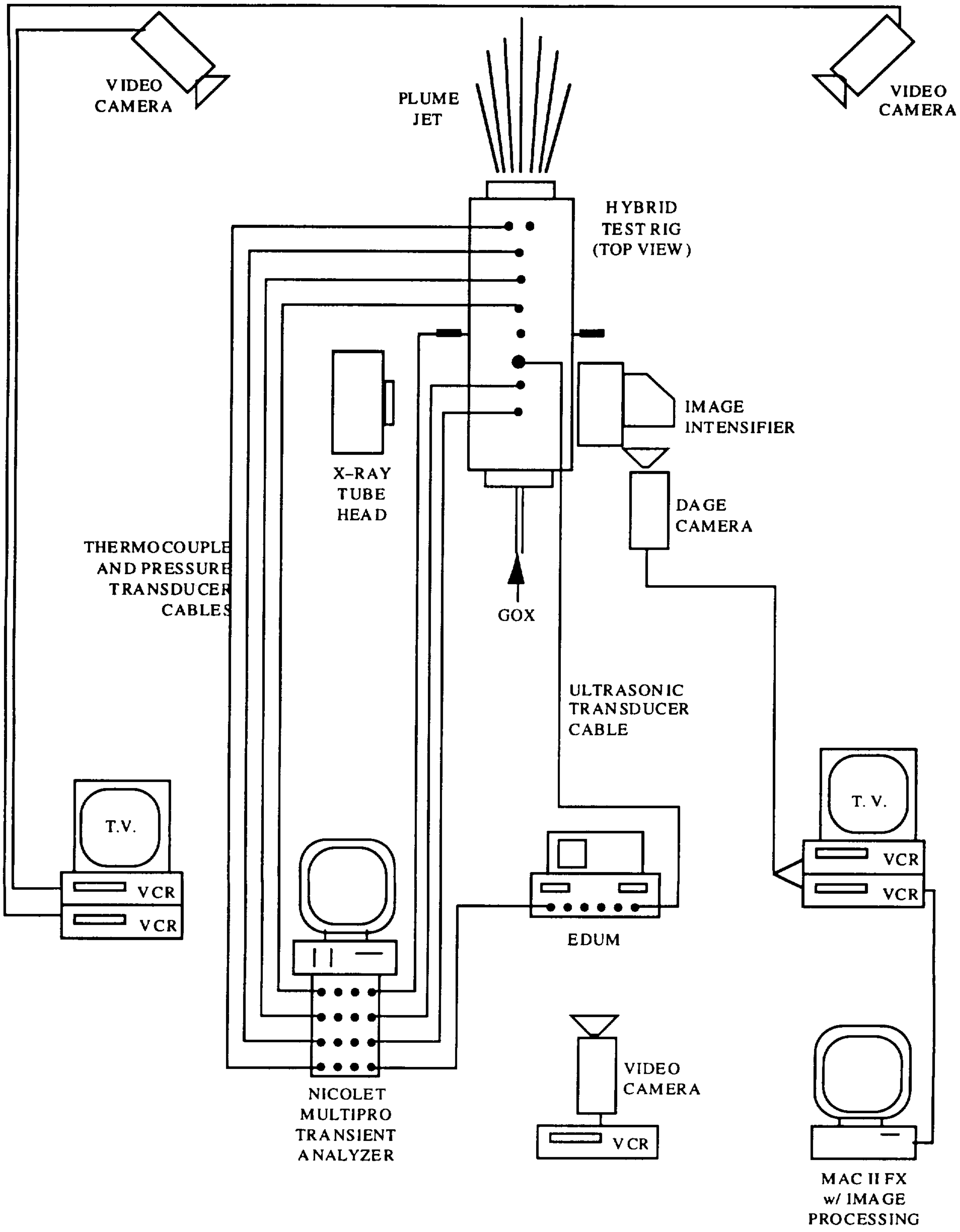

Figure I.3.8 Hybrid test rig data acquisition system

In general, all thermocouples and Setra pressure transducers were recorded at 1000 Hz sampling rate, i.e., the voltage signals transmitted from these instruments to the Nicolet were sampled every 1 ms, or 1000 times a second. The Nicolet controlled the sampling rate of the Setra transducers and thermocouples. The Kistler pressure transducers and ultrasonic transducer were recorded at 5000 Hz to obtain sufficient temporal resolution for their respective measurements. During the analysis of the ultrasonic transducer data (discussed later) it was necessary to have both pressure and ultrasonic signals aligned exactly in time. However, it was not possible to synchronize the sampling of the Nicolet and EDUM, so the EDUM was used to control both the sampling of the Kistler pressure transducers and the ultrasonic transducer by triggering the appropriate channels on the Nicolet with a 5 volt Transistor Transistor Logic (TTL) signal from the EDUM.

The raw voltage data recorded were converted to pressure, temperature, and propagation time signals using appropriate calibration equations obtained prior to the test firings. In some cases, such as for the ultrasonic transducer and Kistler pressure transducers (prone to drift), the calibration procedures had to be performed prior to each test. The Setra pressure transducers required infrequent re-calibrations, while Omega Engineering provided equations to convert thermocouple voltage signals into temperature signals. Digital data was stored in waveform format by NicWindows, then converted to floating-point format using Wave Converter. In this form, the digital data was analyzed and processed using the Matlab software package.

Several video camera/VCR/monitor combinations were used to display and record various images during the test firings. A high-resolution Dage camera and two VCR's recorded the real-time X-ray image of the regressing fuel slabs during the test. Meanwhile, separate video camera/VCR combinations recorded the plume image and EDUM oscilloscope image. The Dage/VCR provided 30 images per second of real-time X-ray data, which were later analyzed using NIH imaging processing software (Image) on a Macintosh II FX personal computer. Other programs such as Excel (primarily for spreadsheet work), Kaleidograph (primarily for graphing), and SigmaPlot (primarily for curvefittng) were used to process and correlate the test data.

I.3.3: Solid Fuel Processing

Hydroxyl–terminated Polybutadiene (HTPB) represents the baseline solid fuel used for all experiments discussed in subsequent chapters. HTPB is a solid polymer made by combining two components: a hydroxyl–terminated homopolymer of butadiene and an isocyanate cross linking agent. The homopolymer used was R–45 M, manufactured and supplied by Elf Atochem, while Isonate 2143 L (modified diisocyanate, MDI), supplied by Dow Chemical, was used as the cross linking agent. Both components are supplied in a liquid state. R–45 M consists of a long, carbon backbone with hydrogen atoms attached along the length. It has an average molecular weight of about 2800. Hydroxyl molecules (OH) terminate the chain at both ends. The chemical formula

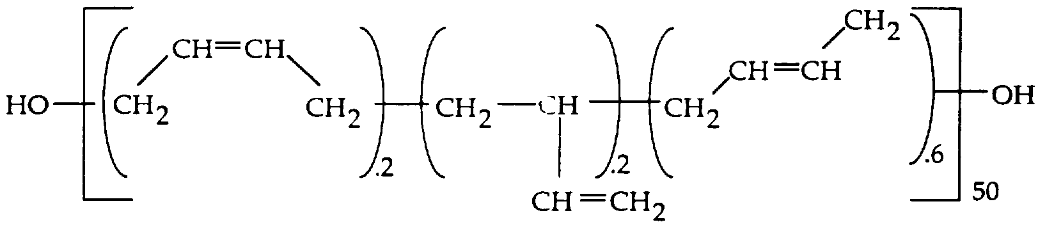

represents R–45 M [I.33]. The first group in parentheses on the left represents the cis 1,4 microstructure, the middle term is the vinyl 1,2 microstructure, and the rightmost group is the trans 1,4 microstructure. In the overall 50–mer chain, the trans arrangement is the dominant microstructure, making up about 60% of the groups, while the cis and vinyl arrangements each constitute about 20% of the chain. All three microstructures are unsaturated since two additional hydrogen atoms could be added in the absence of the carbon double bond. When mixed with R–45 M, the NCO groups that terminate the Isonate 2143L chain bond with the OH molecules to form NCO_2H. Thus, the polymer chains link to form solid HTPB. The chemical formula

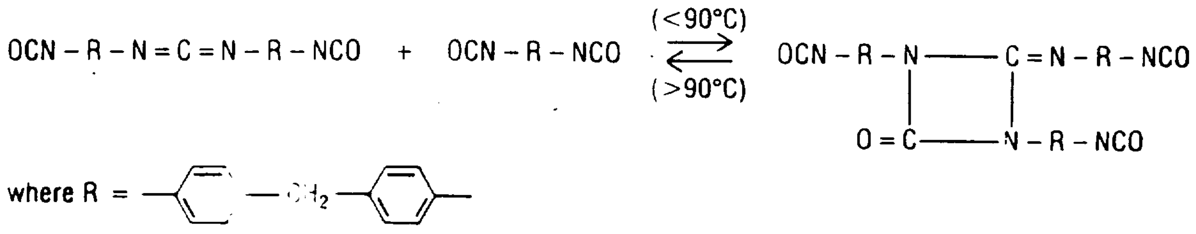

represents Isonate 2143 L [I.34].

One may determine the proper mixture ratio of Isonate 2143 L to R–45 M using the equation

$$\frac{\text{MASS OF 143L}}{\text{MASS OF R-45M}} = 1.05\frac{eq_{NCO}}{eq_{OH}}\ 0.73\text{x}10^{-3}\frac{eq_{OH}}{g_{R\text{-}45M}}\ 144.5\frac{g_{143L}}{eq_{NCO}} = 0.11 \qquad (I.3.10)$$

The factor of 1.05 ensures that enough Isonate 2143 L is present to cure the polymer since the process is not 100% effective. Performing the calculation shows that an amount of properly cured HTPB should be composed of about 89.79% R–45 M and 10.21% Isonate 2143 L by weight.

When processing fuel slabs, the proper amounts of each component are first determined then poured into glass beakers for weighing on an electronic balance. The R–45 M and Isonate 2143L are then mixed under vacuum for about 10 minutes. The purpose of mixing the fuel components in a vacuum is to remove any bubbles that would occur during the pouring and mixing processes. After mixing, the liquid fuel is poured into the fuel mold. The entire assembly is then placed in a vacuum tank for about 30 minutes to help remove any remaining bubbles.

Several test firings utilized fuel slabs containing additives of carbon black powder or ultra fine aluminum powder (UFAL). The carbon black power had a mean particle size of 75 nm. Carbon black represents a commonly used solid fuel opecifier which should cause all or nearly all gas–phase radiation to be absorbed on the solid fuel surface rather than in the slab interior. The ultra–fine aluminum powder (called Alex by Russian scientists) was added to evaluate its effects as a possible regression rate enhancing agent. UFAL is manufactured in Siberia by exploding thin aluminum wires in an argon environment. The UFAL powder had a particle size of 50 to 100 nm [I.30].

When processing fuel slabs containing these additives, the powder was first added to the liquid R–45 M and mixed under vacuum for about 10 minutes to ensure even particle distribution through the homopolymer. After the initial mixing, Isonate 2143L was added to the powder/homopolymer mixture, and the entire liquid mixed again under vacuum for another 10 minutes.

To conserve on the amount of UFAL used, the UFAL–loaded liquid fuel was cast onto a partially cured layer of pure HTPB and allowed to cure. Excellent bonding between the two material layers was achieved when the pure HTPB layer is allowed to partially cure for about 3 hours before pouring the second layer containing UFAL powder.

I.4 Data Analysis and Experimental Results

This Section concerns the data analysis procedures and results of the experimental method of approach presented in Section I.3. Separate sections discuss the approach taken to deduce the individual parameters of interest, including motor pressure, solid fuel temperature, and various types of regression rate. Correlations of experimental data are presented which relate the regression rate to various operating conditions and geometric parameters.

Table I.4.1 summarizes the conditions of the test firings discussed below.

Table I.4.1 Summary of test firings

Test No.	Fuel	$G_{ox,0}$, kg/m^2-s (lb/in^2–s)	Pressure, Mpa (psia)	Burn Time (s)	r_{global}, mm/s (in/s)
1	HTPB	337.8 (0.48)	8.55-2.31 (1240–335)	15.0	-
2	HTPB	68.3 (0.10)	2.07-2.05 (300–300)	2.7	-
3	HTPB	125.3 (0.18)	3.45-2.48 (500–360)	3.6	-
4	HTPB	166.8 (0.24)	8.96-1.79 (1300–260)	5.8	-
5	HTPB	158.3 (0.23)	5.31-2.82 (770–410)	4.1	1.4 (0.055)
6	HTPB	133.3 (0.21)	3.89-1.34 (565–195)	6.6	0.92 (0.036)
7	HTPB	102.3 (0.15)	3.65-1.72 (530–250)	8.9	0.76 (0.030)
8	HTPB	100.7 (0.15)	3.45-1.72 (500-250)	9.5	0.76 (0.030)
9	HTPB HTPB +0.25% cb	113.5 (0.30)	3.45-1.72 (500-250)	4.2	1.2 (0.047)
11	HTPB +0.25% cb HTPB	162.3 (0.23)	4.93-1.24 (715-180)	8.5	0.95 (0.037)
12	HTPB+4% UFAL HTPB	196.9 (0.29)	3.72–2.07 (540–300)	4.0	1.13 (0.045); 1.29 (0.051)
13	HTPB+12% UFAL HTPB	234.5 (0.35)	4.31–1.86 (625–270)	4.5	1.24 (0.049); 1.49 (0.059)
14	HTPB+20% UFAL HTPB	220.5 (0.33)	4.14–2.14 (600–310)	4.4	1.28 (0.050); 1.57 (0.062);
15	HTPB	362.5 (0.54)	4.96–1.52 (720–220)	7.2	1.376 (0.054)
16	HTPB				
17	HTPB	369.9 (0.56)	4.62–1.52 (670–220)	6.1	1.429 (0.056)

*cb represents carbon black

The pressure ranges given in the fourth column correspond to the maximum motor pressure and the minimum motor pressure just before shut down by terminating the GOX flow. The pressure drop was due mainly to erosion of the graphite nozzle throat. Test No. 4 has an unexpected maximum pressure level of 9 MPa caused by a momentary blockage of the nozzle by a piece of solid fuel torn from the fuel slab. After this test, extension pins were mounted to the ends of the fuel sample holders to provide extra support for the solid fuel slabs, which prevented the problem from recurring. The third column of Table 4.1 gives the initial GOX mass flux found by dividing the known GOX mass flow rate by the initial inlet combustor port area. The last column gives the global regression rate of each test. Test No. 5 has a relatively high regression rate due to the large pressure oscillations observed during this test firing. Others have reported similar finding for tests with substantial pressure oscillations [I.17]. Test Nos. 9 and 11 were conducted using one translucent fuel slab and one fuel slab with 0.25% wt carbon black. Test No. 10 was conducted using a totally different solid fuel, and therefore is not included in this Table. Test Nos. 12, 13, and 14 were conducted using one pure HTPB slab and one fuel slab processed with UFAL weight fractions of 4, 12, and 20%, respectively.

I.4.1: Overall Data Analysis Procedure

Two separate combinations of software packages were employed to analyze and correlate the test data obtained from the diagnostic instruments and data acquisition systems described in Section 3. Figure I.4.1 illustrates a flow chart which describes the interaction of the different commercial software packages used. The NicWindows/Matlab combination was used to analyze all digital data recorded by the Nicolet Multipro Transient Analyzer. These two programs were used on the Multipro PC (an IBM–compatible computer). NicWindows is basically a front–end program allowing the user to interact with the Nicolet Multipro Transient Analyzer. All acquired raw data, in the form of instantaneous voltage signals from the pressure transducers, thermocouples, and the ultrasonic transducer, was stored in the Multipro acquisition board using NicWindows. The data, stored in waveform format was exported to Wave Converter for converting recorded waveforms into floating point (ASCII) format. The converted files were then opened in Matlab.

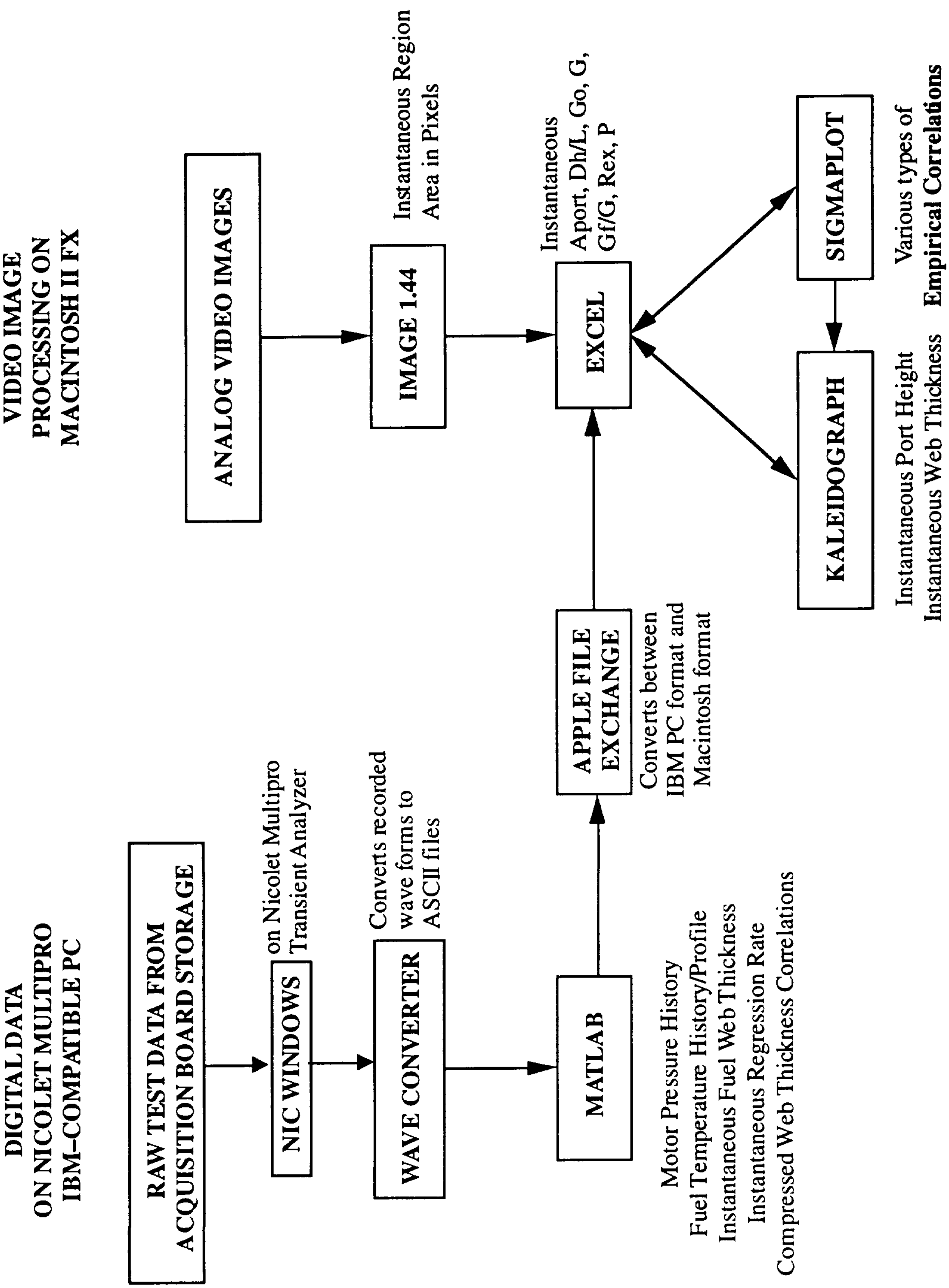

Figure I.4.1 Data processing flow chart

Matlab is an extremely useful software package that can be used for many diverse applications. Since it can easily import a large amount of raw test data directly from hard disk storage, Matlab proved very convenient for converting the voltage–time signals into pressure–time traces, temperature–time traces, and instantaneous web thickness data. Though Matlab can be operated entirely in a real–time interactive mode, repetitive tasks were more efficiently accomplished by writing computer codes in the Matlab "Notepad" editor. Essentially, the data were imported then split into two different matrices—one representing the voltage signal and the other representing the time signal. The voltage signal was then converted to either a pressure signal or a temperature signal using an appropriate conversion equation. This data could then be plotted or saved on a 3.5" diskette for transport to the Macintosh II FX using the Apple File Exchange program, which converts the files from PC to Macintosh format.

The real–time X–ray video images were reduced to instantaneous port height data and instantaneous web thickness data using commercial software on the Macintosh II FX. This type of analysis proved more labor intensive than analysis using Matlab since the video images represent a type of analog data. The particular data analysis procedure used to obtain regression rate data from the real–time X–ray radiography system is discussed separately in a later section.

I.4.2: Motor Pressure Results

As described in Section I.2, Kistler pressure transducers measured dynamic motor pressure, while Setra transducers measured quasi–steady motor pressure. During data analysis, pressure was treated as an instantaneous, global quantity—i.e., only temporal variations in the motor pressure were considered. Thus, p is equal to p(t) only, and the instantaneous pressure was assumed to be the same everywhere in the motor. This assumption was verified to be very reasonable by pressure transducer data obtained at different locations of the motor.

Both types of pressure transducers produce a voltage signal which was recorded by the Nicolet Multripro Transient Analyzer. Using a pre–test calibration procedure the voltage signals were converted to pressure–time traces after the test firings using linear equations of the form

$$P(t) = A + B^{*}V(t) \qquad (I.4.1)$$

where P(t) represents the deduced instantaneous pressure expressed in psia, V(t) the measured instantaneous transducer voltage signal, and A and B constants determined empirically via the calibration procedure.

Figure I.4.2 shows a pressure–time trace of the hybrid motor during Test No. 2. The initial jump in pressure at about 0.2 seconds was caused by the start of GOX flowing through the supply line and into the hybrid motor. At a time of approximately 1.5 sec., the onset of ignition was achieved and flame began to spread over the solid fuel. Within about 0.5 seconds the chamber filling process was finished. At about 2.0 seconds after the start of the test, the motor reached a quasi-steady state operating condition of about 2.07 MPa (300 psia). During this period significant pressure oscillations, on the order to ±20% of the mean pressure, occurred. At about 4.3 sec., the GOX flow was shut off and the nitrogen purge was activated. The total time of combustion for this run was about 2.5 seconds.

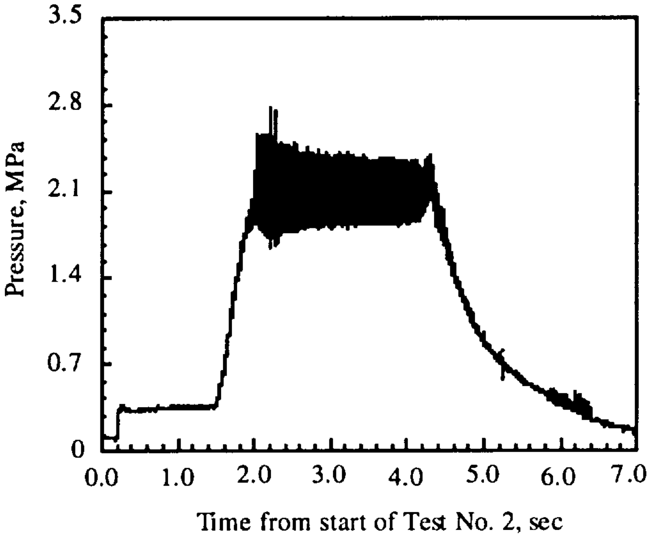

Figure I.4.2 Pressure time trace from Test 2

Figure I.4.3 shows the frequency spectrum of the pressure oscillations. The combustion instability was observed in longitudinal modes. The fundamental (first) mode of oscillation occurred at a frequency of about 53 Hz, with a second mode at 106 Hz.

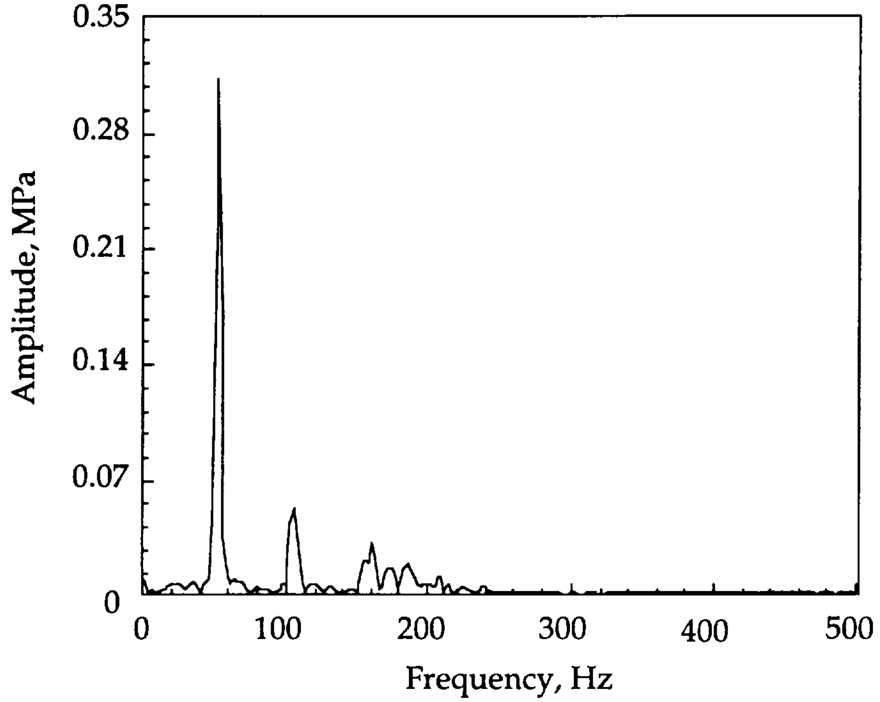

Figure I.4.3 Pressure oscillation frequency spectrum

Similar to Test No. 2, significant pressure oscillations were observed in Test No. 1, 3, and 4. The major source of combustion instability was not fully determined at the end of these tests; however, it was speculated that the acoustic coupling between the GOX feed–line and combustion chamber could be responsible for the observed phenomena. Considering the distance between the choked venturi throat and the injector face of the combustion chamber, the calculated acoustic frequency in this equivalent 1/4–wave tube was around 50 Hz—very close to the fundamental mode frequency of 53 Hz. This close agreement seemed to indicate that the source of instability was associated with acoustic characteristics of the GOX supply line. Therefore, the following major modifications to the GOX supply line were made in order to eliminate the undesirable combustion instability phenomena:

1. A section of steel tubing in the GOX supply line between the venturi and the motor inlet was replaced. The new section was shaped in the form of a loop with a diameter of 40.6 cm (16 in). The effective length of the GOX supply line was increased to verify the dependence of the oscillation frequencies on GOX supply line tube length. It was seen in Test No. 5 that the frequencies of the first and second longitudinal modes of oscillation were reduced to 40 and 86 Hz by the

increase of GOX supply line length. The amplitude of oscillations for this run was also reduced to less than ±10%. This finding verified that the pressure oscillations in the motor were closely linked to the GOX supply line.

2. To further decouple the pressure wave transmissions between the motor and GOX supply line, and to damp out major pressure oscillations, a 6.35 cm (2.5") long orifice with inner diameter of 0.94 cm was added to the GOX supply line just upstream of the motor inlet. Since the GOX supply line had an inner diameter of 1.57 cm, the long orifice provided an area blockage ratio of about 65%.

Results from Tests 6 and 7 showed that these two modifications successfully eliminated the combustion instability problems encountered in earlier tests of the hybrid motor system. Figure I.4.4 shows the p–t trace of Test No. 6, which was conducted after both the loop and long orifice were installed. The pressure oscillations dropped to only about ±1% and ±1.5% of the mean pressure during Test No. 6 and 7, respectively. The chamber pressure showed significant decay after the attainment of the peak pressure in Fig. I.4.4. This decay was caused by erosion of the graphite nozzle throat.

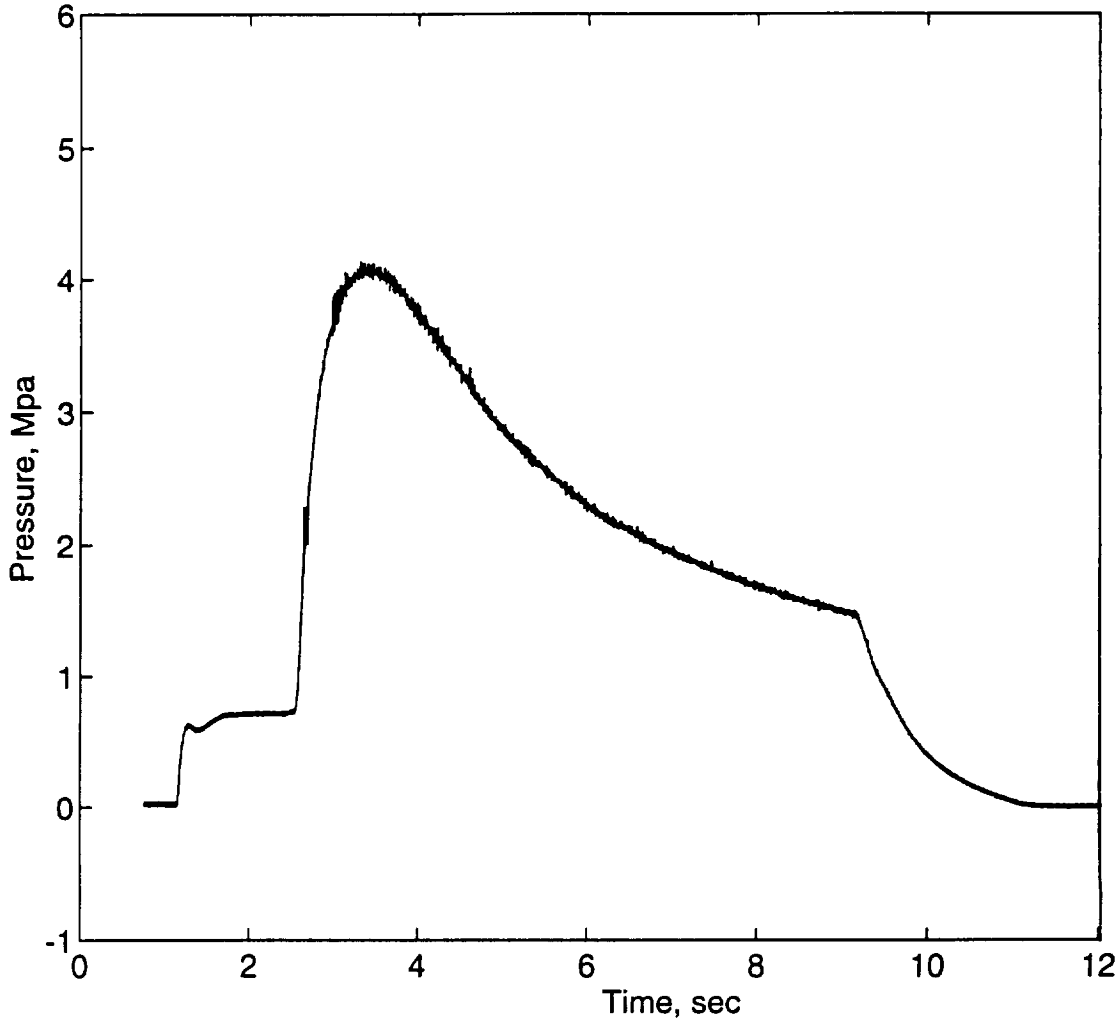

Figure I.4.4 Pressure time trace from Test 6

Since combustion instability phenomenon did not represent the major focus of this study, no further attempt was made to examine the motor pressure oscillations observed in the early test firings.

I.4.3: Solid Fuel Temperature Results

All solid fuel surface temperatures and subsurface thermal wave profiles reported here were measured using 25 μm Pt/Pt-10%Rh (S-type) fine-wire thermocouples. The fine-wire thermocouples were manufactured at the High Pressure Combustion Lab using commercially purchased supplies.

Solid fuel surface temperature was measured at several axial locations by embedded fine–wire thermocouples. In other words, T_s was equal to $T_s(x_i)$, where x_i corresponds to the particular axial location of the thermocouple. Since the thermocouple could not move with the burning surface during the test, it provided a surface temperature measurement at only one instant during the test. However, the subsurface temperature measurement represents a profile measurement at a particular location by converting the temperature–time trace to $T(z,x_i)$, using the time–averaged regression rate, r_{avg}, at x_i obtained from the micrometer measurement technique described in Section I.3. The magnitude of z represents the depth measured from the burning fuel surface. The coordinate z was defined as negative in the solid fuel and positive in the gas–phase.

Like the Kistler and Setra pressure transducers, the fine–wire thermocouples produce a time–dependent electric potential which is recorded by the Multipro. This voltage signal was converted to a temperature signal using a 9th–order polynomial expression provided by the thermocouple material supplier, Omega Engineering.

Figure I.4.5 shows a temperature–time trace obtained using a 25 μm fine–wire Pt/Pt–10%Rh thermocouple embedded at 292 mm (11.5 in) from the leading edge of the upper fuel slab in Test No. 5. The thermocouple registered the ambient temperature for the first 0.6 second of the test run then began to register higher temperatures as the fuel surface regressed toward the thermocouple junction. The temperature profile increased smoothly until a temperature of around 1000 K was reached. Beyond the burning surface, the temperature profile undertook a rough, jagged shape in the gas–phase region, where the thermocouple bead location can be affected by cross flow of partially burned gases. The burning surface temperature was determined by curve fitting the subsurface temperature data, using an exponential equation. The obvious departure point was selected as the surface location. Usually, the temperature gradient exhibited abrupt changes at the surface location.

The thermocouple was destroyed when it reached a temperature of around 1700 K at approximately 1.35 s. According to Ref. [I.31], the maximum temperature sustainable by the S–type thermocouples is around 1750 K.

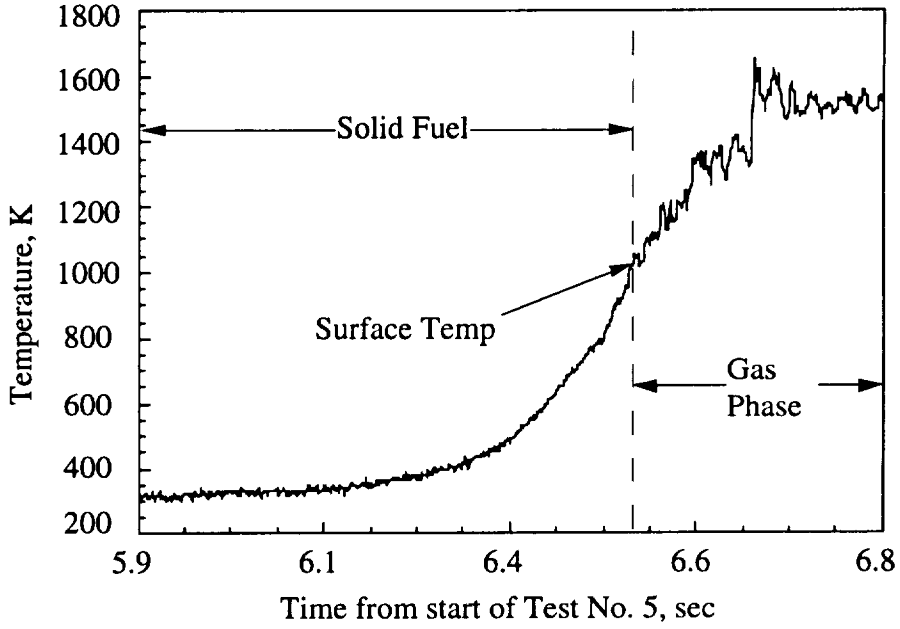

Figure I.4.5 Temperature–time trace for Test 5.

Figures I.4.6a and I.4.6b show a pair of temperature–time traces recorded at two different axial locations (x = 14.0 and 44.5 cm measured from the front edge of the sample) during Test 6. In Fig. I.4.6a, the upstream thermocouple displayed several temperature plateaus between 4.25 and 4.5 seconds. The first plateau corresponds to a temperature of about 900 K, which is believed to be the temperature of the melt layer covering the regressing solid fuel surface. This temperature plateau is associated with the passage of the thermocouple junction through the surface melt layer beneath the boundary layer. The local Reynolds number based upon axial distance is around 5.1×10^5, indicating the beginning of transition to turbulent boundary layer.

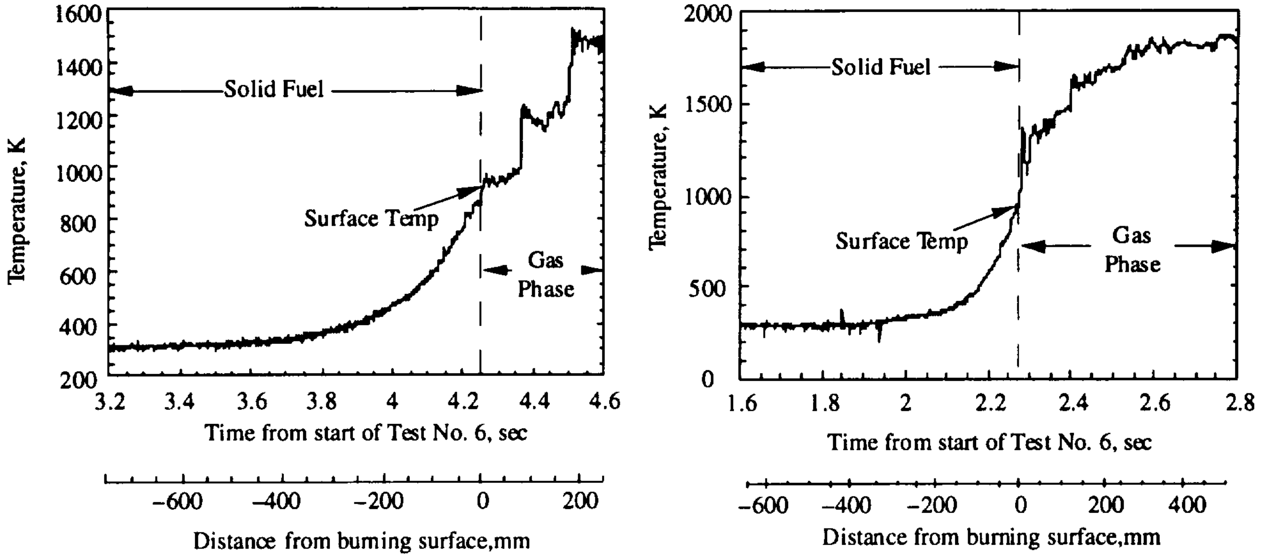

(a) Upstream Location (x=14 cm)

(b) Downstream Location (x=44.5 cm)

Figure I.4.6 Fuel temperature results for Test 6

Comparing the temperature–time trace in Fig I.4.6b with the upstream one (shown in Fig. I.4.6a), it is apparent that the surface heat feedback from the gas phase is much stronger for the turbulent boundary–layer zone due to the increased mass flux in the axial direction and transverse motion of turbulent eddies. Thus, the surface temperature is higher, about 950 K, and the thermal profile in the subsurface region is steeper. The thermal wave thickness deduced for the upstream thermocouple was approximately 400 μm, while that at the downstream is about 250 μm. Corresponding to the higher energy feedback, the surface regression rate toward the rear end of the fuel slab was higher than that of the front section.

Similarly, Figs. I.4.7a and I.4.7b compare two fine–wire thermocouple traces recorded at upstream (x = 6.4 cm) and downstream (x = 52 cm) locations of the top fuel slab from Test No. 7. Again, the temperature profile recorded by the upstream thermocouple (definitely located in a laminar boundary layer covered station) shows a much thicker thermal wave (about 400 μm) than that of the downstream thermocouple (about 200 μm). The surface temperature in the upstream location, about 950 K, is lower than that of the downstream location, around 1000 K. Correspondingly, the fuel slab at the upstream location has a lower regression rate than that of the downstream.

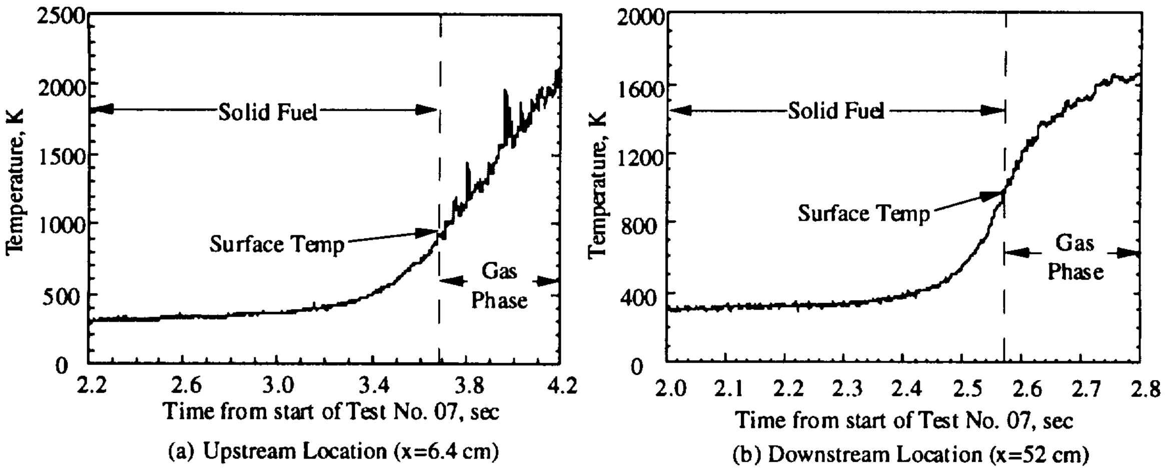

(a) Upstream Location (x=6.4 cm)

(b) Downstream Location (x=52 cm)

Figure I.4.7 Fuel temperature results for Test 7

The surface temperature, subsurface temperature profile, and heat flux to the solid fuel surface can also change substantially with operating conditions, as shown in Figure I.4.8. Figure I.4.8 compares the temperature profiles from Test Nos. 6 and 17. Test No. 6 (initial GOX flux of 148 kg/m^2–s), has a surface temperature of 950 K and a thermal wave about 0.125 mm thick while Test No. 17 (initial GOX flux of 394 kg/m^2–s), has a higher surface temperature of about 1018 K and a thinner thermal wave of about 0.065 mm. In addition, the calculated heat flux into the fuel at the surface for Test No. 6 is 718 kW/m^2, which is much lower than the value of 1500 kW/m^2 for Test No. 17 with much stronger convective shear flow.

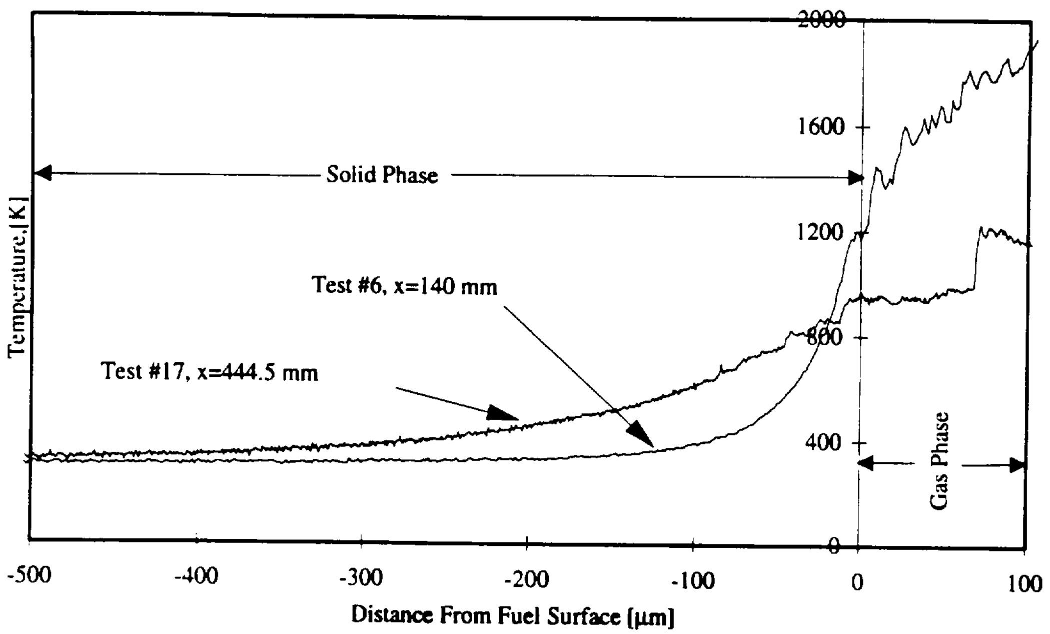

Figure I.4.8 Fuel temperature variation with operating conditions

I.4.4: Solid Fuel Surface Characteristics

The recovered fuel surfaces also exhibit the transition from laminar to turbulent boundary layer with very distinct roughness patterns shown in Figs. I.4.9a through I.4.9c. In the upstream region, the solid fuel has a very smooth surface due to melt layer coverage. In the transition region surface striations (ripples) running in the transverse direction are clearly visible. In the downstream turbulent region, the surface roughness is greater in magnitude with a highly random pattern. Due to the high rates of heat feedback, the melt layer may or may not exist in the turbulent boundary–layer region. The solid fuel could readily pyrolyze into gas–phase products without going through a liquefaction process.

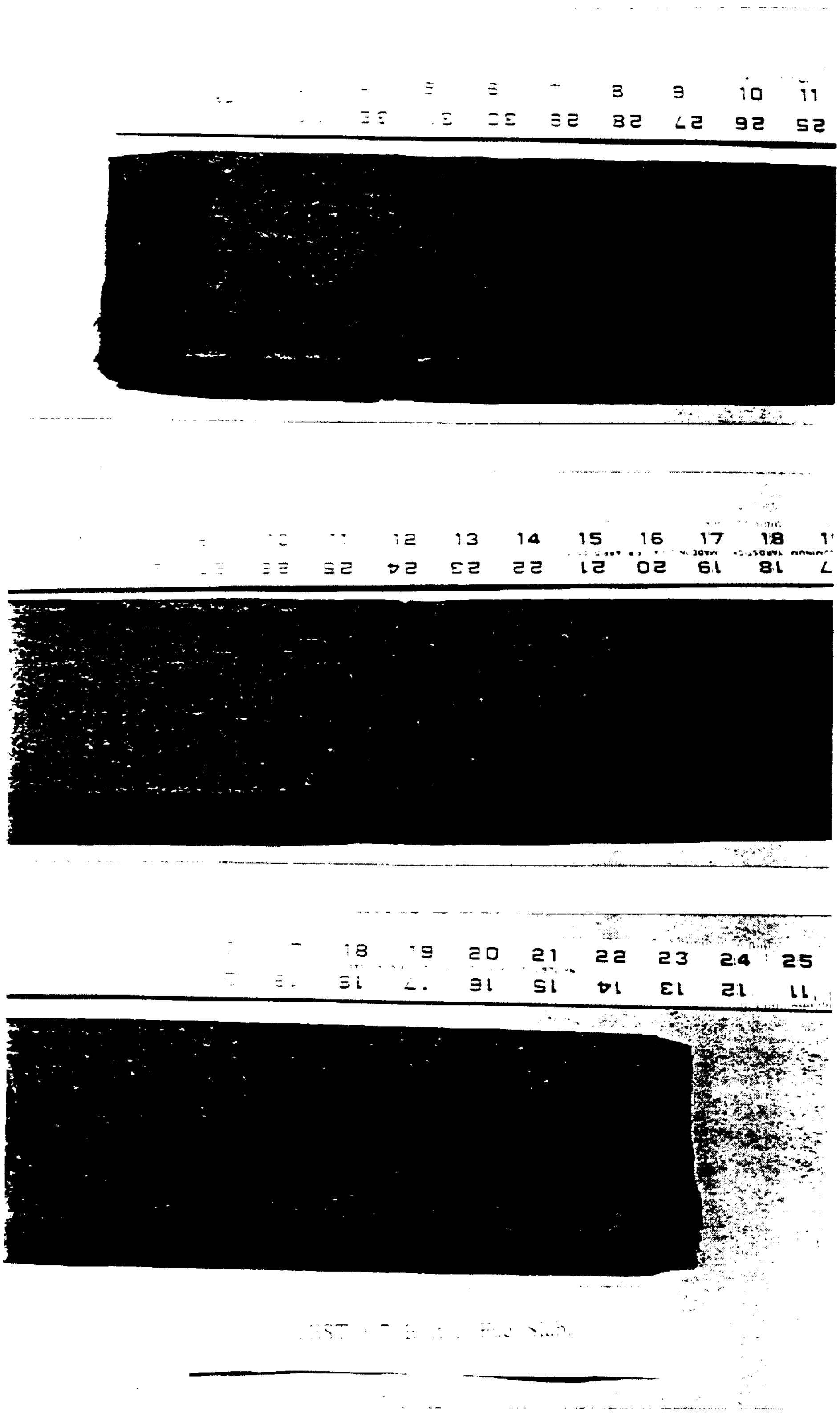

Figure I.4.9 Recovered fuel sample surface for Test 11

I.4.5: Instantaneous Regression Rate Results

As discussed previously, both ultrasonic pulse–echo and real–time X–ray radiography were used to determine solid fuel instantaneous regression rates. The data analysis procedure and results of these two independent methods are discussed separately below.

I.4.5.1: Ultrasonic Pulse–Echo System Regression Rate Results

The ultrasonic pulse–echo system provides an instantaneous web thickness and regression rate measurement at a single location along the centerline of the top fuel slab. In this case, $r=r(x_o,t)$, where x_o indicates that the measurement occurs at a specific location. The ultrasonic transducer was placed at one of four locations: 6.9, 9.9, 13.1, or 16.1 in downstream from the front edge of the fuel slab.

In order to obtain accurate data from the ultrasonic system, the EDUM must be properly adjusted prior to each test according to the particular fuel slab initial web thickness, initial GOX mass flux, and expected burn time during the test. Since all these factors may vary from test to test, the system had to be recalibrated whenever adjustments to the EDUM were made in order to obtain the correct relationship between output voltage and the propagation time of the ultrasonic pulse through the fuel slab.

The examination of data from ultrasonic pulse–echo measurements (and real–time X–ray radiography) indicated that the chamber pressurization and depressurization processes affected the web thickness and regression rate results. The top portion of Fig. I.4.10 shows the time histories of motor pressure and displaced web thickness (by mechanical deformation and burning) for Test 9, while the regression rates deduced from ultrasonic measurement are shown in the bottom portion of the figure. The dashed curve indicates the uncorrected regression rate deduced directly from the ultrasonic measurement device, while the solid curve represents the corrected regression rate found by considering the mechanical deformation of the fuel slabs under pressure excursions. The correction procedure is discussed below. The ultrasonic transducer was located at 178 mm downstream from the leading edge of the fuel slab. The times of GOX flow initiation, ignition of the solid fuel slabs, and GOX flow termination are indicated on the graph. Notice that at the start of GOX flow, but *before* ignition, the web thickness decreased due to the chamber pressurization, yielding a corresponding artificial regression rate of the fuel slab. This artificial regression rate reached a peak value of 0.9 mm/s, and then fell back to zero as the chamber pressure reached a steady level of about 0.6 Mpa.

This change of solid fuel web thickness and regression rate were not caused by burning, but induced by the mechanical compression of the fuel slabs. Since the motor underwent relatively rapid pressurization at ignition, the regression rates at the start of the tests were greatly influenced by the compression process. When the GOX flow was terminated, the motor underwent a depressurization process which caused an apparent increase in the instantaneous web thickness (not shown in the figure) and a *negative* regression rate. These effects are also due to solid fuel deformation during the pressure excursions.

In order to separate the effects of mechanical compression and true regression due to combustion, several calibration tests were conducted using cold flow to characterize the mechanical deformation behavior of the HTPB solid fuel slabs. A simple correlation was developed to relate the change in propagation time of the ultrasonic signal through the solid fuel with chamber pressure:

$$\Delta\tau/\tau_o = 1.3893\text{x}10^{-5} + 3.476\text{x}10^{-3}P - 7.1371\text{x}10^{-5}P^2 \qquad \text{(I.4.2)}$$

where p is measured in Mpa. In Eq. (I.4.2), $\Delta\tau$ represents the change in propagation time due to pressurization, and τ_o is the propagation time at the reference pressure of 0.1 Mpa. As discussed in Ref. [I.28], the propagation time of the ultrasonic signal through the solid fuel provides the measurement of the web thickness. This equation was incorporated into the data analysis routine to correct the observed burned web thickness, and therefore the regression rate, for the compression/decompression effect. It should be noted that Eq. (I.4.2) is applicable for quasi–steady conditions. Under highly transient operating conditions, other factors such as pressurization rates and visco–elastic material properties including shear modulus, creep compliance, and Poisson's ratio should be considered in the development of a further refined correction.

The amount of regression rate correction is shown as the difference between the two traces in the lower portion of Fig. I.4.10. The artificial regression rate spike at the onset of GOX flow was not totally eliminated in this test, while in other tests the magnitude of the spike was substantially reduced after the correction.

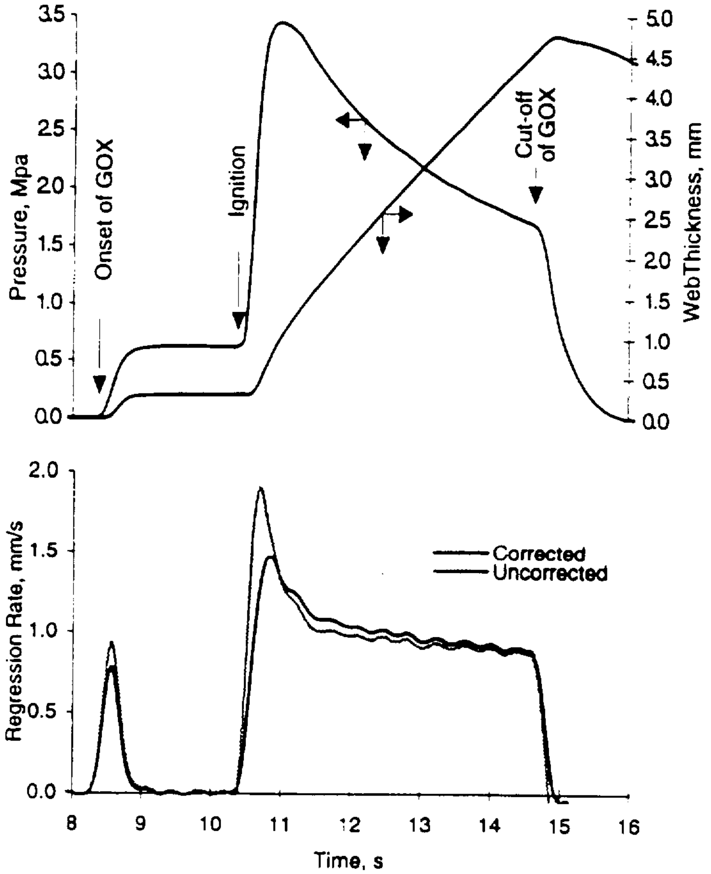

Figure I.4.10 Regression rate correction for ultrasonic system

I.4.5.2: Instantaneous Regression Rate Results over a Region

The real–time X–ray radiography system described previously in Fig. I.3.7 allows the instantaneous regression rate to be measured not only at a single location, as does the ultrasonic pulse–echo system, but over a finite region along the combustor, in the windowed portion. Figure I.4.11 shows a set of typical X–ray radiography images of a portion of the fuel slabs and combustor port distributions at three different times from Test 14. Images similar to these were used to determine the instantaneous web thickness and port cross–sectional area at certain spatial intervals along the fuel slabs. The time resolution between images was around 33.33 ms, while web thickness measurements were made at 12.5 mm spatial increments. The instantaneous regression rates were obtained by processing the fuel web thickness time histories at each axial station.

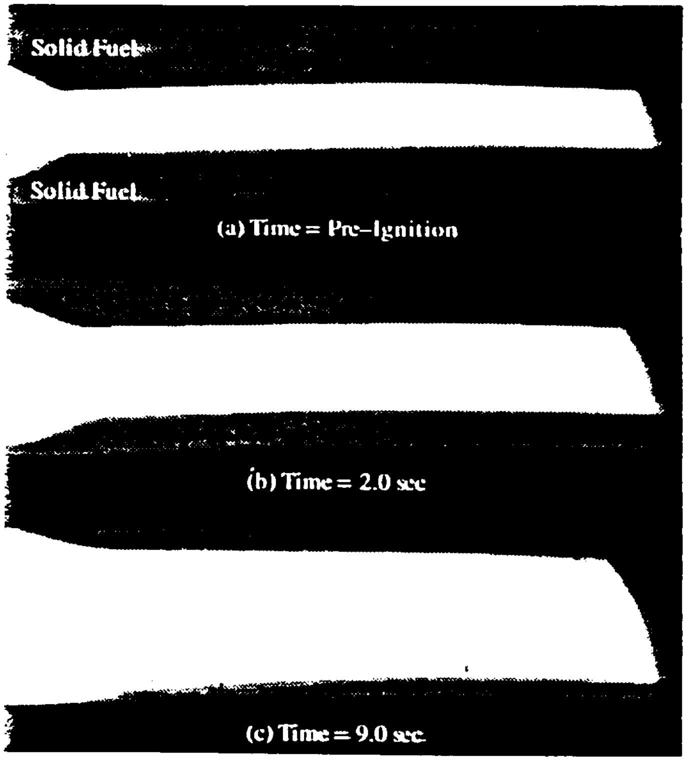

Figure I.4.11 Sample X–ray images from Test 14

Figure I.4.12 shows the chamber pressure time history and the changes in web thickness due to burning (closed triangles), compression, and the sum of both effects (open circles) for Test No. 17 at one axial location. In order to find the web thickness change due to burning alone, the change due to compression was subtracted from the overall change measured from the X-ray images. The change due to compression was found using Eq. (I.4.2), but with the left hand side replaced by $\Delta w_p/w_o$, the strain, which is equivalent to $\Delta\tau/\tau_o$ if there is no change in the speed of sound of HTPB under different pressures. When the variation in speed of sound, c, is important, the relationship between $\Delta w_p/w_o$ and $\Delta t/t_o$ is given by

$$\Delta t/t_o = 1+(\Delta w_p/w_o-1)c_o/c \qquad (I.4.3)$$

where the quantities with subscript "o" represent those at the reference condition (0.1 Mpa). The quantity Δw_p represents the instantaneous web thickness change due to pressure excursions, which can be found since the measured web thickness, w_o, and pressure, p, are known at all times. Therefore, as with the ultrasonic transducer data, the changes in web thickness due to compression and burning can be separated to find the true regression rate due to burning alone.

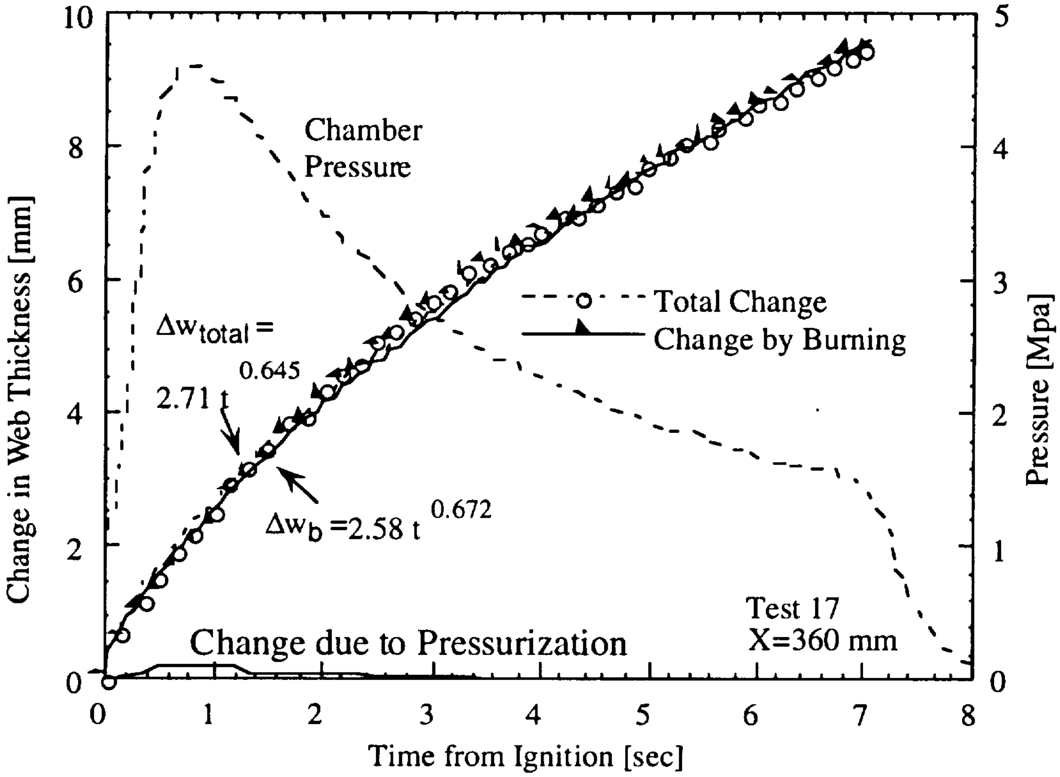

Figure I.4.12 Changes in solid fuel web thickness due toburning and pressurization, from X-ray data

Figure I.4.13 shows the regression rates corresponding to the total observed web thickness change and the change due to burning alone, along with the chamber pressure history. The regression rates were determined by curve–fitting the change in web thickness due to burning, Δw_b, using a power–law equation of the form:

$$\Delta w_b = a + bt^k \tag{I.4.4}$$

which fits the experimental data quite well as shown in Fig. I.4.12. In Eq. (I.4.4), Δw_b is given in (mm) and t is given in (s). The corresponding regression rate is obtained by taking the time derivative of Eq. (I.4.4). Since Δw_b depends on axial location, the constants a, b, and n in Eq. (I.4.4) also depend on axial location.

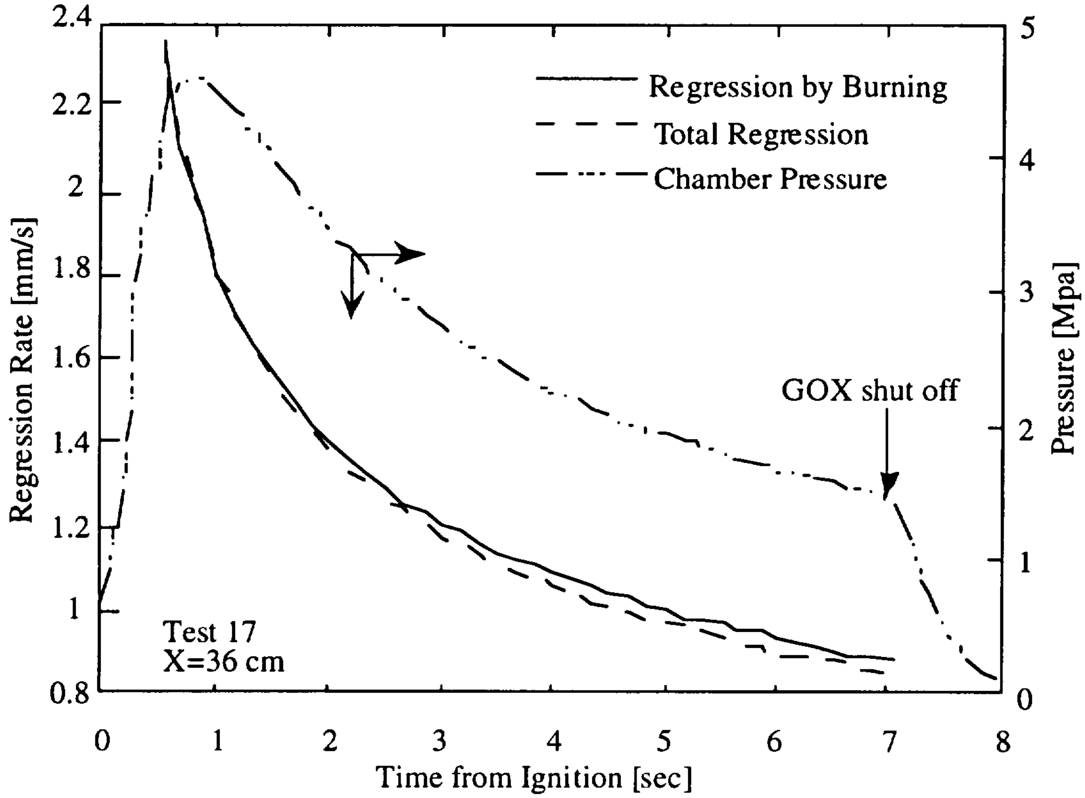

Figure I.4.13 Comparison of corrected and uncorrected regression rates deduced from X–ray data

As the motor is pressurized just following ignition, the change in web thickness due to compression increases since the pressure continues to increase to the maximum pressure. During this time, the change in fuel web thickness due to compression is in the same direction as the change due to burning. Therefore, compression of the fuel slab makes the regression rate appear slightly higher than its true value, until maximum motor pressure is reached. After reaching p_{max}, the motor pressure begins to drop due to erosion of the graphite nozzle and the increase in free volume of the chamber. The fuel slabs begin to expand due to chamber depressurization. During this time, the change in fuel web thickness due to depressurization is in the direction opposite that due to burning, so that X-ray analysis indicates a regression rate lower than the true value for the interval from p_{max} to GOX shut-off. Therefore, the true regression rate due to burning is higher than that given by the uncorrected data during the time between p_{max} and termination of the GOX flow, but slightly lower than that indicated by the uncorrected data over the interval from ignition to p_{max}.

The correction methods for the ultrasonic pulse-echo and real-time X-ray radiography systems discussed above were used to correct all instantaneous regression rate data discussed here. Direct comparison of the regression rates determined by the two independent techniques were made for most of the tests over the time intervals between peak pressure and GOX shut off. The agreement between the two methods is usually within about ±4%. At this point, no attempt has been made to deduce the ignition transient (defined as the time interval between first increase in regression rate and peak regression rate) or the shut-down transient using the X-ray radiography system. However, the ultrasonic pulse-echo method has sampling intervals of about 0.2 ms, and was used to determine the instantaneous regression rate over the entire test from ignition to motor shut down.

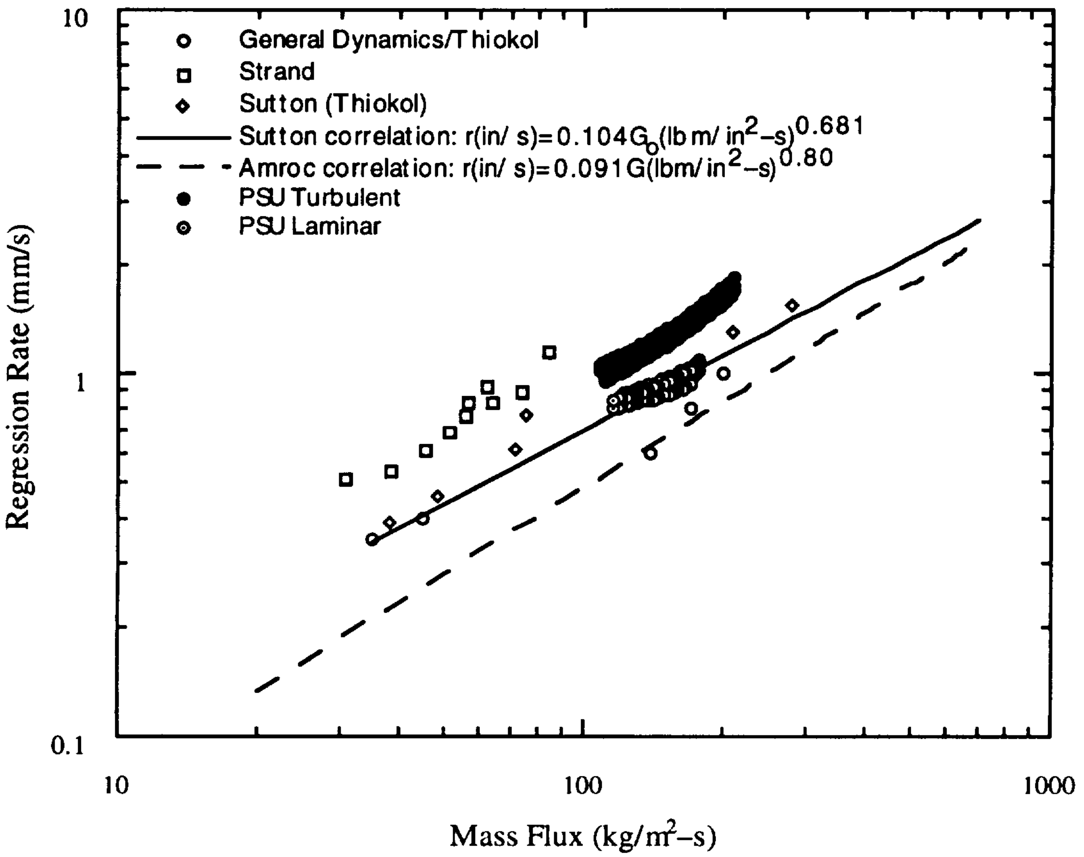

Figure I.4.14 Comparison of several regression rate studies

Figure I.4.14 shows a comparison of the regression rate data obtained in this study with data obtained by other researchers. The Penn State data is shown as two separate groups: regression rate in the laminar region of the boundary layer and regression rate in the turbulent portion of the boundary layer. Not surprisingly, the turbulent regression rate data is higher than the laminar regression data at the same mass flux. The Penn State data matches quite well with both the data presented by Strand and by Sutton, which comes from Thiokol experiments. The Amroc correlation and General Dynamics data, however, seems somewhat lower than the other data sets, which may be due to the low pressures (88 psi) used in some of these tests.

I.4.6: Effects of Solid Fuel Additives

In order to determine the effects of solid-fuel additives on the combustion behavior of HTPB and GOX, two different types of powders were added to the solid fuel: carbon black and ultra-fine aluminum (UFAL). In all tests conducted with these additives, one fuel slab contained the additive at a certain weight percent, while the other fuel slab contained 0% additive (pure HTPB). In this manner, a direct comparison in the behavior of the two slabs was possible. In no cases were both carbon black and UFAL added to the same fuel slab.

I 4.6.1: Samples with Carbon Black Powder Additive

Carbon black represents a commonly used solid–fuel opecifier. The addition of carbon black makes the solid fuel opaque, which prevents in–depth radiation absorption. In order to determine the effect of carbon black on solid fuel regression rate and surface temperature, one of the fuel slabs was fabricated with 0.25% by weight carbon black additive during the fuel processing stage for two tests. The results of both tests indicated no significant difference in the regression rates of the slabs with carbon black compared to those of the translucent fuel slabs. For Test No. 9 (initial GOX flux of 210 kg/m^2–s), both slabs had a global regression rate of 1.2 mm/s and displayed very similar time–averaged regression rate profiles. For Test No. 11 (initial GOX flux of 170 kg/m^2–s) both slabs had nearly the same global regression rate of 0.96 mm/s. Again, the time–averaged regression rate profiles with respect to axial location were almost identical within experimental error. Figure I.4.14 illustrates this result, along with the results of Test No. 14, discussed later. It is believed that a black char layer was formed on the surface of the translucent fuel slabs during burning, so that the radiative heat flux was absorbed only at the surface rather than in the interior of the slab. Such a char layer has been observed on the surfaces of all recovered HTPB fuel slabs.

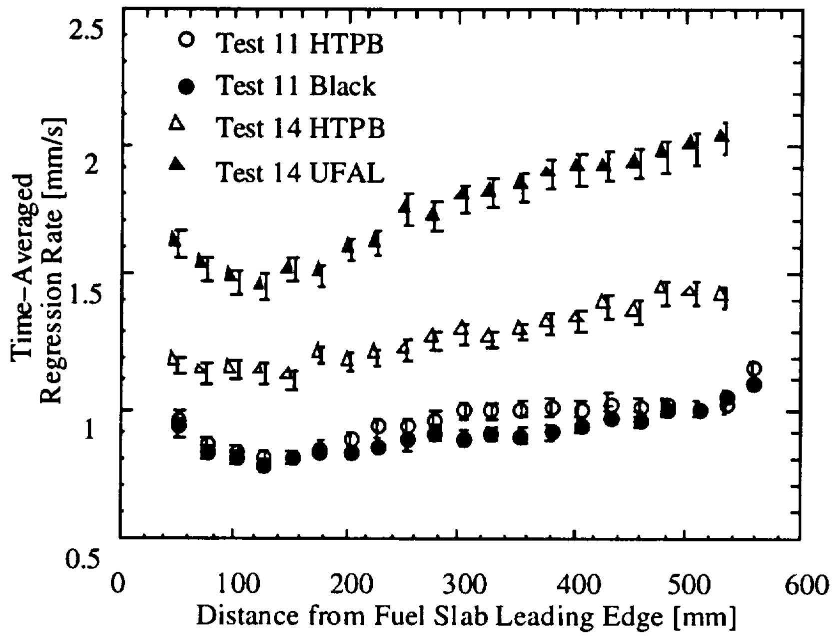

Figure I.4.15 Time–averaged regression rate profiles showing effects of solid fuel additives

From thermocouple measurements, the surface temperature of the slab with carbon black was about 930 K at a location 300 mm downstream from the leading edge of the fuel slab in Test No. 11. This result is consistent with previous surface temperature measurements, which indicate that the surface temperature of pure HTPB fuel slabs is around 950 to 1150 K, depending on operating conditions and axial location [I.32]. The subsurface thermal wave profiles of Test No. 6 (translucent slab) and No. 11 (black slab) were compared since both tests had similar initial GOX mass fluxes (148 and 162 kg/m^2–s, respectively) and global regression rates (0.92 and 0.95 mm/s, respectively). The surface temperatures and subsurface temperature profiles were found to be quite similar, giving further evidence that the addition of carbon black powder did not affect the regression behavior of the HTPB fuel slabs.

I 4.6.2: Samples with Ultra–Fine Aluminum Powder Additive

In order to assess the effects of ultra–fine aluminum powder (UFAL) on the burning rate of HTPB, several tests were conducted using one pure HTPB fuel slab and one HTPB fuel slab loaded with a certain fraction of UFAL. In Tests Nos. 12, 13, and 14, UFAL was added to one fuel slab in amounts of 4%, 12%, and 20% of the total fuel weight, respectively. In contrast to carbon black powder, the UFAL powder had a significant effect on the solid fuel regression rate. Figure I.4.15 shows the time–averaged regression rate profiles of the pure HTPB slab and the HTPB/20%UFAL slab from Test No. 14. Though the two profiles have approximately the same shape, the fuel slab containing 20% UFAL consistently displays a much higher regression rate than the pure HTPB slab at the same axial location.

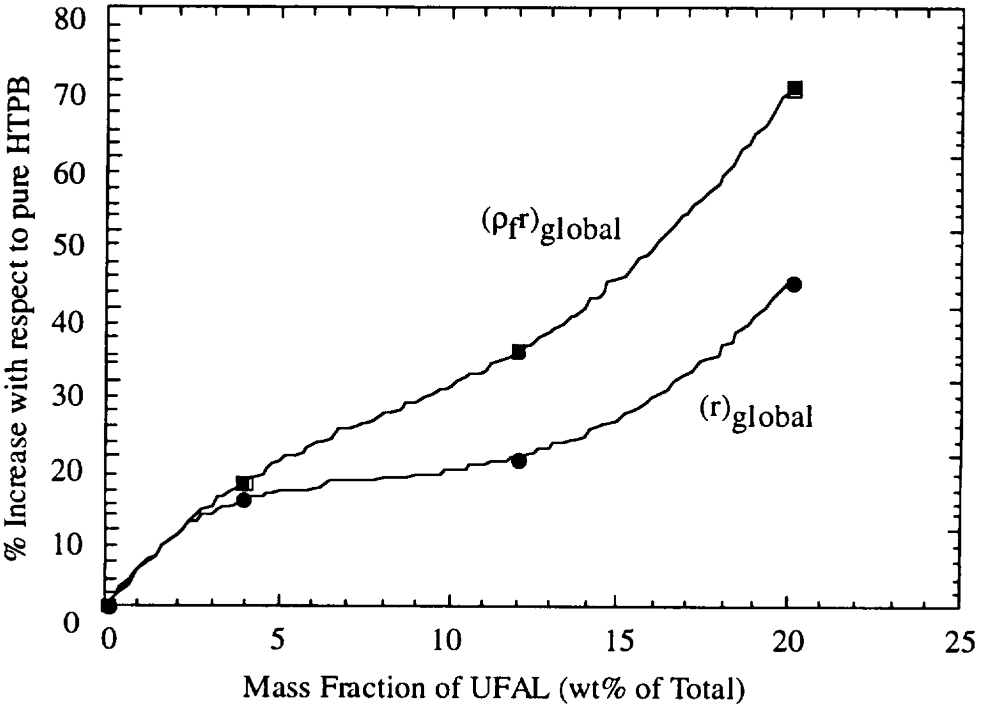

Figure I.4.16 Effect of UFAL addition on global regression rate and solid fuel mass burning rate

Figure I.4.16 shows the increase in global regression rate and global mass burning rate with respect to pure HTPB versus %wt of UFAL in the fuel slab. Since UFAL has a higher density than HTPB, the increase in mass burning rate is even higher than the increase in regression rate for the same percentage of UFAL. Test No. 14 indicates that with 20% UFAL addition, the regression rate increased by almost 40%

and the mass burning rate increased by approximately 70% over the pure HTPB slab. These values represent a significant improvement in performance since low regression rate is often cited as a major disadvantage of hybrid rocket motors.

As discussed previously, the surface of recovered pure HTPB slabs exhibited different characteristics with axial distance: The front portion of the slab had a smooth surface, followed by a middle region of increasingly distinct transverse striations. The transverse striations developed into much more random patterns at distances further downstream. These fuel surface characteristics were attributed to the transition from laminar to turbulent flow in the boundary layer. The fuel slabs containing UFAL exhibited much different surface characteristics than the pure HTPB slabs. Figure I.4.17 shows the fuel slabs from Test No. 13. The slab with 12% UFAL displayed a much smoother surface than the pure HTPB slab. This evidence suggests that some forms of heterogeneous reactions may exist near the surface region, and thereby contribute to the enhanced regression. Based on Ref [I.30], it is believed that when subjected to a large enough heat flux, such as occur in a hybrid rocket motor, UFAL particles vaporize with an associated high heat release. Possibly, the unique UFAL manufacturing process allows the particles to form in a metastable state. When "disturbed" by heating, the particles vaporize and release their stored energy. This energy release causes a greater heat feedback to the fuel surface than that occurs in pure HTPB, and increases the regression rate. It is useful to postulate another mechanism associated with microexplosions to explain the rapid reaction of the aluminum particles near the surface. During manufacturing, the UFAL particles were formed under a rapid cooling process. A shell–like crust may form on the surface of the particles as the outer region cools, inducing a high potential for built–in thermal stresses within the particle as the interior region cools to ambient conditions. When the UFAL particles are subjected to high temperatures near the fuel surface, the outer shell is heated and softened first. The internal material could then be ejected in the form of a microexplosion. Due to these unusual and promising characteristics of UFAL, much more research in this area is required.

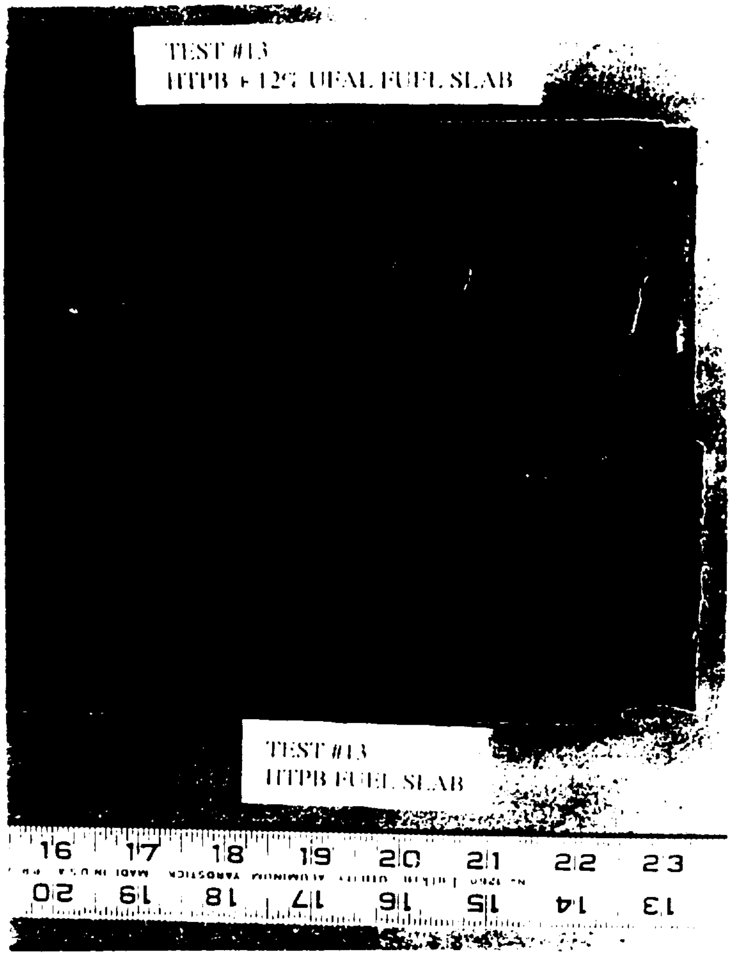

Figure I.4.17 Surface characteristics of pure HTPB and HTPB with 12% UFAL addition

I 4.7: Development of Regression Rate Correlations

This section discusses the results of empirical correlations which relate the instantaneous regression rate obtained from X-ray images and the ultrasonic transducer to flow parameters, such as G_o, G, and Re_x, and P, and geometric parameters such as x, L, and D_h. The correlations presented below have been developed from results similar to those discussed in the previous sections of this chapter.

One of the main objectives of this study was to provide correlations to relate the solid fuel regression rate to motor operating conditions and fuel grain geometry. In order to accomplish this goal, the instantaneous regression rate data provided by the X-ray radiography system was carefully examined to determine the regression rate dependence on axial location, mass flux, pressure, hydraulic diameter, Reynolds number, and fuel formulation (% weight ultra-fine aluminum powder). The effects of carbon black powder and ultra-fine aluminum powder on regression rate have already been discussed in the previous section. The individual influences of flow regime and operating conditions on regression rate are discussed in the following sections to illustrate their importance in the overall regression rate correlations.

I.4.7.1: Regression Rate Dependence on Flow Regime

Figure I.4.18 shows deduced regression rate time histories at several axial locations for a single test. The regression rates are relatively high at the beginning of the test, but decrease continuously with time due to increase in the local port area and corresponding decrease in the local mass flux, which, for convectively governed solid fuel regression, is the most influential operating condition. Since local mass flux increases in the downstream direction due to fuel mass addition, the regression rates also tend to increase with axial location measured from the fuel slab leading edge, as indicated in this figure.

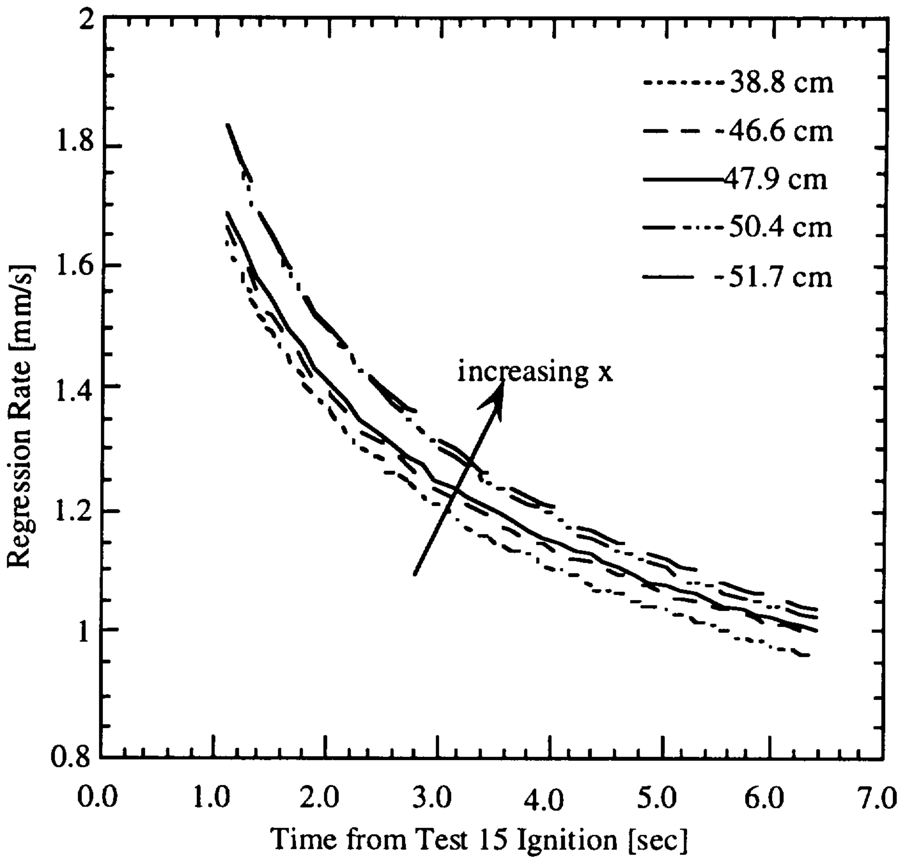

Figure I.4.18 Representative regression rate time histories

However, as shown by Marxman and Gilbert, a location of minimum regression rate could exist somewhere on the fuel slab. For optimal fuel grain design, the prediction of this location may be important. Figure I.4.19 illustrates the solid fuel internal ballistic behavior observed in this study. The lower portion of the graph shows several instantaneous regression rate profiles from Test 13, with a lower initial GOX mass flux, and from Test 15, with a higher initial GOX mass flux. For Test 13, the X-ray and image intensifier were set up to view the upstream portion of the fuel slabs, while for Test 15, the X-ray images were taken from the downstream region of the fuel slabs. The break between the two sets of regression rate profiles is due to obstruction by metal support pieces between the two viewing windows and to selection of the particular viewing area for each test.

In Figure I.4.19, the regression rate profiles are 0.5 sec apart for Test 13 and 0.4 sec apart for Test 15. The regression rates were higher for Test 15 due to higher injected GOX mass flux and the downstream turbulent sampling location. The regression rate is relatively high near the leading edge of the fuel slabs, but decreases with axial location for a certain interval until reaching a minimum, beyond which the regression rate increases with increasing axial distance from the leading edge. This point of minimum regression rate corresponds to the crossover of two competing effects: Reynolds number and local mass flux. The regression rate should decrease with Reynolds number (Re_x) but increase with mass flux, which both increase with axial location, x. Near the fuel slab leading edge, the Reynolds number effect is dominant, but further downstream, the effect of mass flux becomes more important. In addition, the location of the minimum regression rate, $x_{r_{min}}$, moves downstream with time, as indicated by the line passing through the profiles in the upstream region. It is believed that since the regression rate is more sensitive to mass flux than to Re_x, as time increases, the decrease of mass flux tends to favor the Re_x effect, thus causing the location of minimum regression to move downstream with time. For Test 13, $x_{r_{min}}$ moved about 0.05 x/L (30.5 mm) downstream during the test. The regression rates also vary with position in the downstream region, but generally tend to increase in the downtream direction due to mass injection by fuel pyrolysis. The non-uniform regression behavior of the fuel slabs in the downstream region could be caused by the embedded thermocouple extension wires and by surface roughness effects.

The upper portion of Fig. I.4.19 shows the variation of the power n on G (i.e., $r \sim aG^n$) with time-averaged axial Reynolds number (as measured from the fuel slab leading edge), which has a one-to-one correspondance with the x/L axis. For example, at x/L=0.2, the value of Re_x is 250,000, so Re_x is given on the top horizontal scale.. The deduced value of n, obtained by curve fitting r with G at various axial locations, indicates the boundary layer flow regime (e.g., laminar versus turbulent).. In the downstream region (Test 15 data) the particular n at individual axial locations varied slightly, but never departed significantly from the fully turbulent value of 0.8. In the upstream entrance flow region, however, n shows a much greater dependence on Re_x and x/L. Near the slab leading edge for x/L between 0.125 and 0.15, the deduced instantaneous regression rates were found to be independent of G (i.e., n=0). It is believed that a recirculation zone near the fuel slab leading edge may cause this behavior. Downstream of this n=0 region, the value of n increases approximately linearly until reaching the laminar region. Here, n assumes values of about 0.5 or 0.6 (the values for Test 13 were slightly higher than the nominal values for the laminar region). This laminar region corresponds to Reynolds numbers of about 300,000 450,000. The middle third of the fuel slabs and combustor port ($0.3 \le x/L \le 0.6$) has not yet been observed with the X-ray radiography system, but it is believed that a region of transitional flow between laminar and turbulent exists downstream of the laminar region at Reynolds numbers slightly greater than about 450,000.

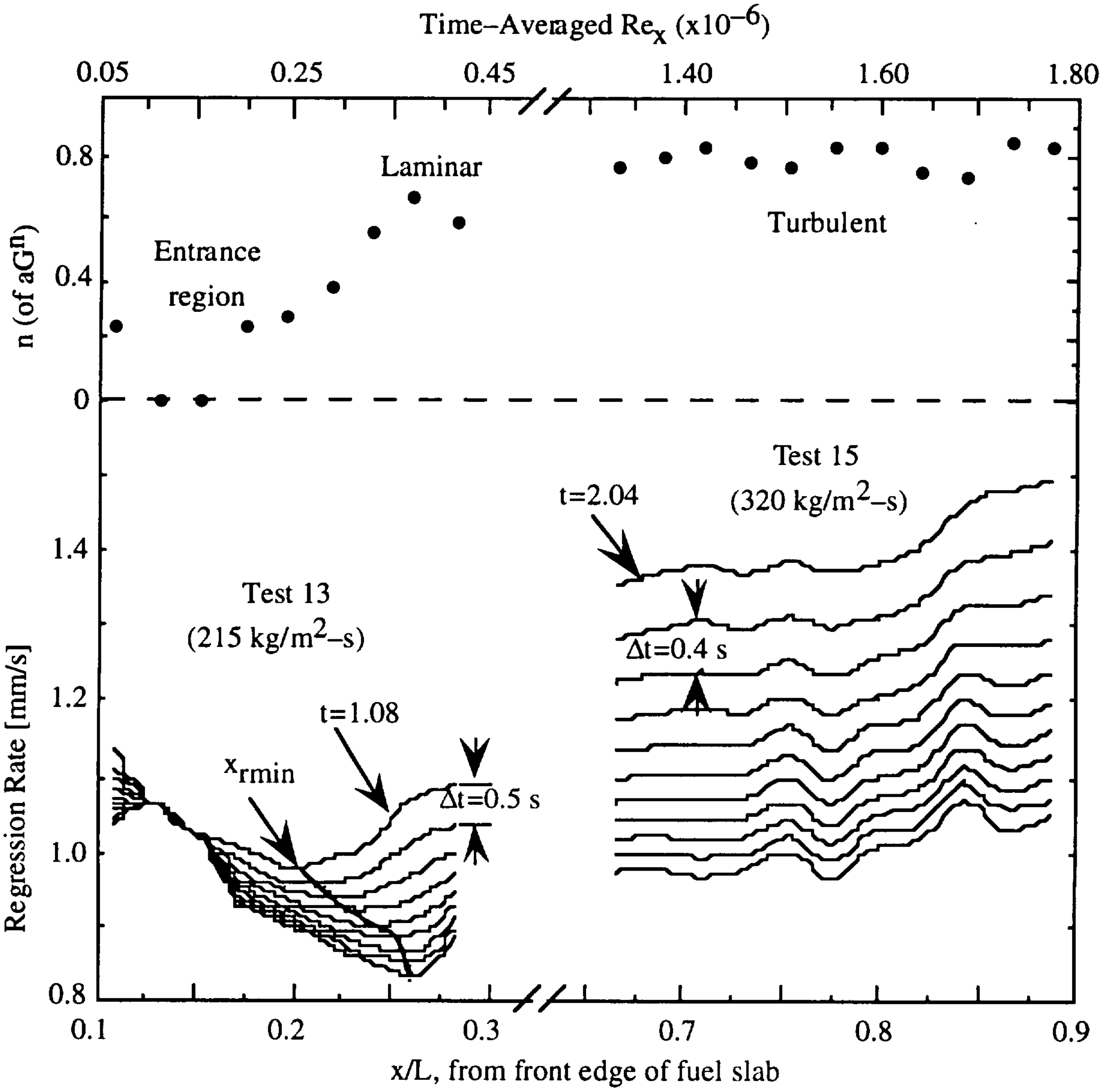

Figure I.4.19 Internal ballistic behavior

The results shown in Fig. I.4.19 were qualitatively similar to the results of other tests conducted during this study. For the design of optimal grains with minimal slivers, the regression rate behavior in the three regions identified above should be considered since, in addition to the turbulent regime, the entrance and laminar flow regimes must also exist in full–scale motors.

I 4.7.2: Regression Rate Dependence on Operating Conditions

Examining the relationship between regression rate and mass flux shows regimes where the convectively-controlled regression rate may be influenced by either gas-phase radiation or kinetics. Figure I.4.20 shows a plot of regression rate versus oxidizer mass flux for two different tests at similar axial locations. The regression data for both tests begins to diverge from the convective solution when the mass flux drops below about 140 kg/m^2-s (0.2 lb$_m$/in^2-s). In the lower mass flux regime, the regression data is higher than that predicted by the convective law due to the radiation heat flux to the solid fuel surface. In addition, the influence of radiation on regression rate is more pronounced at higher pressures. The Test 15 data shows higher regression rates in the lower mass flux regime than the data from Test 17, which was conducted at the same mass flux but at a lower pressure level. The effect of radiation is not as evident at higher mass fluxes because of the complex interaction of fuel mass blowing, convective heat flux, and radiative heat flux to the fuel surface, but becomes apparent in the low mass flux regime where convection is less dominant. This evidence suggests that some type of radiative model should be included in regression rate correlations. The increase in regression rate due to radiation in the low mass flux regime has also been suggested by several other researchers, such as Strand [I.7], Altman [I.20], and Muzzy [I.12]. The effect of finite rate gas-phase kinetics, which should act to reduce the regression rate at very high mass fluxes [I.12, I.20], has not yet been observed in this investigation

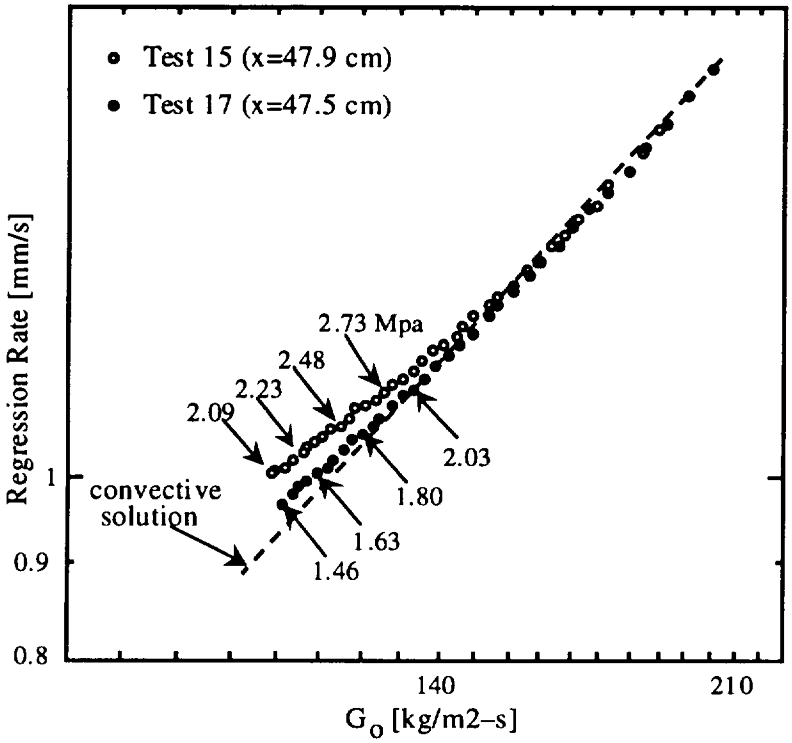

Figure I.4.20 Effect of radiation on regression rate

I.4.7.3: Derivation of Proper Empirical Correlational Form

One of the major goals of this study was to develop empirical correlations which relate the solid fuel regression rate to operating conditions and geometry of the motor. Accurate estimation of solid–fuel regression rate is needed for motor design, performance prediction, and high percentage of fuel utilization.

Once the instantaneous regression rate has been deduced at known operating conditions, the data can be correlated with other instantaneous governing parameters such as G (or G_o), P, and D_h to determine their functional relationships. In order to correlate experimental data over a broad range of oxidizer flux levels, the effect of gas–phase radiation on regression rate must be considered, as discussed in the above section. The radiative energy flux, though normally assumed a small fraction of the total energy feedback to the solid fuel, could be especially important at low oxidizer mass fluxes, as discussed above.

In order to account for this effect, a proper correlational form was sought. To correct for radiative effects, Marxman et al [I.13] suggested the following equation:

$$\rho_f r = [Q_c \exp(-Q_r/Q_c) + Q_r]/\Delta H \qquad (I.4.5)$$

Expressions for Q_c and Q_r are known:

$$Q_c = aGRe_x^n B^{0.23} \Delta H \tag{I.4.6}$$

$$Q_r = \sigma T_g^4 (1 - e^{-\alpha PD}) \tag{I.4.7}$$

where Eq. (I.4.6) is taken from Marxman et al. [I.13] and Eq. (I.4.7) appears in Refs [I.7 and I.20]. In Eq. (I.4.6), n should theoretically equal –0.5 for laminar flow and –0.2 for turbulent flow.

Substituing Eq. (I.4.6) and (I.4.7) into Eq. (I.4.5) gives

$$\begin{aligned} \rho_f r/G_o = {} & a_1 Re_x^{n-1} (x/L)_{m-n+1} \{a_2 (1 - e^{-\kappa Ph})/(G_o Re_x^{n-1}) \\ & + \exp[-a_2 (1 - e^{-\kappa Ph})/(G_o Re_x^{n-1})]\} \end{aligned} \tag{I.4.8}$$

By substituing $Re_x = Gx/\mu$ into Eq. (I.4.8) and rearranging, a dimensional form results:

$$r = c_1 G_o^n x^m \{c_2 (1 - e^{-\kappa Ph})/G_o^n x^{n-1} + \exp[-c_2 (1 - e^{-\kappa Ph})/G_o^n x^{n-1}]\} \tag{I.4.9}$$

The first term on the right side of Eq. (I.4.9) represents the portion of regression due to convective heat flux from the gas phase to the solid–fuel surface, while the term in curly brackets represents the corrective term due to radiative heat flux to the surface. Eq. (I.4.9) appears to properly represent the trends shown in Figure I.2.1 for the regimes controlled by both convective and radiative heat transfer to the solid fuel surface. In the middle region of Figure I.2.1, the regression rate is dominated by convection. The term outside the curly brackets of Eq. (I.4.9) should be large in this region since it is proportional to G, while the term in curly brackets should be small since it varies inversely with G. Conversely, in the left region of Fig. I.2.1, the second term becomes important since G is relatively small, while the first term contributes less to the overall heat flux. In this region, the radiative contribution to regression is relatively more important as G (or G_o) decreases and as the product of pressure and port height increases. When Pxh is large, the effective emissivity term in curly brackets of Eq. (I.4.9) is high and hence the radiative transfer is more important.

In Eq. (I.4.9), r is given in (mm/s), G_o in (kg/m^2–s), p in (Mpa), x in (m), and h in (m). When κph is zero, there is no thermal radiation from the gas phase and the term in curly brackets becomes unity. In the process of correlation development, the data were compared to $C_1 G_o^n x^m$ alone, which was found to be inadequate to account for the regression rate values at the lower GOX mass fluxes. Therefore, the more complicated form of Eq. (I.4.9) was necessary to correlate the data.

I.4.7.4: Correlation Results

The parameters C_1, C_2, m, n, and k were found using a least squares analysis to minimize error. Figure I.4.21 shows the experimental regression rate versus the predicted regression rate found using Eq. (I.4.9).

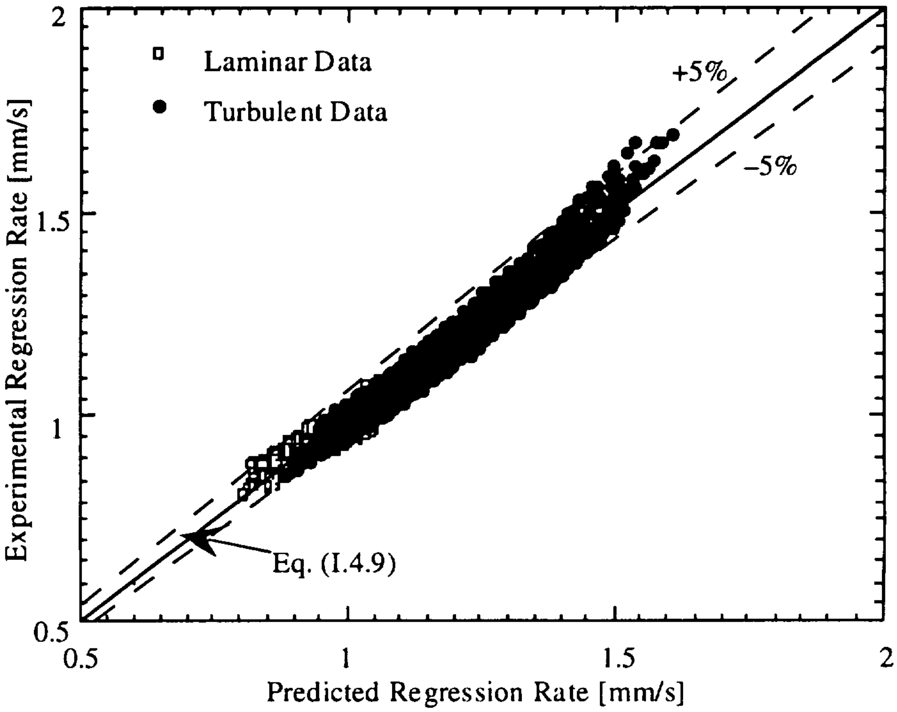

Figure I.4.21 Regression rate correlation for pure HTPB

Almost all the data lies within a ±5% error band, indicating that the correlation properly represents the important physical processes governing solid fuel regression. However, it should be noted that the data shown in Fig. I.4.21 represents two different correlations: one for the laminar flow regime and one for the turbulent flow regime. The parameters have different values in these two regimes as shown in Table I.4.2.

Table I.4.2 Parameters for correlations

Parameter	HTPB Laminar	HTPB Turbulent	HTPB +4%UFAL	HTPB +12%UFAL
c_1	0.1165	0.0158	0.0535	0.2538
c_2	6.632	84.389	14.197	14.197
n	0.50	0.90	0.63	0.63
m	0.313	0.344	0.122	0.882
k	17.13	17.13	57.11	57.11

The value for n in the turbulent regime is slightly higher than the theoretical value of 0.8. Since G_o has been used here instead of the local flux, G, this difference is expected. However, the 0.5 power is also expected since the laminar region exists near the head end where G_o is quite close to G. According to convective theory, the regression rate should depend on axial position, x, to the –0.2 power in the turbulent regime and –0.5 in the laminar regime. Here, an overall positive power on x was found for both regimes. Since G_o has been used here instead of G, the positive power on x probably accounts for the increase in regression rate due to mass accumulation in the downstream direction.

Figure I.4.22 shows the contribution of both convection and radiation to the regression rate versus oxidizer mass flux for Test No. 15. At higher mass fluxes, the radiative contribution accounts for about 6 or 7% of the total regression, but as mass flux decreases, the radiation becomes more important, eventually providing over 12% of the overall regression rate. At higher pressures, the radiative contribution should be even more prominent in the lower mass flux regime. The percentage of regression rate due to convection was evaluated as the ratio of $C_1 G_o^n x^m$ to the left hand side of Eq. (I.4.9), the total regression rate. The percentage of regression due to radiation is the difference between 100 and the convection portion.

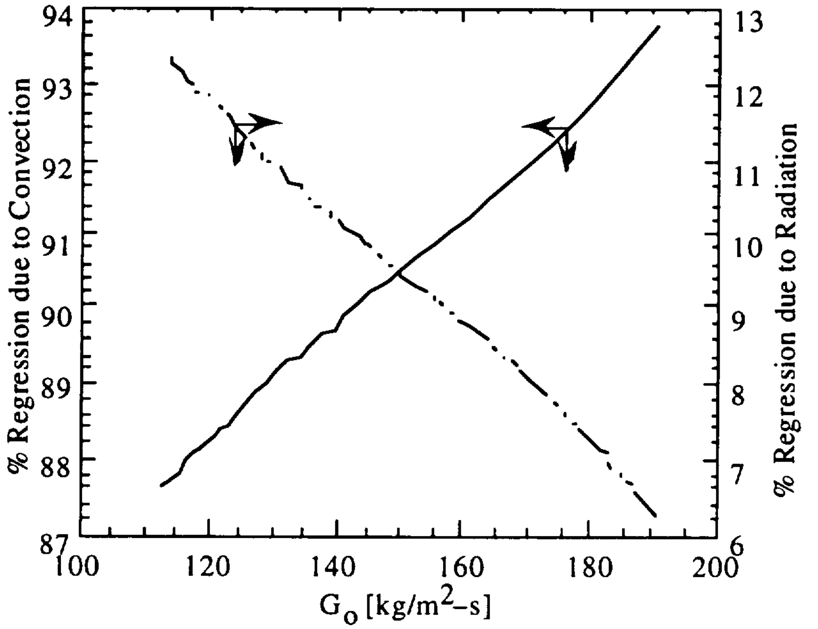

Figure I.4.22 Radiative and convective contributions to regression rate

Separate correlations were developed for HTPB/4% UFAL and HTPB/12% UFAL. The experimental and predicted regression rates are compared for both cases in Figure I.4.23 which indicates that the correlation accurately predicts the experimental regression rates. The parameters for these correlations are also shown in Table I.4.2.

The data for the tests utilizing the above fuel formulations were taken in the upstream region, and therefore correspond the laminar regime, as indicated by the value of n. Similar values were obtained for most of the parameters, but the 12%UFAL fuel formulation showed a much greater dependence on axial location than the 4%UFAL formulation, as shown by the higher m value. Since the 12% UFAL slab had a substantially higher fuel mass flux than the 4% UFAL sample, the boundary layer may have been changing rapidly with axial location due to this destabilizing effect, causing a relatively high dependence on x/L.

The value of k was also higher for the UFAL fuel formulations than for the pure HTPB cases, discussed above. This type of result is expected for metalized fuels which should show a greater dependence on radiation due to higher gas-phase emissivity from vaporized metal particles.

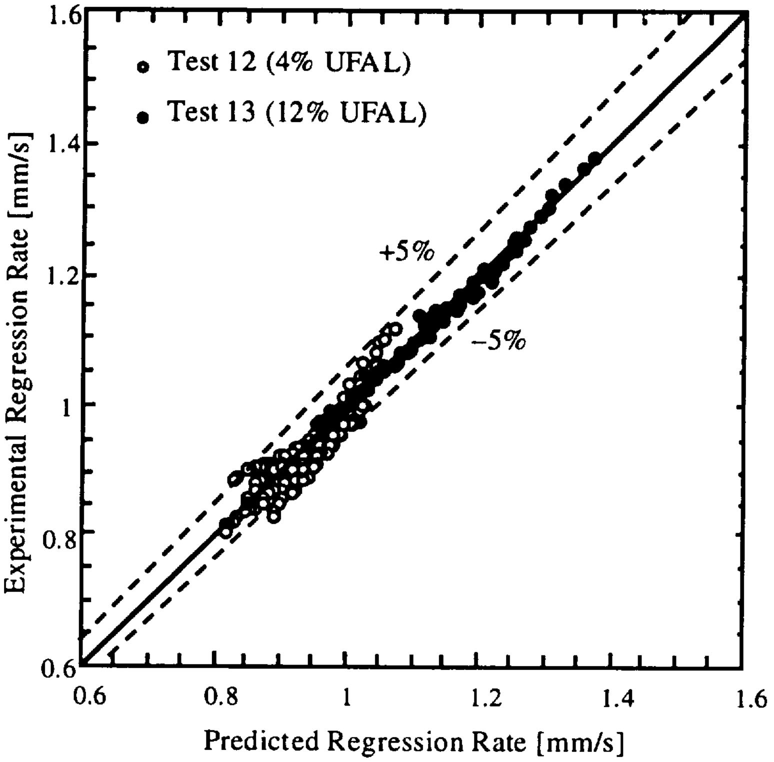

Figure I.4.23 Correlations for UFAL-loaded HTPB

I.4.8: Solid Fuel Pyrolysis Behavior

Table 3 lists the temperature and subsurface heat flux results found in this study, along with operating conditions and time–averaged regression rate. Assuming no chemical reactions in the subsurface region, the conductive heat flux at the fuel surface can calculated from

$$q_{-}'' = \rho_f \, r \, c_p \, (T_s - T_o) \tag{I.4.10}$$

using the measured T_s and r.

Table I.4.3 Deduced burning surface temperature and subsurface conductive heat flux

Go,i	x	r	Ts	q–
133.3	14.0	0.712	970	718
133.3	44.5	1.148	986	1187
102.3	6.4	0.590	932	560
102.3	52.1	1.030	1020	1114
113.5	14.0	1.090	944	1129
162.3	6.4	0.916	1043	1022
162.3	29.2	1.062	937	1016
370	36.8	1.357	1018	1483
370	44.5	1.420	1169	1852
370	*52.1*	*1.256*	*1301*	*1889*

A solid fuel pyrolysis law may be obtained by relating the regression rate to the surface temperature through the Arrenhius equation

$$\rho_f r = A \exp(-E_a / 2 R_u T_s) \tag{I.4.11}$$

According to [I.18] the surface temperature should increase in accordance with the regression rate so as to accelerate solid fuel degradation. Figure I.4.24 compares the results of several studies on an Arrenhius type plot of the solid fuel mass flux ($r_f r$) vs reciprocal surface temperature. In general, the PSU data matches quite well with those found in previous studies and falls within the range of error suggested by Cohen [I.18]. The differences with the law from Lengellé et al. may be due to the different methods used to determine the surface temperature. The pyrolysis data of [I.18] was extrapolated from differential scanning caliorimetry (DSC) experimental data with low heating rates on the order of 0.2 K/s for surface temperature around 700 K to the heating rates for hybrid motor conditions (on the order of 1500 K/s) and surface temperature of about 1000 K. This long extrapolation was recognized by Lengellé.

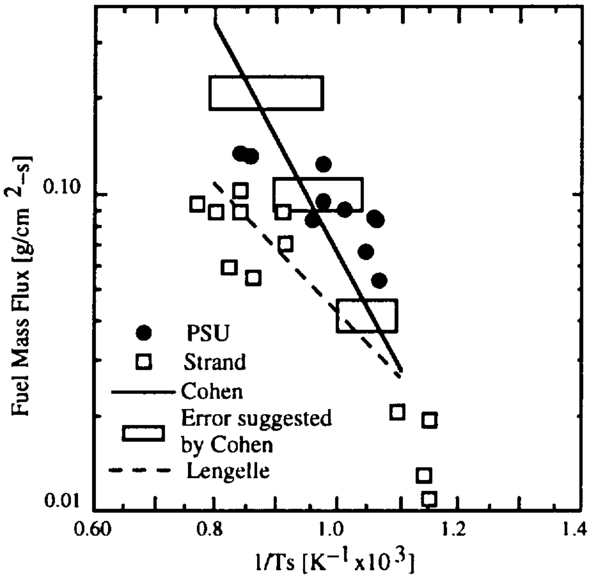

Figure I.4.24 Comparison of several pyrolysis studies

As indicated by Eq. (I.4.11), a least squares fit of ln ($\rho_f r$) vs $1/T_s$ provides an estimate of the activation energy, E_a, for HTPB pyrolysis. The slope of the curve in Fig I.4.25 is –2891 K, which, when multiplied by $2R_u$, gives a value of 11.5 kcal/mol for E_a. This value is quite similar to that of 13.5 kcal/mol given by Brill and Arisawa [I.15,I.16] for the overall activation energy of HTPB under high heating rates. As stated in Refs [I.15,I.16,I.25], relatively low activation energies such as those stated above, indicate that the pyrolysis process is limited by desorption of pyrolyzed fuel molecules from the solid fuel surface, and not by polymer chain bond breaking. The latter process is characterized by higher activation energies on the order of 40 kcal/mol, and dominate the pyrolysis process at low heating rates or low pressures and temperatures. This difference may explain why Lengellé obtains an E_a of 48.6 kcal/mol at low heating rates.

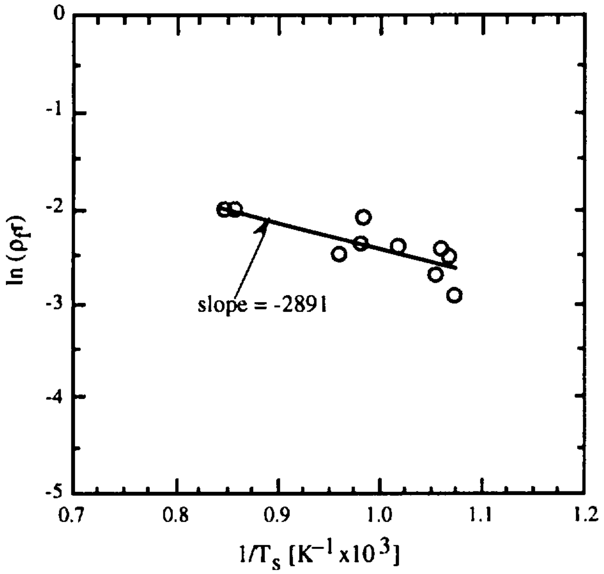

Figure I.4.25 Obtaining HTPB activation energy

I.5 Conclusions

Several conclusions can be drawn from the results of the study:

1. Severe combustion instability phenomena were encountered in early tests. The source of instability was identified as the acoustic coupling between the GOX feed line and the combustion chamber. The instability problem was eliminated by decoupling the two regions. The magnitude of chamber pressure oscillations was reduced to less than ±1.5%.

2. The burning surface temperature of the HTPB varied between 950–1150 K, depending on both operating conditions and axial locations. The burning surface temperature is higher at the turbulent region than that at the laminar region

3. The subsurface temperature profiles are steeper (thinner thermal waves) with higher surface temperatures at the downstream locations; this is due to the increase in heat transfer rates in the turbulent portion of the boundary layer.

4. Regression rate increases with axial distance, except near the leading edge portion of the solid fuel; this is caused by the increase in total mass flux and convective heat flux.

5. Both ultrasound and x–ray results indicate that the regression rate varies substantially with both time and axial location; generally decreasing with time due to port area increase and increasing with axial location from the leading edge due to total mass addition.

6. The addition of carbon black to HTPB fuels did not affect the fuel regression rate, surface temperature, and subsurface thermal wave profile in comparison to the translucent fuel slabs. This implies that the in–depth radiation absorption was not important to the regression rate. Radiation flux was absorbed only at the surface where a black char layer is formed.

7. The recovered fuel samples showed distinct surface structures at different axial regions. The surface covered by a laminar boundary layer is very smooth, indicating the existence of a liquid layer. The transition region showed

transverse striations and the turbulent boundary–layer zone exhibited very rough surface structure with highly random patterns.

8. Mechanical deformation of the solid fuel slabs during the motor pressurization and depressurization stages can influence the deduced instantaneous regression rate in a non–negligible manner. This effect must be accounted for when analyzing instantaneous regression rate data. An accurate correction method has been developed in this investigation to account for mechanical deformation.

9. With the above factor considered, both real–time X–ray radiography and ultrasonic pulse–echo methods showed similar results for both the solid fuel instantaneous web thickness and instantaneous regression rate.

10. Addition of ultra–fine aluminum powder (UFAL) caused a significant increase in the solid fuel regression rate. The solid fuel mass burning rate was increased by up to approximately 70% with the addition of 20% by weight of UFAL (the maximum percentage tested). It is believed that UFAL increases the regression rate by enhancing the heat release at or near the solid fuel surface.

11. Regression rate measurements indicate that gas–phase radiation contributes in a non–negligible amount to regression of solid fuels at low oxidizer mass flux levels (below about 140 kg/m^2–s). The motor pressure plays an important role in this regime; at higher pressures, gas–phase emission is more pronounced.

12. Taking into account the effects of gas–phase radiation, flow regime, and axial location, semi–empirical correlations have been developed to describe the regression rate of both pure HTPB and HTPB fuel with ultra–fine aluminum additives as a function of G_o, P, x, h, L, and Re_x. The measured data were within ±5% of the developed correlations. These variables represent *a priori* known design parameters. It is believed that the correlations presented here can be useful design tools to help predict motor performance and fuel utilization.

13. The pyrolysis behavior of HTPB indicates an activation energy of around 11.5 kcal/mol. This value suggests that at high heating rates and surface temperatures the overall pyrolysis process is governed by desorption of high

molecular weight species from the solid fuel surface, and not by bond breaking and reorganization of the polymer chains.

References

[I.1] Sutton, G. 1992. *Rocket Propulsion Elements: An introduction to the Engineering of Rockets*, Sixth Edition, John Wiley & Sons.

[I.2] Green, L., "Introductory Considerations on Hybrid Rocket Combustion," *Heterogeneous Combustion*, 1963.

[I.3] Altman, D., "Hybrid Rocket Development History," AIAA Paper 91–2515, 1991.

[I.4] Anon., AIAA Hybrid Workshop Report, Washington, D.C., 1995.

[I.5] Boardman, T. A., Carpenter, R. L., Goldberg, B. E., and Shaeffer, C. W., "Development and Testing of 11– and 24–Inch Hybrid Motors Under the Joint Government/Industry IR&D Program," AIAA 93–2552, 1993.

[I.6] Strand, L., Ray, R. L., Anderson F. A., and Cohen, N. S., "Study of Fuels for Hybrid Rockets," JPL New Technology Report NPO–18724, May 1994.

[I.7] Strand, L., Jones, M. D., Ray, R. L., and Cohen, N. S., "Characterization of Hybrid Rocket Internal Heat Flux and HTPB Fuel Pyrolysis," AIAA 94–2876, 1994.

[I.8] Marxman, G. A., and Gilbert, M., "Turbulent Boundary Layer Combustion in the Hybrid Rocket," *Ninth International Symposium on Combustion*, Academic Press, Inc., New York, 1963, p. 371–383.

[I.9] Smoot, L. D., and Price, C. F., "Regression Rates of Nonmetalized Hybrid Fuel Systems," *AIAA Journal*, Vol. 3, No. 8, 1965.

[I.10] Smoot, L. D., and Price, C. F., "Regression Rates of Metalized Hybrid Fuel Systems," *AIAA Journal*, Vol. 4, 1965.

[I.11] Smoot, L. D., and Price, C. F., "Pressure Dependence of Hybrid Fuel Regression Rates," *AIAA Journal*, Vol. 5, No. 1, 1966.

[I.12] Muzzy, R. J., "Applied Hybrid Combustion Theory," AIAA Paper No. 72–1143, 1972.

[I.13] Marxman, G. A., Wooldridge, C. E., and Muzzy, R. J., "Fundamentals of Hybrid Boundary Layer Combustion," *Heterogeneous Combustion, Progress in Astronautics and Aeronautics*, Vol. 15, Academic Press, New York, 1964, p. 485–521.

[I.14] Marxman, G. A., "Combustion in the Turbulent Boundary Layer on a Vaporizing Surface," *Tenth Symposium (International) on Combustion*, p. 1337–1349, The Combustion Institute, 1965.

[I.15] Arisawa, H., and Brill, T. B., "Flash Pyrolysis of Hydroxyl–Terminated Polybutadiene (HTPB) I: Analysis and Implications of the Gaseous Products," unpublished.

[I.16] Arisawa, H., and Brill, T. B., "Flash Pyrolysis of Hydroxyl–Terminated Polybutadiene (HTPB) II: Implications of the Kinetics to Combustion of Organic Polymers," unpublished.

[I.17] Dijkstra, F., and Korting, P., "Ultrasonic Regression Rate Measurement in Solid Fuel Ramjets," AIAA 90–1963, 1990.

[I.18] Lengellé, G, Fourest, B., Godon, J.C., and Guin, C., "Condensed Phase Behavior and Ablation Rate of Fuels for Hybrid Propulsion," AIAA 93–2413, 1993.

[I.19] Peck, M. V., and Houser, T. J., "Research in Hybrid Combustion," *Heterogeneous Combustion*, 559–581, 1963.

[I.20] Estey, P. N., Altman, D., and McFarlane, J. S., "An Evaluation of Scaling Effects for Hybrid Rocket Motors," AIAA Paper No. 91–2517, 1991.

[I.21] Salita, M., "Comparison of Four Boundary Layer Solutions for Fuel Regression Rate in Classical Hybrid Rocket Motors," AIAA Paper 91–2520, 1991.

[I.22] Moutet, A. and Barrere, M., "Contribution a l'Etude de la Combustion dans les Fuse'es a Lithergol ou Hybrides," *Advances in Aeronautical Sciences,* Peragom Press, New York, 1961, pp. 465–495.

[I.23] Incropera, Frank P. and DeWitt, David P., *Fundamentals of Heat and Mass Transfer,* 3rd ed., John Wiley & Sons, New York, 1990.

[I.24] Hottel, H.C. "Radiant–Heat Transmission," in W.H. McAdams, Ed., *Heat Transmission,* 3rd ed., McGraw–Hill, New York, 1954.

[I.25] Ramohalli, K., Yi, J., "Hybrid Revisited," AIAA 90–1962, 1990.

[I.26] Ramohalli, K., Bates, R., Jones, M., Wygle, B., and Yi, J., "Some Recent Results from a Program in Hybrids at the University of Arizona," AIAA 95–2945, 1995.

[I.27] Chen, J. K., and Brill, T. B., "Chemistry and Kinetics of Hydroxyl–terminated Polybutadiene (HTPB) and Diisocyanate–HTPB Polymers during Slow Decomposition and Combustion–like Conditions," *Combustion and Flame* 87: 217–232, 1991.

[I.28] Cauty, F., et. al., 1994. "Determination of Solid Propellant Burning Rate Sensitivity to the Initial Temperature by the Ultrasonic Method", *Non–Intrusive Combustion Diagnostics,* Edited by K. K. Kuo and T. P. Parr, Begell House, Inc., New York.

[I.29] Kuo, K. K. and Parr, T. P., eds., 1994. *Non–Intrusive Combustion Diagnostics,* Begell House, Inc., pp. 365–423.

[I.30] Ivanov, G. V. and Tepper, F., 1996. "'Activated' Aluminum as a Stored Energy Source for Propellants", presented at the Fourth International Symposium on Special Topics in Combustion, Stockholm, Sweden.

[I.31] Anon., Omega Temperature Handbook.

[I.32] Chiaverini, M. J., Harting, G. C., Lu, Y. C., Kuo, K. K., Serin, N., and Johnson, D. K., "Fuel Decomposition and Boundary–Layer Combustion Processes of Hybrid Rocket Motors," AIAA 95–2686, 1995.

[I.33] Anon., Elf Atochem, Brochures on Elf Atochem Polybutadiene Products, 1991.

[I.34] Anon., Dow Chemical, Isonate 143L Product Literature.

PART II: THEORETICAL INVESTIGATION

C. L. Merkle and S. Venkateswaran
Propulsion Engineering Research Center
The Pennsylvania State University
University Park, PA 16802

TABLE OF CONTENTS

Section

LIST OF FIGURES

LIST OF TABLES

II.1 INTRODUCTION

There has been renewed interest in hybrid rocket propulsion in recent years as a candidate for advanced launch vehicle applications. Hybrid motors are attractive because of their potential low cost, ease of fuel handling, reliability, throttling capability, and environmentally friendly emissions characteristics. The design of hybrid motors requires an understanding of the physical phenomena that control the combustion and fluid dynamic processes inside the ports. This, in turn, requires a knowledge of the complex interactions between such wide-ranging physical phenomena as fuel surface pyrolysis, oxidizer atomization and vaporization (in the case of LOX systems), gas-phase combustion and mixing, soot formation and radiation characteristics. Of particular importance in the design of hybrid motors is the fuel surface regression rate and the manner in which it varies with operating conditions. The regression rate determines the overall sizing, mass fluxes and geometric configuration of the hybrid fuel ports. Design issues of current importance include size scale-up from smaller to larger motors and combustion stability. The overall objective of the theoretical analysis portion of this study is the development of a design and analysis tool that will enable addressing these issues.

Both experimental and computational studies are necessary to provide appropriate design guidance for full-sized hybrid motors and to assess related issues such as combustion efficiency and combustion stability. The current computational study is closely coordinated with the companion experimental study presented in Part I of this report. As discussed in Part I, the experimental studies have involved detailed diagnostics of combustion processes in a windowed laboratory-scale hybrid combustor. *In-situ* meaurements of the time-dependent regression rate have been obtained using state-of-the-art X-ray and ultrasound techniques. Previous sub-scale hybrid motor tests [1-6] were primarily directed toward global performance measurements and detailed regression rate data have not been previously available. In addition, in the current experimental study, fuel surface temperature is obtained using thermocouples inserted in the fuel slab. This allows the fuel pyrolysis temperature to be determined. The experimental data are useful for verifying and calibrating the computational model. The numerical model is, in turn, used to extrapolate the information gained from the lab-scale experiments and from the small- and mid-scale tests to full-sized hybrid motors. This study thereby enables us to anticipate the critical issues at these larger scales.

In the hybrid rocket combustion chamber, oxygen flowing over the solid fuel reacts with the pyrolyzed gases on the fuel surface and forms a turbulent diffusion flame. Convective and radiative heat transfer from the flame, in turn, provide the heat of pyrolysis for the thermal decomposition of the solid fuel. It is evident that the rate of fuel surface regression is governed by the interaction between these different processes. In general, the surface regression rate is a function of both the axial position in the grain and the stage in the burn. Theoretical modeling of hybrid combustion requires that these processes are adequately represented.

Classical analyses of hybrid combustion [7] have relied on boundary layer assumptions to determine the heat flux to the fuel surface. This heat flux is then used to characterize the surface regression rate. Typically, the regression rate is given as $r_b = G^n$, where G is the head-end specific flow rate of the oxidizer ($= \dot{m}_{ox}/A_{in}$) and the exponent n is generally between 0.6 and 0.8. The experimental correlation presented in Part I of this study, however, shows that this classical boundary layer expression is too simplistic and additional terms are necessary to account for the variations in the regression rate data. The reason for the limitations of the boundary layer theory is that the fluid dynamics in the hybrid rocket motor do not, in fact, correspond to a classical boundary layer. This is due, in part, to the finite dimensions of the fuel ports, which cause strong local acceleration of the core gases in the combustor while causing the oxidizer concentration in the "freestream" to decrease with distance. In addition, mass addition from the pyrolyzing fuel causes the total specific flow rate to increase with axial distance rather than to remain constant. Further, radiative fluxes from the hot gases and soot particles also contribute significantly to the energy balance on the fuel surface. Finally, since boundary layer theory suggests that the fuel surface regression rate is a function of the head-end specific flow rate, this model suggests that the burning rate is insensitive to size and geometric variations. On the contrary, the computational results in the present report indicate that regression rate is, in fact, quite strongly influenced by these factors. Thus, while boundary layer theory provides a qualitative understanding of trends, it is inadequate to provide the kind of quantitative information needed for combustor design and, particularly, for size scale-up. A more comprehensive Navier-Stokes analysis, including the effects of turbulence, combustion and radiation is therefore required [8-10] and is the approach adopted in the present study.

The present analysis is based upon a comprehensive model, that is comprised of the complete time-dependent Navier-Stokes equations, coupled to auxiliary transport equations and physical submodels. The model includes the effects of finite rate chemistry, turbulence, gas-phase radiation and coupling of the gas-phase to the solid (fuel) phase. The solid/gas-phase coupling is handled by detailed energy and species mass balances at the solid-gas interface. Further, the energy equation is solved within the solid phase in order to account for the temperature gradients in the fuel slab. These conditions enable the determination of the fuel surface regression rate and temperature as a function of the coupled solid- and gas-phase solutions.

The hybrid combustion model is calibrated and validated using the experimental data. The modeling physical phenomena such as radiation and fuel pyrolysis is extremely complicated and are handled in a phenomenological fashion in the present study. The magnitude of the radiative heat fluxes to the fuel surface are determined using the measured regression rate data, while the fuel pyrolysis model is verified using the fuel surface temperature data. With the radiation and pyrolysis models fixed, the experimental data are then used to verify parametric trends predicted by the computational model. Global regression rate data obtained from previous subscale tests are also used to verify computational predictions under various operating conditions.

The computational formulation is capable of performing both steady-state and unsteady analyses, although only steady state results are presented in the current report. Experimental measurements reveal that the hybrid flowfield is quasi-steady since the fuel surface regression rate is much smaller than the convective speed of the flowing gases. Thus, a specific test run is simulated by means of a series of steady-state computations, each a snapshot of the flowfield at a particular instance in time. The time-averaged regression rate data may then be obtained by averaging the computational predictions for several instances in the burn, although, in practice, it was sufficient to use the results for mid-way through the burn. In the present study, the computational model is applied to a variety of parametric studies to assess trends and design issues. Specifically, we assess the effects of going from a planar geometry (necessary for the present experimental set-up) to an axisymmetric configuration (representing the central port of a practical combustor), and the effects of scale-up from the sub-scale configuration used in the experiments to representative full-scale configurations. Our results show that both configuration and size play an important role in the fuel regression characteristics, contrary to boundary layer estimates which suggest that regression rate is only a function of the GOX specific flow rate

(G). These results thus demonstrate that computational studies are a useful complement to experimental testing in the design and analysis of hybrid combustors.

The report is organized as follows. We start by presenting an overview of the computational model including the gas-phase governing equations, the combustion model, the fuel pyrolysis model, the solid/gas-phase interfacial boundary conditions and the radiative transfer model. We then present computational results corresponding to the geometry and test conditions employed in the companion experiments. Detailed verification and calibration of various components of the computational model are carried out using the measurement data. Additional verification is also performed using the data from the experiments of Strand *et al.* [3,4] and lab-scale tests carried out by General Dynamics, Thiokol and Rocketdyne [1,2]. We then apply the computational model to study the effects of size scale-up and geometric configuration, which are important to extend the planar, lab-scale measurements to practical, full-scale geometries.

II.2 COMPUTATIONAL MODEL

II.2.1 Governing Equations

The governing equations are the standard Navier-Stokes equations coupled with additional transport equations for combusting species and the equations for the turbulence kinetic energy and dissipation. The coupled set of equations may be written in the following vector form:

$$\Gamma_p \frac{\partial Q_v}{\partial \tau} + \frac{\partial Q}{\partial t} + \frac{\partial E}{\partial x} + \frac{\partial F}{\partial y} = H + L(Q_v) \tag{2.1}$$

where

$$Q = \begin{pmatrix} \rho \\ \rho u \\ \rho v \\ e \\ \rho k \\ \rho \epsilon \\ \rho Y_i \end{pmatrix} \qquad Q_v = \begin{pmatrix} p_t \\ u \\ v \\ T \\ k \\ \epsilon \\ Y_i \end{pmatrix} \qquad E = \begin{pmatrix} \rho u \\ (\rho u^2 + p_t) \\ \rho uv \\ (e + p_t)u \\ \rho uk \\ \rho u\epsilon \\ \rho uY_i \end{pmatrix} \qquad F = \begin{pmatrix} \rho v \\ \rho uv \\ (\rho v^2 + p_t) \\ (e + p_t)v \\ \rho vk \\ \rho v\epsilon \\ \rho vY_i \end{pmatrix} \tag{2.2}$$

Here, $i = 1, 2, \ldots, N - 1$, where N is the total number of chemical species and $p_t = p + \frac{2}{3}\rho k$.

The viscous terms are written in terms of the viscous flux vector Q_v and is given as:

$$L = \frac{\partial}{\partial x} R_{xx} \frac{\partial}{\partial x} + \frac{\partial}{\partial x} R_{xy} \frac{\partial}{\partial y} + \frac{\partial}{\partial y} R_{yx} \frac{\partial}{\partial x} + \frac{\partial}{\partial y} R_{yy} \frac{\partial}{\partial y} \tag{2.3}$$

The viscous matrices take their standard forms and are not defined here for brevity. They are given in Ref. 17.

The preconditioning matrix Γ_p is:

$$\Gamma_p = \begin{pmatrix} 1/\epsilon_p c_t^2 & 0 & 0 & 0 & 0 & 0 & 0 \\ u/\epsilon_p c_t^2 & \rho & 0 & 0 & 0 & 0 & 0 \\ v/\epsilon_p c_t^2 & 0 & \rho & 0 & 0 & 0 & 0 \\ \frac{\tilde{h}_o}{\epsilon_p c_t^2} - 1 & \rho u & \rho v & \rho C_p & \frac{5}{3}\rho & 0 & \rho(h_j - h_N) \\ k/\epsilon_p c_t^2 & 0 & 0 & 0 & \rho & 0 & 0 \\ \epsilon/\epsilon_p c_t^2 & 0 & 0 & 0 & 0 & \rho & 0 \\ Y_i/\epsilon_p c_t^2 & 0 & 0 & 0 & 0 & 0 & \rho\delta_{ij} \end{pmatrix} \tag{2.4}$$

where ϵ_p is a preconditioning parameter, which is responsible for controlling the convergence rate. c_t is the modified frozen speed of sound and is given by $c_t = \sqrt{\gamma R' T} = \sqrt{\gamma (R + \frac{2}{3}\frac{k}{T}) T}$ and $\tilde{h}_o = h + \frac{u^2+v^2}{2} + \frac{5}{3}k$.

Note that the equations are written in dual-time form, which allows for both steady and unsteady solutions within the same computational framework. The first time-derivative in Eqn. (2.1) is a pseudo-time derivative and is present for both steady and unsteady computation. The second time-derivative is the physical time derivative which is necessary only for time-accurate computations and is not used for steady-state computations. The pseudo-time derivative serves as an iterative device: for steady computations, it marches the solution in pseudo-time until the desired steady solution is reached; similarly, for unsteady computations, it ensures that the proper unsteady equations are identically satisfied at each physical time level. Γ_p is a preconditioning matrix that premultiplies the pseudo-time derivative. It is selected so as to condition the eigenvalues of the system under different physical situations such as low speeds, low Reynolds numbers and/or in the presence of high grid aspect ratios and, thereby, provides efficient solution convergence behaviour. More details on the preconditioning procedure may be obtained from Refs. 17 and 18.

For the hybrid combustion problem, steady solutions are useful in characterizing the fuel surface regression rate, combustion efficiency and size scale-up effects. On the other hand. time-accurate solutions are necessary to analyze the incidence of combustion instability in hybrid rocket motors. Since both steady and unsteady solutions are of interest for hybrid combustion analysis. we maintain complete generality in the overall formulation. The results presented in this report are. however. related to regression rate characterization and size scale-up effects and are. therefore. limited to steady solutions.

The source vector H contains the source terms related to combustion. turbulence and radiation. The combustion source term in the species equations, $\dot{w}_i$, is obtained by summing the species generation contributions from the various elemental reactions. This is written as:

$$\dot{w}_i = M_i \sum_{k=1}^{NR} (\dot{c}_i)_k \tag{2.5}$$

where NR is the total number of reactions. $(\dot{c}_i)_k$ is the rate of production of moles of species i by reaction k,

$$(\dot{c}_i)_k = (\nu_{ik}'' - \nu_{ik}')(k_{fk} \prod_{m=1}^{N} C_m^{\nu_{jm}'} - k_{bk} \prod_{m=1}^{N} C_m^{\nu_{jm}''}) \tag{2.6}$$

where the k^{th} reaction is written as:

$$\sum_{i=1}^{N} \nu_{ik}' M_i \rightleftharpoons \sum_{i=1}^{N} \nu_{ik}'' M_i \tag{2.7}$$

Here. ν_{ik}' and ν_{ik}'' are the stoichiometric coefficients for the i^{th} species, k_{fk} and k_{bk} are the forward and backward reaction rates and M_i is the molecular weight of the i^{th} species. C_i is the molar concentration of the species and is given by $C_i = \frac{\rho Y_i}{M_i}$. The specific kinteics model used in the present work is described later.

The source terms in the k and ϵ transport equation correspond to the standard $k - \epsilon$ model [12] with additional low Reynolds number terms introduced for near-wall effects [13]. These may be written as:

$$H_k = \mu_t \mathcal{S} - \frac{2}{3}\rho k \mathcal{D} - \rho\epsilon - \frac{2\mu k}{n^2} \tag{2.8}$$

$$H_\epsilon = C_1 \mu_t \frac{\epsilon}{k}\mathcal{S} - \frac{2}{3}C_1 \rho\epsilon\mathcal{D} - C_2 f_2 \frac{\rho\epsilon^2}{k} - \frac{2 f_1 \mu\epsilon}{n^2} \tag{2.9}$$

where $\mu_t = C_\mu f_\mu \frac{\rho k^2}{\epsilon}$ and $\mathcal{S}$ and $\mathcal{D}$ are given by:

$$\mathcal{S} = \left[\frac{\partial u_i}{\partial x_j} + \frac{\partial u_j}{\partial x_i} - \frac{2}{3}\delta_{ij}\frac{\partial u_k}{\partial x_k} \right] \frac{\partial u_i}{\partial x_j} \tag{2.10}$$

$$\mathcal{D} = \frac{\partial u_i}{\partial x_i}. \tag{2.11}$$

Standard values are used for the constants in the $k - \epsilon$ model. There are: $C_\mu = 0.09$. $C_1 = 1.35$ and $C_2 = 1.8$.

Finally, the energy equation contains a source term to account for the radiative transfer in the gaseous medium. The modeling of this radiative transfer term is discussed in the following section.

II.2.2 Radiative Transfer Model

The experimental studies reported in Part I as well as previous hybrid tests conducted at JPL [4] indicate that radiation may be a signficant contributor to the energy balance on the fuel surface particularly at low mass fluxes. Measurements of radiative flux in the small-scale tests at JPL [4] indicate that, at low specific flow rates (less than $0.1 lbs/in^2 - s$), radiation may account for as much as 25-30% of the total heat flux on the fuel surface. Estimates of the present study—obtained from correlations derived from the measurement data—indicate a radiative contribution of 10 to 15% for GOX flow rates of about $0.2 lbs/in^2 - s$ and concomitantly lower values for higher flow rates. These studies indicate the need for including a model for radiative transfer for the calculation of the fuel surface regression rate. Moreover, it is necessary to assess the relative importance of radiation in a parametric manner, particularly at higher flow rates and as a sizing issue.

The detailed modeling of radiative properties and radiative transfer in participating media is however extremely difficult. We have, therefore, implemented a simplified radiative transfer model, which represents the radiative contribution phenomenologically. The model provides useful qualitative insight into the importance of radiation under various circumstances. The computational results may then be used to determine whether, and under what circumstances, a more detailed radiation model is warranted.

In the simplified model used in the present research, the gas-phase is treated as a purely emitting medium, an approximation that is appropriate in the limit of optically thin media.

$$Q_{\text{rad}} = \sum_{i,j} \frac{4\sigma k_{ij} T_{ij}^4}{J_{ij}} \mathcal{F}_{ij\to k} \tag{2.12}$$

where $1/J_{ij}$ is the volume of the (i,j)th cell and $\mathcal{F}_{ij\to k}$ is the view-factor of that cell with respect to the kth grid location on the fuel slab surface. Summing up the contributions from all the cells in the computational domain yields the total radiative flux incident on a given axial location on the fuel surface. This in turn is employed in the interfacial energy balance (discussed in Section 2.4) used to determine the fuel surface regression rate.

The absorption co-efficient of the gas is taken to be independent of temperature and of the wavelength of the radiation. Its magnitude is determined by calibratng the results with the regression rate data from the subscale tests reported in Part I of this study. At low flow rates, when the radiative contribution is significant, the surface regression rate is under-predicted if the radiative contribution is not accounted for. The gas absorption co-efficient is calibrated so that the desired level of radiation heat flux is obtained at the fuel surface and the predicted regression rate is in agreement with the measured data.

To further understand the qualitative effects of radiation transfer from the gas to the fuel surface, we have also considered the other extreme case of optically thick media. In this optically thick limit, it is possible to represent the radiative flux using the diffusion approximation [11, 12]:

$$Q_{\text{rad,thick}} = -\lambda_R \frac{\partial T}{\partial y} \tag{2.13}$$

where $\lambda_R = 4/3\pi\frac{C}{k}T^3$. In practice, it is likely that the gas is optically thick over some regions of the flowfield (as in very 'sooty' regions of the flame), while it is optically thin in others. By considering the radiative effects in these two limiting situations independently, we can assess the overall trends in the radiative fluxes and determine their relative influences on fuel surface regression rates. The analysis then may be used to determine under what conditions radiation plays a major role in the energy budget and, consequently, whether it is necessary to employ a more detailed radiation model.

II.2.3 Pyrolysis Model

The pyrolysis of the solid fuel (HTPB in this work) into gaseous products is modeled in semi-empirical fashion. Following the work of Cohen *et al.* [15] and Brill *et al.* [16], the rate of pyrolysis is described by means of an Arrhenius-type relationship,

$$\rho_s r_b = A_s \exp\left(\frac{-E_a}{R_u T_s} \right) \tag{2.14}$$

where T_s represents the fuel surface temperature, E_a is the activation energy and A_s is the reaction constant. The above equations have two unknowns, the regression rate and the surface temperature and, thus, requires an additional condition. This is provided by using an interfacial energy balance on the fuel surface as discussed in the following section. In the present work, we use the models of both Brill and Cohen as given in Table II.2.1. Most of the computational results are based upon Brill's results which is the more recent work. However, to show sensitivity of the results to changes in the surface regression model, we also present some calculations based on the Cohen model.

II.2.4 Solid/Gas-Phase Interface Formulation

The coupling between the solid (fuel) and gaseous phases is effected through an interfacial boundary condition. The energy balance at the solid/gas interface involves a balance between the convective, diffusive and radiative fluxes on the gas-side and the diffusive and heat of pyrolysis on the solid-side and is, thus, given by:

$$-\lambda \frac{\partial T}{\partial y} + Q_{rad} + \rho v h - \sum_{i=1}^{N} \rho \mathcal{D}_{im} \frac{\partial Y_i}{\partial y} h_i = -\lambda_s \left(\frac{\partial T}{\partial y} \right)_s - \rho_s r_b h_s \tag{2.15}$$

where the left side of this equation represents the gas-phase quantities and the right side represents the solid-phase quantities. The first term on the left is the convective heat flux to the wall, while the second term is the total radiative flux. The convective heat flux is obtained from the gas-phase solution, while the radiative flux is modelled as discussed in the previous section.

The two relations are augmented by a closed form solution for locally one-dimensional thermal conduction in the solid:

$$T(y) = T_\infty + (T_s - T_\infty) e^{-r_b/\nu_{ts} y} \tag{2.16}$$

where T_∞ is the temperature of the unheated fuel, ν_{ts} is the thermal diffusivity of the fuel slab and r_b is the fuel surface regression rate. The derivative of Eqn. (2.16) may

Model	A_s	E_a
Cohen	2.99e3	-8.557e3
Brill	2.208e3	-6.797e3

Table II.2.1 Arrhenius Expressions for HTPB Pyrolysis be substituted into Eqn. (2.15) to determine the conduction heat loss in the solid phase. Thus, by combining Eqns. (2.14), (2.15) and (2.16), both the fuel surface temperature T_s and the surface regression rate r_b may be determined.

Finally, the wall blowing rate is given by applying a mass balance at the interface:

$$\rho v = -\rho_s r_b \tag{2.17}$$

For the gas-phase boundary condition, the above set of relations is augmented by the standard no-slip axial velocity, the normal momentum equation (for the interface pressure) and the appropriate species balances (for the species mass fractions Y_i).

II.2.5 Gas-Phase Chemistry Model

The computational model has the capability of including complex chemical kinetics to represent the gas-phase combustion processes. However, detailed chemistry for butadiene (the main product of HTPB pyrolysis) is extremely complicated involving over fifty species and hundreds of elementary reaction steps. In the present study we, therefore, use a global combustion model [11] to represent the combustion of the gaseous products of HTPB pyrolysis. The pyrolysis products are taken to be constituted entirely of 1,3-butadiene (C_4H_6). The global model involves two reaction steps. The first step represents the oxidation of C_4H_6, while the second step represents the oxidation of wet CO:

$$C4H6 + 3.5O2 \longrightarrow 4CO + 3H2O$$

$$CO + 0.5O2 \longleftrightarrow CO2 \tag{2.18}$$

As noted above the second reaction can proceed in both directions. The rates of production and destruction of species are given by the following expressions:

$$\dot{w}_{C_4H_6} = -M_{C_4H_6} k_{f1} [C_4H_6][O_2]$$

$$\dot{w}_{O_2} = M_{O_2} \Big[-3.5 k_{f1} [C_4H_6][O_2] - 0.5 (k_{f2} [CO][O_2]^{0.5} - k_{b2}[CO_2]) \Big]$$

$$\dot{w}_{CO} = M_{CO} \Big[4 k_{f1} [C_4H_6][O_2] - (k_{f2} [CO][O_2]^{0.5} - k_{b2}[CO_2]) \Big]$$

$$\dot{w}_{H_2O} = 3 M_{H_2O} k_{f1} [C_4H_6][O_2]$$

$$\dot{w}_{CO_2} = M_{CO_2}(k_{f2}[CO][O_2]^{0.5} - k_{b2}[CO_2]) \tag{2.19}$$

The reaction rates k_f and k_b for the two reactions are expressed as Arrhenius functions and are evaluated from Ref. 16. The values of the Arrhenius constants used in this study are tabulated in Table II.2.2.

II.3 COMPUTATIONS OF EXPERIMENTAL CONFIGURATION

II.3.1 Representative Hybrid Flowfield Simulations

We start by presenting computational solutions of the experimental slab burner configuration. Figure II.3.1 shows the grid geometry for a representative case at three different times in the burn. In each case, the grid size is 151 × 61. The length of the HTPB fuel slabs corresponds to the experimental configuration and is about 23 in (or 580 mm). The initial port height (i.e.. the distance between the fuel slabs) is 0.5 in (or 12 mm). The flowfield in the hybrid combustor is therefore a domain of very high aspect ratio. In the grid plots, the y-coordinate has been exaggerated by a factor of ten so that the details of the grid are visible. The fuel slabs are located in the straight section upstream of the converging-diverging nozzle. The grid is strongly stretched in the near-wall region to resolve the turbulent boundary layer adjacent to the fuel surface. The axial clustering of grid cells signifies the leading edge of the fuel slab. In the computations, the details of the leading edge and trailing edge regions of the fuel slab have been omitted since the main purpose of the present study is the characterization of the fuel surface regression rate. Further, in many of the calculations, the computational domain included only the straight channel section of the configuration. These simplifications of the geometrical details allow relatively modest grid sizes to be used, thereby making it economical to perform a large number of parametric computations.

We first present results for a representative test case (corresponds to Test 11 of the experimental studies). The computations were run at a constant GOX mass flow rate which. for this test. was set at 0.16 kg/s. The specific flow rate G ($= \dot{m}_{GOX}/A_p$), however. decreases with burn time as a consequence of the surface regression and the corresponding increase in port area (A_p). Computational results are shown at three times during the burn: near the start of the burn where the port height was 16 mm corresponding to a

Reaction	A_f	E_f	A_b	E_b
1	1.3496e10	-1.5108e4	0	0
2	2.2387e12	-2.0143e4	5.e8	-2.0143e4

Table II.2.2 Two Step Global Chemistry Model

Start of Burn

Midway in Burn

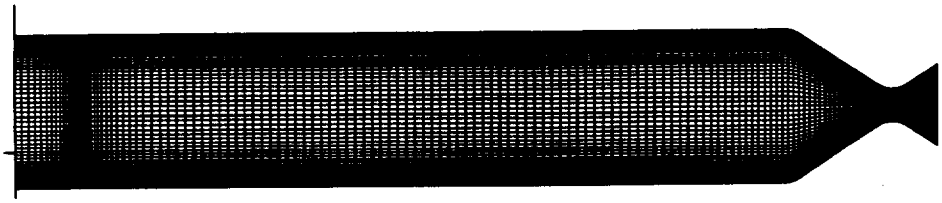

End of Burn

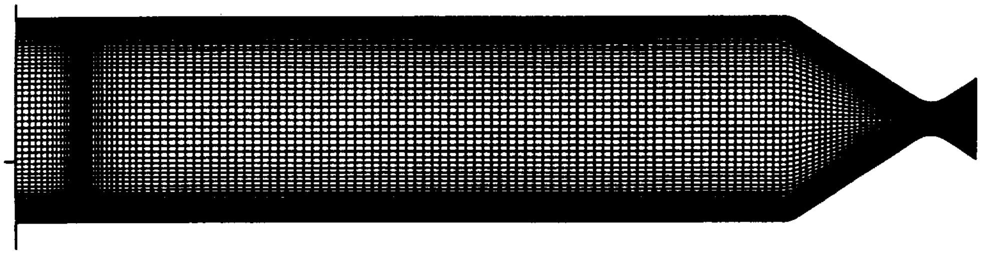

Figure II.3.1 Grid geometry used in the computations at three different times in the burn. Grid size is 151 X 61.

Fig. 3.1

specific flow rate. $G = 165kg/m^2 - s$; midway through the burn at a port dimension of 20 mm corresponding to $G = 132kg/m^2 - s$; and near the end of the burn when the passage height was 26 mm resulting in an oxidizer flow rate of $G = 102kg/m^2 - s$. For modeling purposes. the flowfield is assumed to be quasi-steady at each stage in the burn. and a separate computation is performed for each stage in the burn.The quasi-steady assumption is justifiable since the fuel surface regression rate (typically about 1 mm/s) is extremely small compared to the axial velocity in the port (1-100 m/s depending on the operating conditions).

The fuel surface regression rates at the three times in the burn are shown on Fig. II.3.2. The predictions indicate that the regression rate is highest during the start of the burn where G is highest and drops signficantly as the test proceeds. Its nominal magnitude ranges from 0.5 and 1.5 mm/s. The decrease in surface regression rate with time in the burn is related to the decrease in the magnitude of the specific flow rate G in qualitative agreement with boundary layer theory that relates the regression rate to G^n.

The results in Fig. II.3.2 also show that the regression rate varies with axial location for all three surface positions. The large values of surface regression at the leading edge of the fuel slab is due to the singularity in the heat flux computation at this point. Beyond the leading edge, the regression rate is observed to decrease gradually, reach a minimum and then increase more or less monotonically. At all three times of burn, the regression rate at the back end is faster than that at the front end. The increase in the regression rate with axial location is related to the mass addition effect of the pyrolyzing fuel. which results in an increase in the 'total' specific flow rate as we move downstream. This result is again in qualitative agreement with boundary layer theory when the dependency of the regression rate on the specific flow rate is expressed in terms of the total local specfic flow rate.

Flowfield contours for the computations near the start, midway and end of the burn of Test 11 (reported in Part I) are given in Figs. II.3.3-II.3.6. Figure II.3.3 shows the temperature contours at the three stages in the burn. Under all three situations. the temperature contours in the vicinity of the flame are similar with a peak temperature of about 3500 K. In accordance with the regression rate results in Fig. II.3.2. The temperature contours reveal that the combustion is most efficient at the start of the burn. when the rate of fuel surface regression is highest. As the burn progresses. the regression rate decreases as does the combustion efficiency. Thus. near the start of the burn. the flame extends

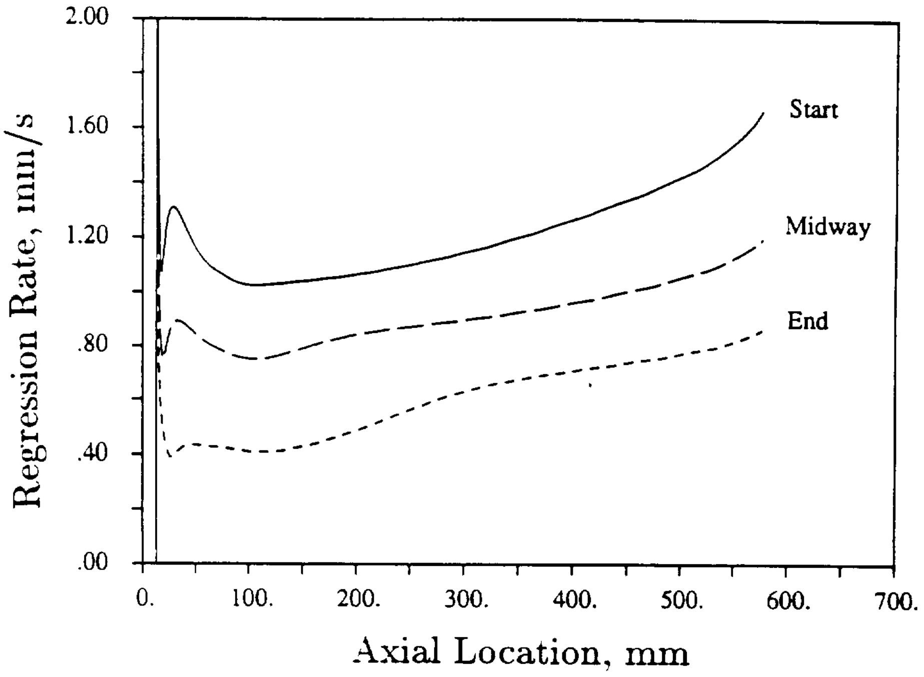

Figure II.3.2 HTPB surface regression rate along the axial length of the fuel slab computed at three stages in the burn. GOX Flow rate = $0.16 kg/s$, $G = 165 kg/m^2 - s$ ($0.23 lbs/in^2 - s$), P=45 atm.

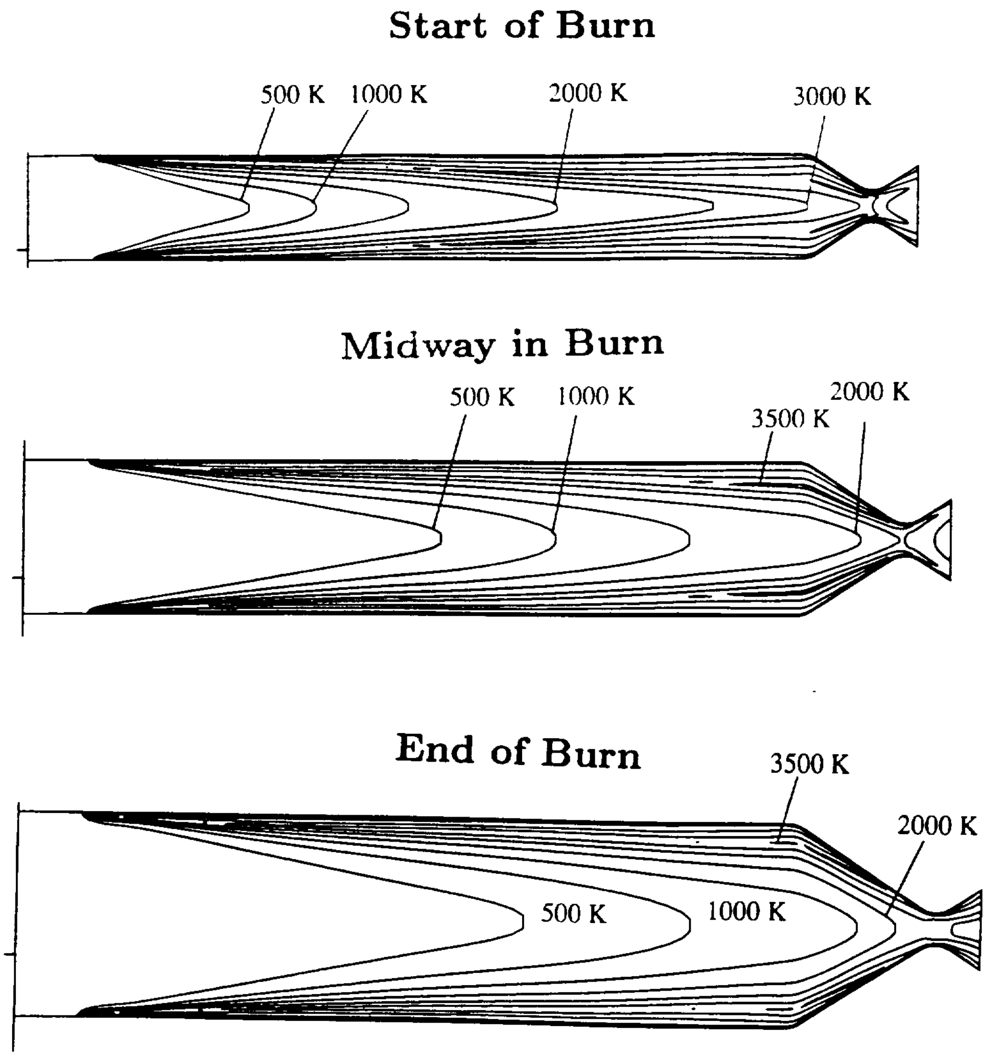

Figure II.3.3 Temperature contours at three stages in the burn. Conditions are the same as those in Fig. II.3.2.

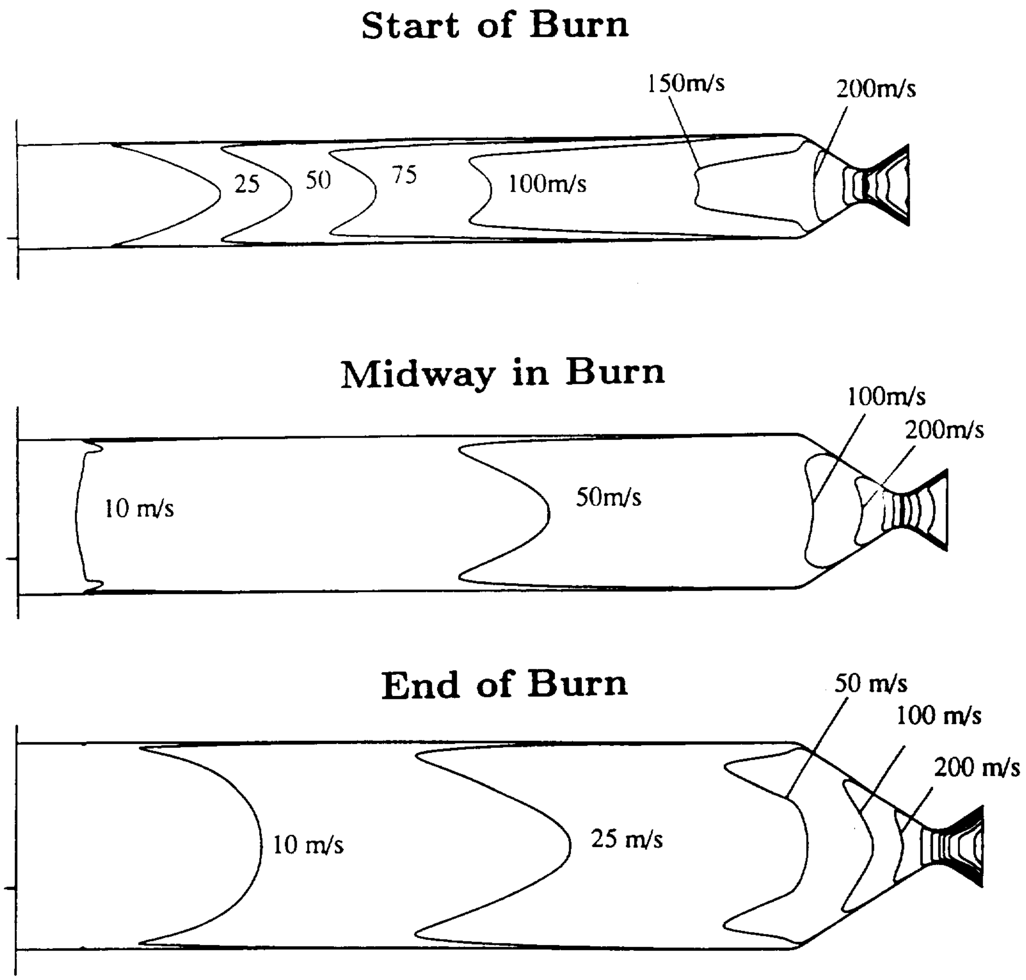

Start of Burn

Midway in Burn

End of Burn

Figure II.3.4 Velocity contours at three stages in the burn. Conditions are the same as those in Fig. II.3.2.

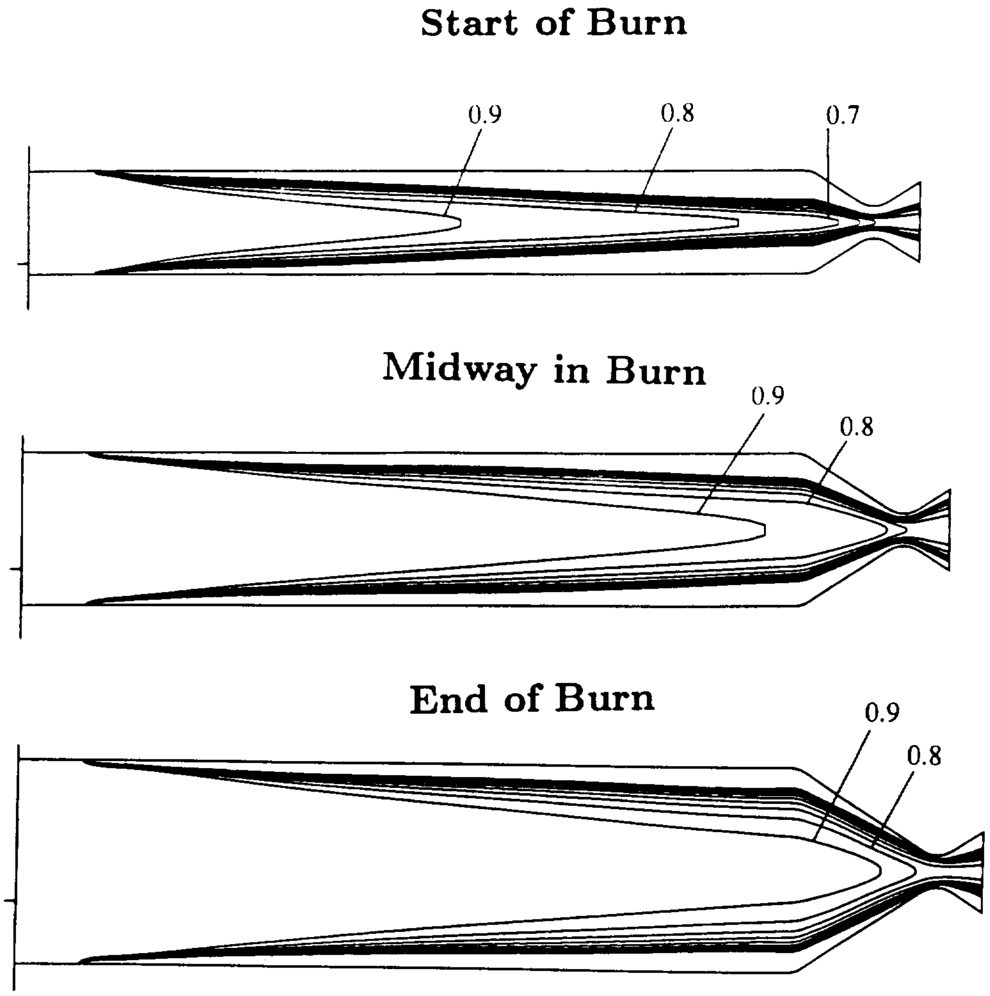

Figure II.3.5 GOX mass fraction contours at three stages in the burn. Conditions are the same as those in Fig. II.3.2.

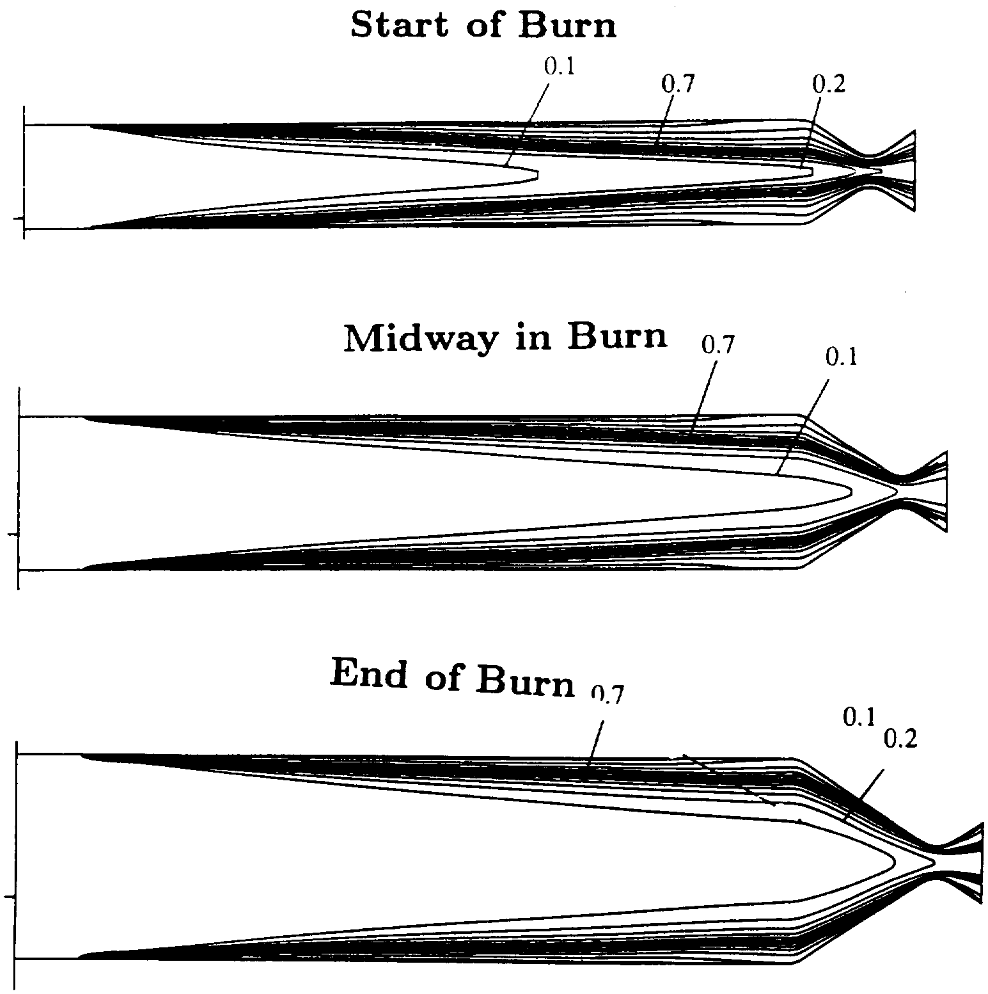

Start of Burn

Midway in Burn

End of Burn

Figure II.3.6 Carbondioxide contours at three stages in the burn. Conditions are the same as those in Fig. II.3.2.

all the way to the centerline of the port, while at the end of the burn, the temperature contours show the flame as remaining close to the fuel surface. This indicates that during the later stages of the burn, the incoming GOX is not fully utilized.

Corresponding contours of gas velocity at the three stages in the burn are shown in Fig. II.3.4. The velocity contours show that the heat addition (due to combustion) and the mass addition (due to fuel regression) lead to dramatic acceleration of the core gases. Again, the acceleration is observed to be strongest near the start of the burn because of the higher regression rate and the smaller port area. As the burn proceeds, the gas acceleration becomes noticeably less pronounced. These plots then clearly demonstrate the relationship between the fluid dynamics and the surface heat fluxes. Higher regression rates lead to faster gas velocities, which consequently results in increased convective heat fluxes. Larger convective fluxes in turn lead to increased pyrolysis rates and increased regression rates.

Examination of the velocity contours in Fig. II.3.4 also reveals that the hybrid flowfield does not, in fact, correspond to a boundary layer flowfield. The strong acceleration of the core gases as well as turbulent diffusive processes causes rapid development of the flowfield. In fact, the velocity contours show evidence of a region of constant velocity at the boundary layer edge only near the leading edge of the fuel slab. In the early stages in the burn, the boundary layer core is observed to be extremely shortlived, while towards the later stages in the burn, when conditions are not quite so severe, the boundary layer region is observed to persist longer, extending roughly to half-length of the fuel slab.

Corresponding contours of GOX and CO_2 mass fractions are given in Figs. II.3.5 and II.3.6 respectively. The GOX contours show that consumption of the oxygen in the core gases is more efficient in the early stages in the burn. However, it is apparent that, even in the beginning stages, the GOX is not completely consumed. At this instance, the integrated fuel mass flux at the fuel surface indicates that the O/F ratio in the combustor is about 1.7, indicating that the combustor is fuel-rich (the stoichiometric ratio is about 3.2). The presence of unburned GOX at the start of the burn is therefore an indication of the degree of mixing in the combustor. Towards the end of the burn, substantial amounts of GOX remain in the core flow. At this stage, the overall O/F ratio in the combustor is 3.2, which is very nearly stoichiometric. It should be pointed out that the experimental configuration includes a mixing chamber in the aft-section of the combustor. The computational geometry is somewhat simplified in this region and it is likely that the computational results under-predict the aft-mixing of the fuel and oxidizer. Since the present study is focused on characterization of the surface regression rate, the details of the aft-section are not crucial to the analysis. Clearly, these details should be included for more accurate estimates of overall combustion efficiency.

The axial variation of the total mass flux ($\dot{m}$) and the specific mass flux (G) are given in Fig. II.3.7. Both plots reflect the increase in the flux due to the mass addition from the fuel pyrolysis. Note that the axial variation in the regression rate (Fig. II.3.2) does not follow the trend in G versus x. Figure II.3.7 also shows the axial variation of the product ρu at the centerline of the chamber. This quantity should represent the conditions at the edge of the boundary layer *if* the flowfield is indeed a 'boundary-layer' flowfield. ρu is observed to vary dramatically as we move downstream. It starts of as being the same as the head-end specific mass flux (G_o), and then increases rapidly due to the displacement effect of the reacting boundary layer. Following this, the quantity decreases, which corresponds to the decrease in density associated with the heating up of the core gases by diffusion. Finally, it starts to increase again because of the effect of mass addition to the chamber. The regression rate clearly does not follow these trends in ρu.

These results bring to question the validity of the boundary layer assumption and its use in the estimation of local and global regression rates. Indeed, in Part I of this study, an experimental correlation was developed to fit the measured regression rate data and was found to depart considerably from the standard boundary layer correlation. In a later section of the present theoretical investigation, we will show further that the regression rate is dependent on the geometry as well as the size of the configuration, a result which renders the boundary layer estimates even less reliable.

II.3.2 Calibration of Computational Model

Both instantaneous and time-averaged regression rates have been experimentally obtained as discussed in Part I of this report. The instantaneous results are obtained at several axial stations using two independent techniques—ultrasonic pulse-echo analysis and X-ray radiography. Time-averaged results are obtained by measuring pre- and post-firing fuel slab web thickness using calipers at several axial stations along the length of the fuel slab. In the computational study, we compare the computational predictions with both the instantaneous and averaged data for several of the experimental runs. In addition to providing a database for validating the computational results and trends, the experimental

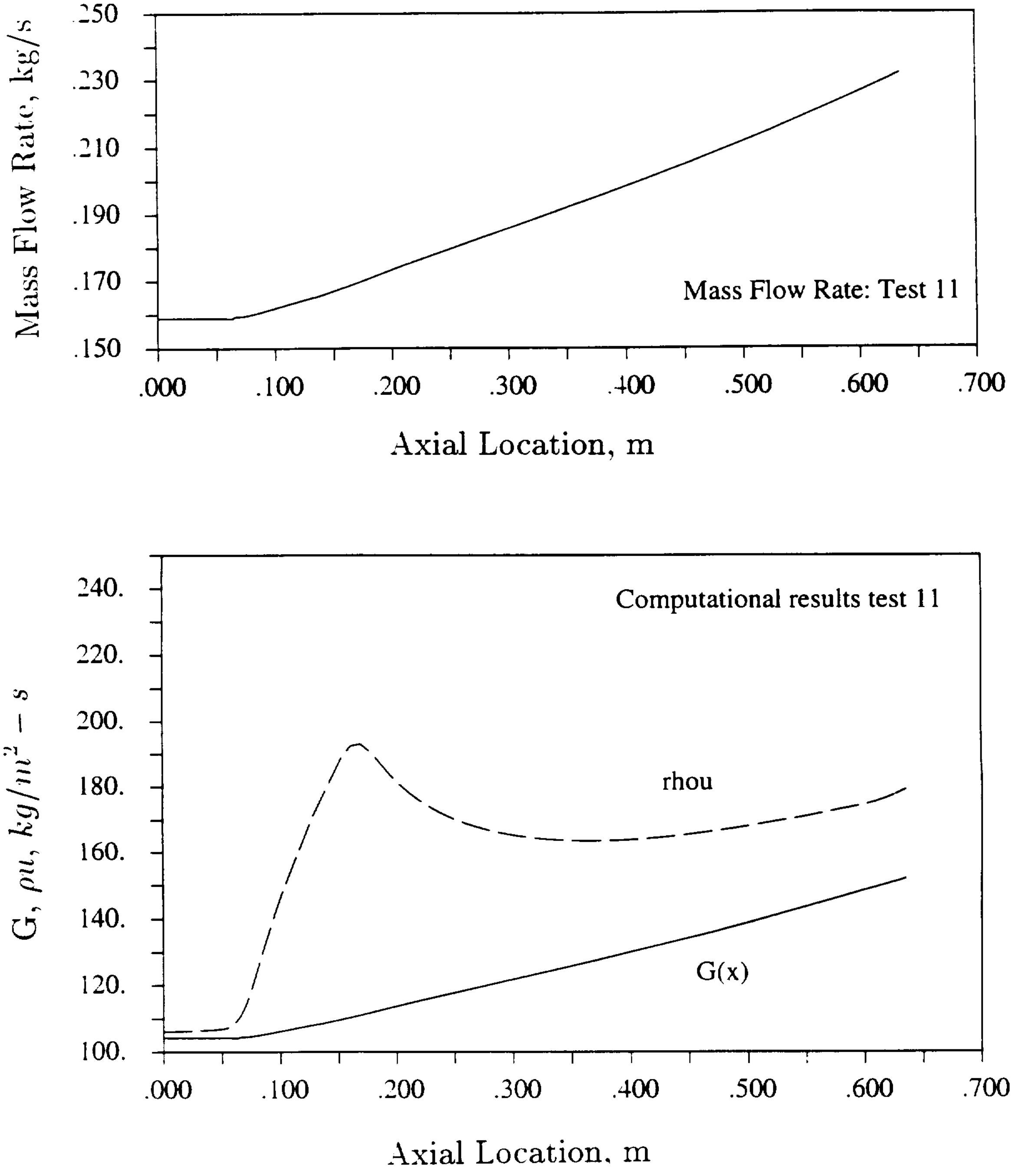

Figure II.3.7 Axial variation of mass flow rate, specific mass flux G and centerline ρu for conditions mid-way through the burn of Test 11.

data are also used to estimate the relative magnitude of radiation in the energy balance at the fuel-gas interface. The phenomenological radiative transfer model sedin this study is calibrated using these guidelines, as discussed in this section.

Time-averaged regression rate data from Test 11 is used to calibrate the radiative transfer model. To obtain an 'averaged' regression rate from the computational data, we perform a simple average of the computed regression rates for *five* different stages in the burn. Figure II.3.8 shows this averaged quantity as a function of axial distance for the representative test case. Figure II.3.8 also shows the computed regression rate obtained midway through the burn. It is observed that the 'average' regression rate corresponds very closely with the 'midway' result. The 'midway' result is then used to calibrate the model against the experimental data by systematically varying the radiative absorption co-efficient of the gas. Further, in many of the results presented in this report, we employ the computations at midway through the burn as representative of an average regression rate. This procedure enables a considerable savings in computer time since only a single calculation is necessary to obtain the average regression rate for each operating condition.

Figure II.3.9 shows the computed results with and without radiation along with the time-averaged experimental data for Test 11. It is apparent that, for this condition, the regression rate is somewhat under-predicted when radiation effects are ignored. In particular, at the mid-location of the fuel slab, the computed regression rate is about 0.8 mm/s, while the experimental rate is 0.9 mm/s, a discrepancy of about 10 %. In the calculation with radiation effects included, the radiative absorpotion coefficient was varied until a close match was obtained with the experimental data at the mid-location on the slab. Once calibrated, the radiative properties were held fixed for all the parametric studies performed.

With the calibrated radiative transfer model, the overall agreement is observed to be reasonably good. The axial variation of the regression rate is qualitatively well-predicted. The regression rate decreases initially near the leading edge and then gradually increases. These trends follow from the trends in the convective heat flux, which is discussed later. The computed values are observed to be somewhat under-predicted near the leading edge and over-predicted near the end of the slab. Near the leading edge, the experiments indicate an initial laminar region, which is followed by a transition region, before the flow becomes fully turbulent. In the computational model, since the $k - \epsilon$ model cannot represent transition to turbulence, the leading edge effects cannot be accurately captured.

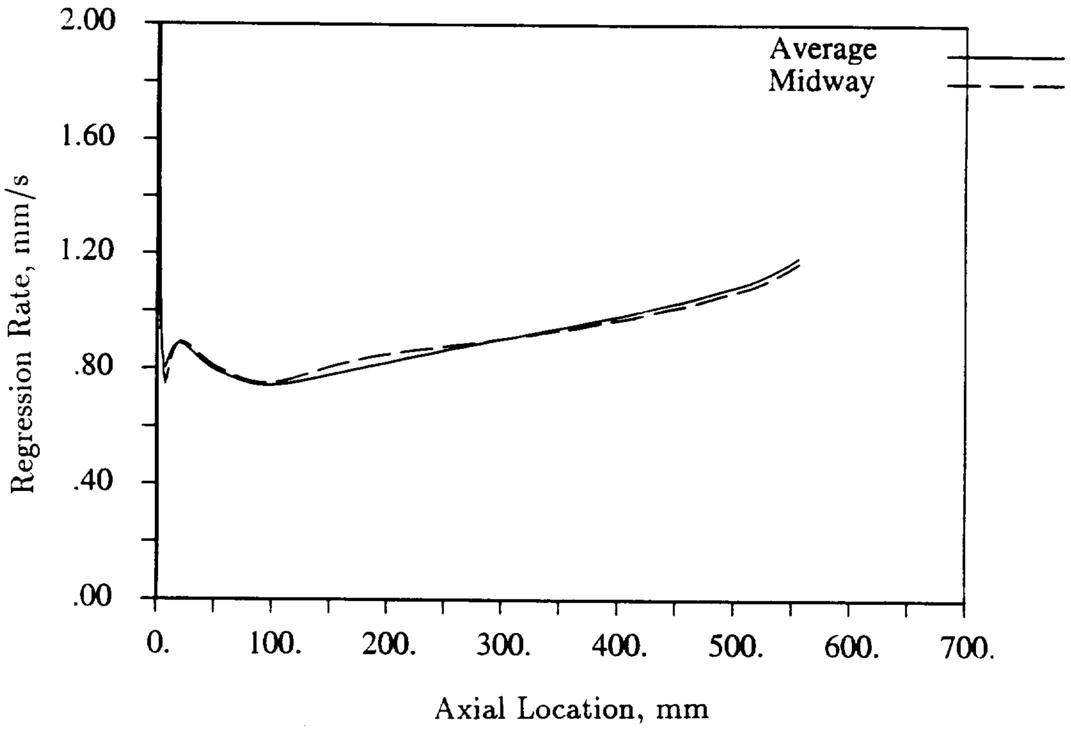

Figure II.3.8 Comparison of time-averaged regression rate from computations at five stages in the burn and the regression rate computed at about mid-way through the burn. Conditions same as in Fig. II.3.2.

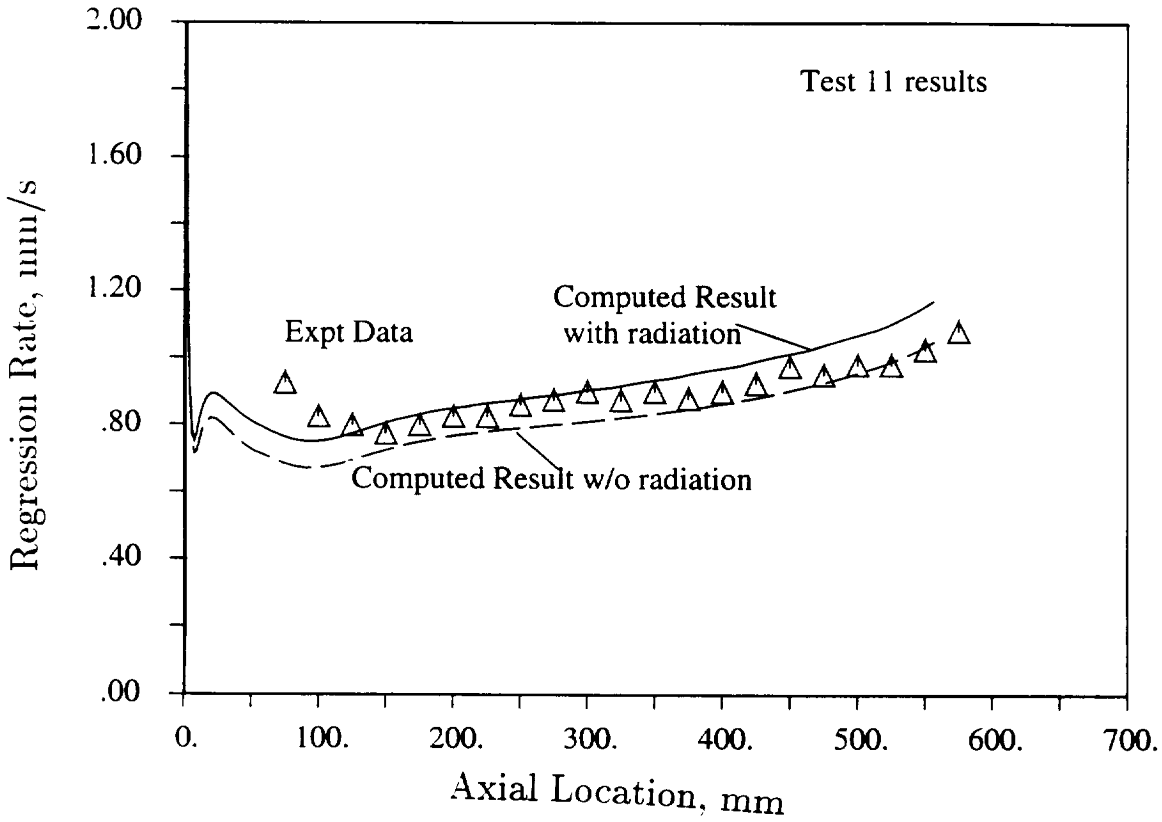

Figure II.3.9 Comparison of computed regression rates midway through the burn with experimental estimates of average regression rates for Test 11, G=165 $kg/m^2 - s$ (or 0.23 $lbs/in^2 - s$).

II.3.3 Parametric Regression Rate Studies

Detailed comparisons of the fuel surface regression rate have been made between the computational and experimental results for several test runs. Figure II.3.10 shows the comparison of the time-averaged regression rates for three such cases—tests 8, 9 and 11. The GOX flow rate for the tests were: 0.1 kg/s (Test 8), 0.16 kg/s (Test 11) and 0.2 kg/s (Test 9). The specific flow rates for each case were 105, 165 and 210 $kg/m^2 - s$ (0.15, 0.23 and 0.3 $lbs/in^2 - s$) respectively. The experimental results are time-averaged regression rate data over the whole test, while the computations show the results midway through the burn (representing an approximate "average" regression rate). Fairly good agreement can be observed over the most of the length of the fuel slab. Importantly, the relative change in the regression rate as a function of the GOX flow rate is well-predicted. This indicates that the balance between convective and radiative effects are well predicted over a range of flow rates. The greatest discrepancy is near the leading edge of the fuel slab, where transition from laminar to turbulent flow may impact the comparisons.

Comparison of the predicted and measured values of the instantaneous regression rate at a given axial location for Tests 9 and 17 is given in Fig. II.3.11. The instantaneous measurements, obtained using the ultrasonic pulse-echo system, show that the regression rate is at its maximum near the start of the test and decreases throughout the burn. The comparisons of the computational predictions with the experimental measurements are observed to be reasonably good. As noted earlier, the decrease in regression rate is due to the increasing port-width caused by the regressing fuel surface, which in turn results in decreasing values of the the specific flow rate, G. The relationship between G and the heat fluxes to the fuel (which control the fuel regression rate) will be addressed in the next section.

We note that Test 17 has a GOX mass flow rate of 0.36 kg/s and an initial head-end $G = 370 kg/m^2 - s$ ($0.56 lbs/in^2 - s$). This corresponds to the highest flow rate tested in the experimental study. It is encouraging to note that the computational predictions remain in good general agreement with the data even at this much higher value of G. Moreover, the temporal variation of the regression rate is also very well-represented by the computational model.

The fuel surface temperature is closely related to the regression rate through the Arrhenius expression used for the pyrolysis rate. Figure II.3.12 shows the predicted fuel

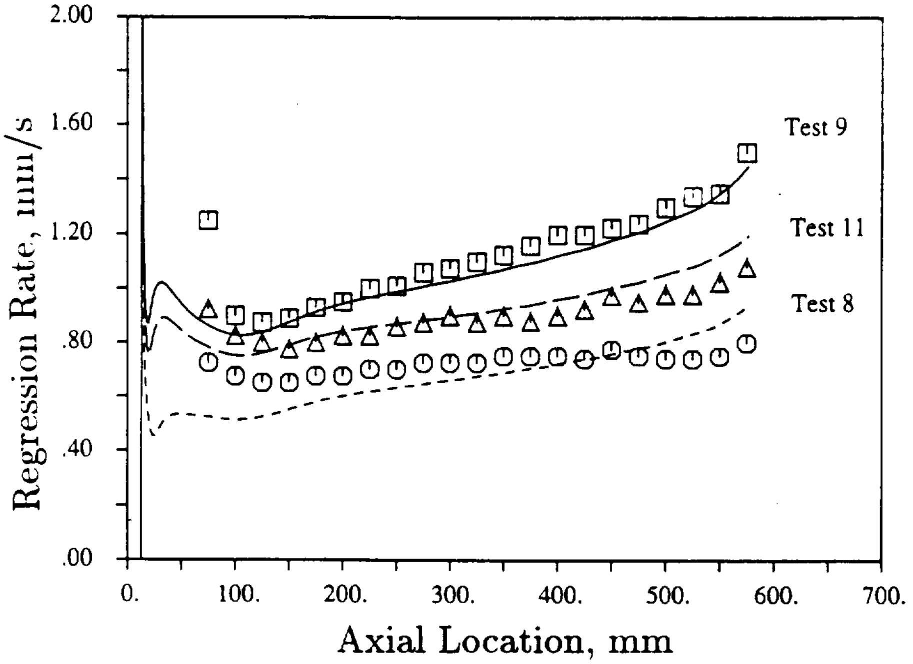

Figure II.3.10 Comparison of computed regression rates midway through the burn with experimental estimates of average regression rates for Tests 8, 9 and 11. G=100, 165 and 210 $kg/m^2 - s$ (or 0.15, 0.23 and 0.3 $lbs/in^2 - s$).

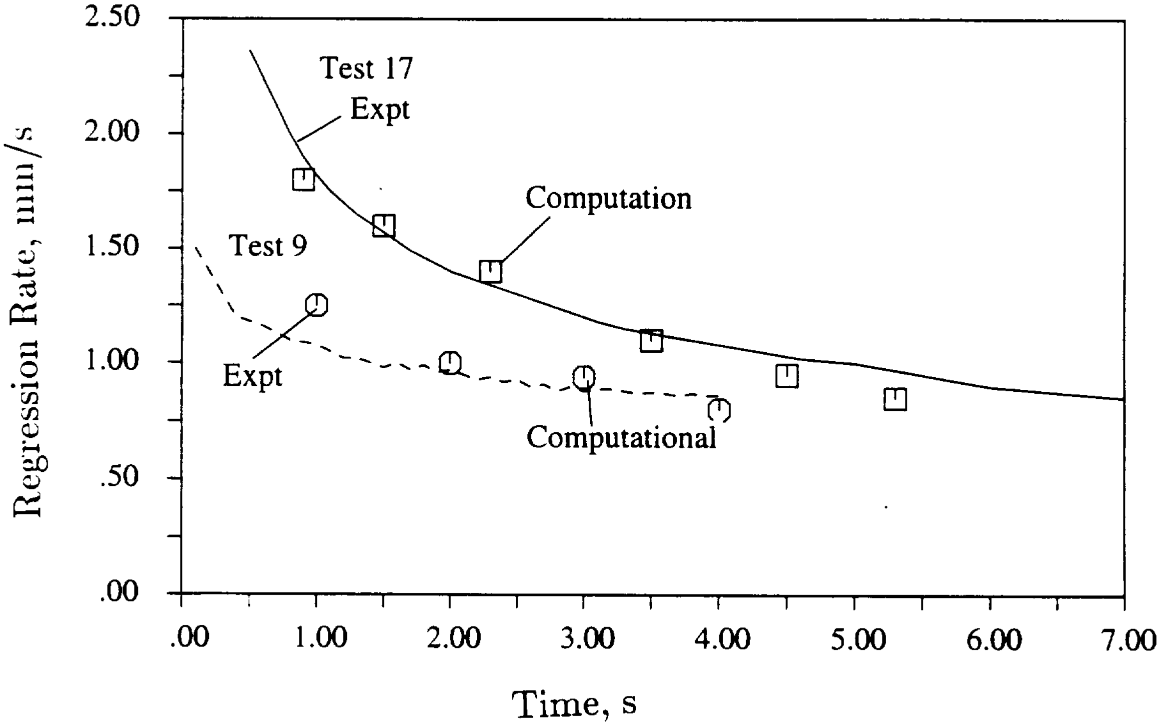

Figure II.3.11 Instantaneous regression rate: measurements and computations. Results shown for a fixed axial location. Conditions correspond to Test 9 and Test 17.

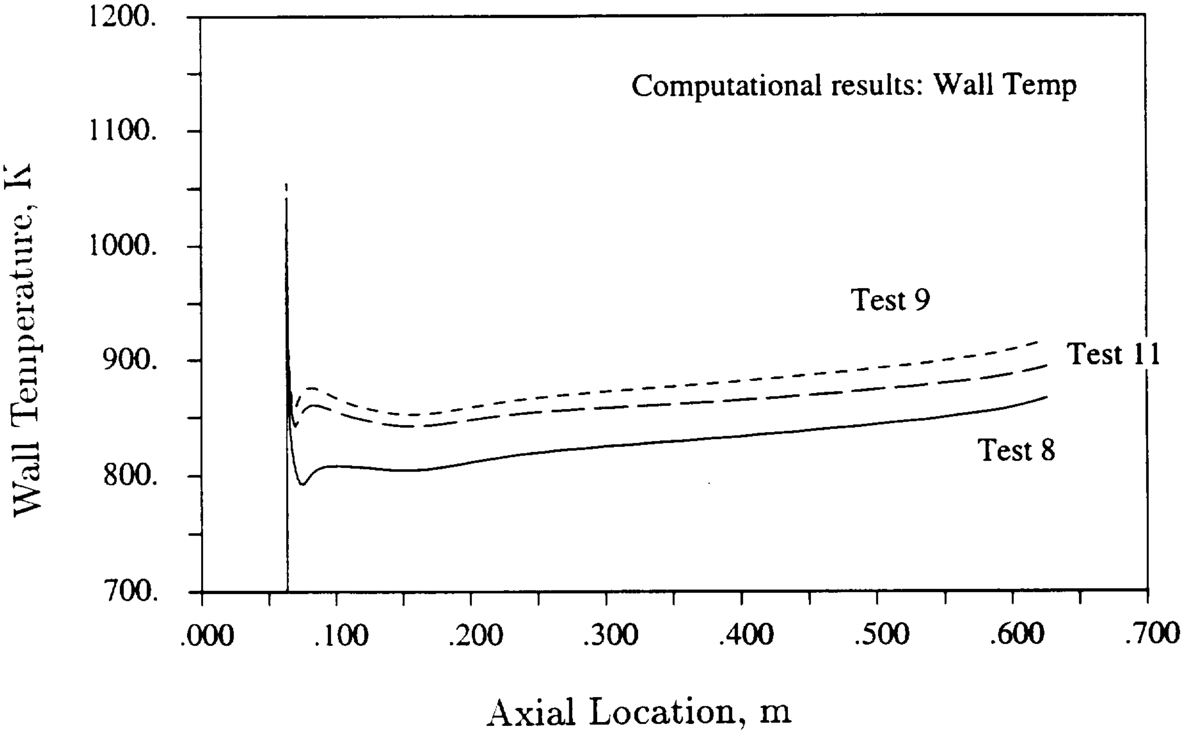

Figure II.3.12 Fuel surface temperature mid-way in the burn for Tests 8,9 and 11.

surface temperatures for the three of the test cases. Note that the surface temperature follows the trends in the regression rate. For the cases shown, the wall temperatures are in the range of 800 to 900 K, which is in reasonable agreement with experimental estimates of 900 to 1000 K. Better agreement may be obtained by fine-tuning the pyrolysis expression. However, this was not attempted in the current study and the pyrolysis expression suggested by Brill *et al.* was consistently used (Table II.2.1) in all of the computations.

II.3.4 Convective and Radiative Heat Fluxes

The fuel surface regression rate is determined by the rate of pyrolysis of the fuel and the energy balance at the solid/gas interface. In general, both convective and radiative heat transfer effects contribute to the surface energy balance. The individual convective and radiative heat fluxes are given in Fig. II.3.13 for three of the test conditions presented in the previous section. As noted earlier, the radiation model was calibrated using the experimental data of Test 11 ($G_o = 0.23 lbs/in^2 - s$). For this test case, the radiative fluxes contribute about 10-15% of the total wall heat flux (at mid-location on the fuel slab). It is interesting note that the convective heat fluxes steadily decrease with decrease in the specific flow rate G. The radiative fluxes, on the other hand, are more or less invariant to the specific flow rate. Thus, radiation becomes more of a factor at low specific flow rates. For the conditions in Test 8 ($G_o = 0.15 lbs/in^2 - s$), radiation accounts for almost 25% of the total heat flux. Under such conditions then the proper accounting of radiative effects becomes a signficant issue. By contrast, at the higher flow rate of Test 9 ($G_o = 0.3 lbs/in^2 - s$), radiation accounts for less than 10% of the total heat flux. Finally, for the even higher flow rate of Test 17 ($G_o = 0.56 lbs/in^2 - s$), the radiative contribution (not shown here) is negligibly small and the convective heat flux accounts entirely for the heat flux on the fuel surface.

These estimates of the relative importance of radiative heat transfer are in good general agreement with the estimates obatined from the experimental correlations presented in Part I of this report. The experimental results indicate that radiation contributes about 10% of the total heat flux at a specific mass flux of $G_o = 140 kg/m^2 - s$ (or $0.21 lbs/in^2 - s$) and that this contribution falls to about 6% for a mass flux of $G_o = 200 kg/m^2 - s$ (or $0.3 lbs/in^2 - s$). It should be borne in mind that the experimental

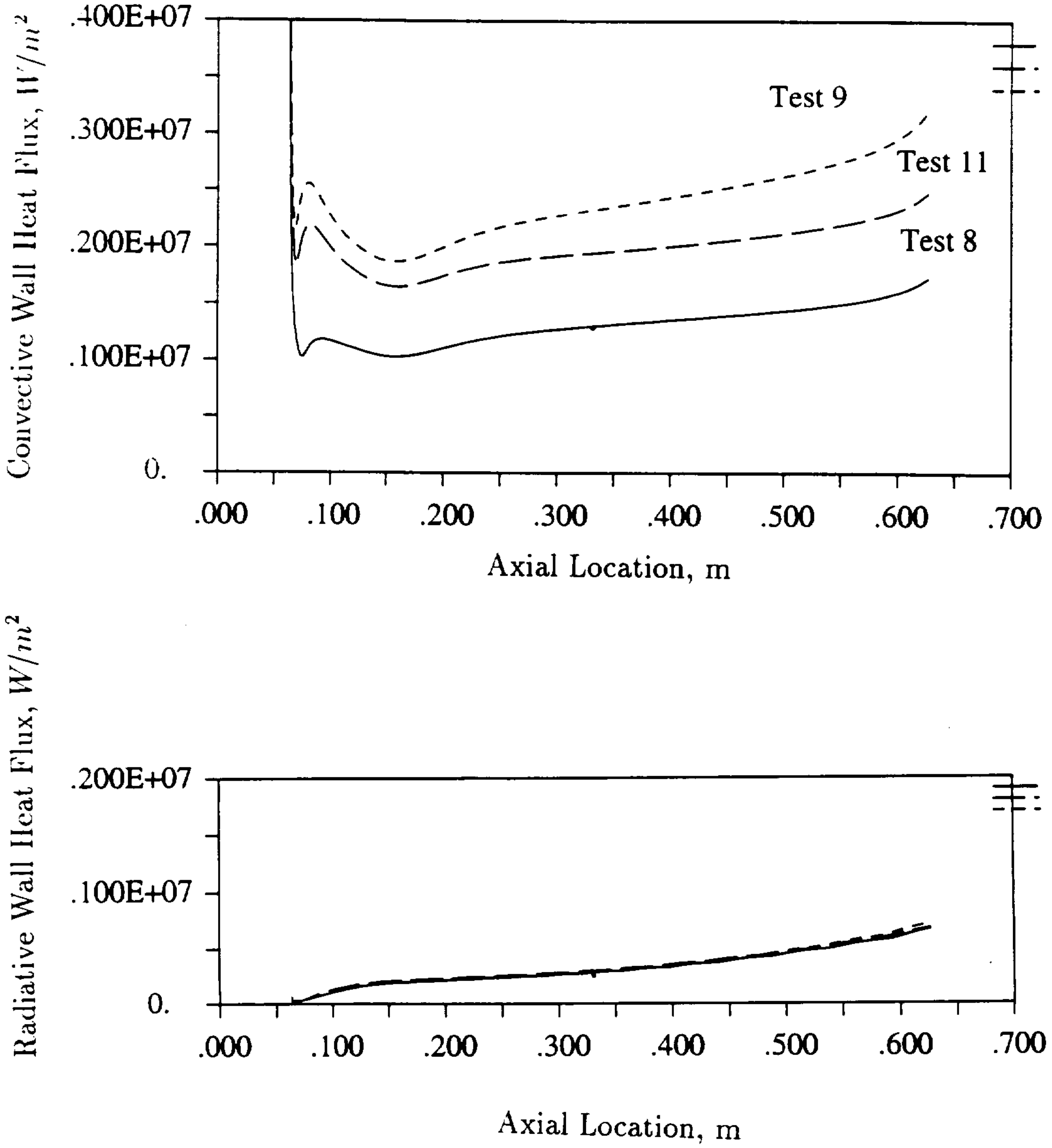

Figure II.3.13 Convective and radiative heat fluxes on the fuel slab surface for Tests 8. 9 and 11.

estimates of radiative transfer are not based upon measurements; rather, they are obtained from the experimental correlation that best matches the data. Under the circumstances, there appears to be good qualitative agreement between the computations and the experiments.

Similar heat flux results are presented in Fig. II.3.14 for Test 11 at three different stages in the burn. Again, the convective heat flux is observed to be strongly influenced by the changing conditions as the burn progresses, while the radiative flux is relatively unaffected. We note also that the decrease in the convective heat flux accompanies the reduction in the inlet specific flow rate as the burn progresses.

It is important to consider the reasons for the behaviour of the convective and radiative heat fluxes under different flow conditions and at different stages in the burn. For a given configuration, the higher the specific flow rate, the higher the gas velocity in the port. Consequently, the Nusselt number of the core flow becomes higher leading to higher convective heat transfer rates from the hot gas to the solid fuel surface. It should be pointed out that the addition of mass by the regressing fuel surface complicates the issue and renders invalid the use of standard boundary layer Nusselt number correlations. Other complexities arise due to the effects of size scale-up and geometric configuration, issues that are addressed in detail in later sections. Simplified hybrid combustor models based on such boundary layer correlations may then seriously misrepresent the regression rate characteristics in the combustor.

The radiative fluxes, on the other hand, are relatively insensitive to the flow conditions. This is because radiation, unlike convection, is not affected by the gas velocity. Radiation is primarily determined by the temperature field and the geometric configuration of the medium. At the different flow rates, although the gas velocity field is very different, the the temperature contours in the vicinity of the flame are similar. In all cases, the peak temperatures are consistently in the 3000-3500 K range. The radiative heat flux incident on the fuel surface is therefore of similar magnitude under the conditions considered here.

In conclusion, we note that the convective heat flux increases with specific flow rate, while the radiative heat flux is more or less constant. Then, the total heat flux increases with flow rate, resulting in increased fuel surface regression rates. Further, we note that radiation plays an important role in the total energy balance only at low specific flow rates. At high specific flow rates (above $0.4 lbs/in^2 - s$), the radiative contribution is generally negligibly small. In the previous section, we compared the regression rate predictions with

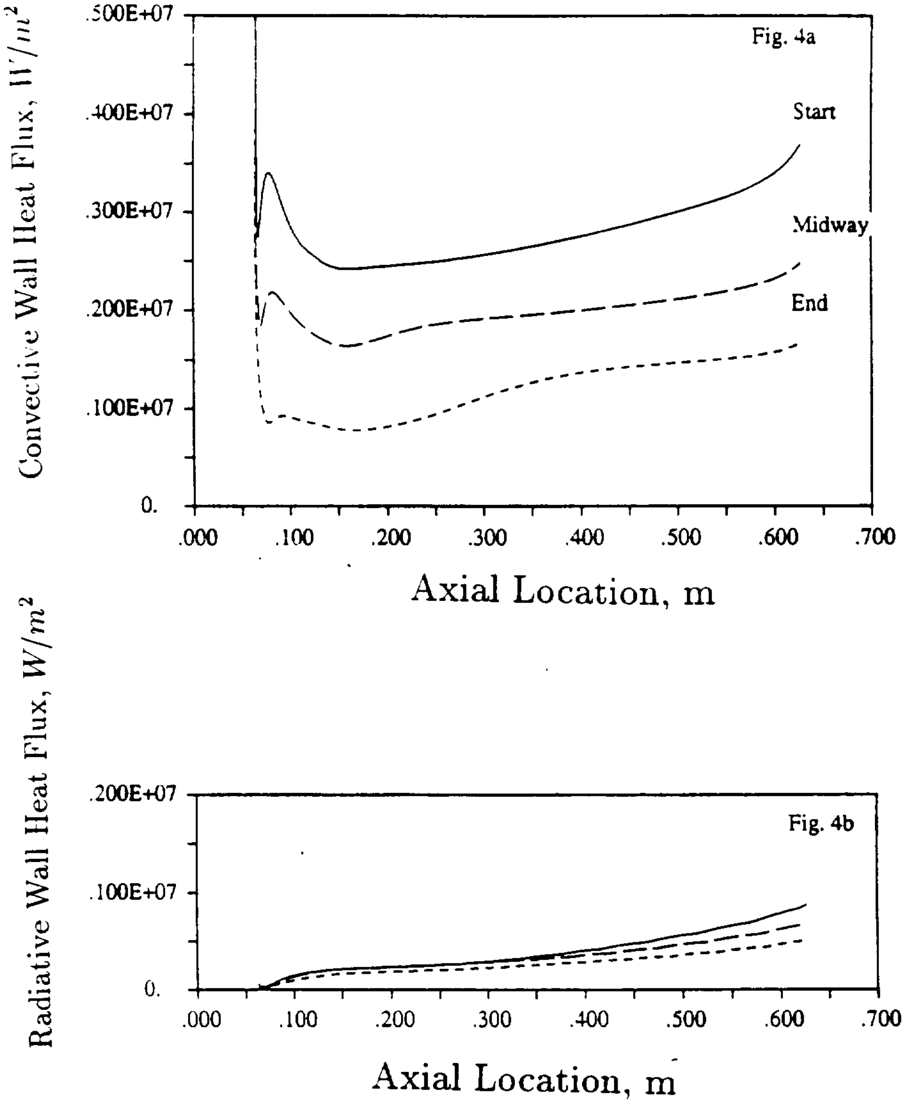

Figure II.3.14 Convective and radiative fluxes on the fuel slab surfaces at three stages in the burn. Conditions are the same as those in Fig. II.3.2.

expermental data over a wide range of flow rates. In general, the computational results faithfully followed the experimental trends. This indicates that the changing balance between convection and radaition under different flow conditions is well represented by the present computational model.

II.3.5 Sensitivity of Pyrolysis Model

The results presented so far have utilized the model suggested by Brill *et al.* [16] for the pyrolysis of HTPB. This is the most recent work in this area and is therefore considered to be the most reliable pyrolysis model. Previous researchers have utilized the model developed by Cohen *et al.* For the sake of comparison and to ascertain the sensitivity of the results to the choice of pyrolysis model, we present regression rate and wall temperature results obtained using the Cohen model. These results are summarized in Fig. II.3.15 and are for the conditions corresponding to Test 11. The results obtained using the Brill model are also included to facilitate the comparison. It is interestig to observe that the results appear extremely sensitive to the model co-efficients. The Cohen model under-predicts the regression rate by almost 25-30 %. This discrepancy cannot be accounted for by radiative transfer since this would mean a total radiative contribution of over 50 %, which is not experimentally supportable. Thus, it appears that the Brill model provides better results than the Cohen model. It is also interesting to note that the Cohen model results in wall temperatures in the range of 1000 to 1100K, about 150 K higher than the Brill model.

II.3.6 Sensitivity of Radiative Transfer Model

We have hitherto represented radiation using the approximation of a purely emitting medium. This approximation is valid in the limit of optically thin media. However, in practice, it is likely that the gases are optically thick in some regions of the flowfield, particularly in the 'sooty' regions of the flame. A detailed consideration of these effects is difficult because it would require detailed knowledge of the radiative properties of the gaseous medium. Instead, in this section, we examine the results if the entire medium were assumed to be optically thick. This would then give us some insight into the behaviour of radiative effects under the two extreme situations.

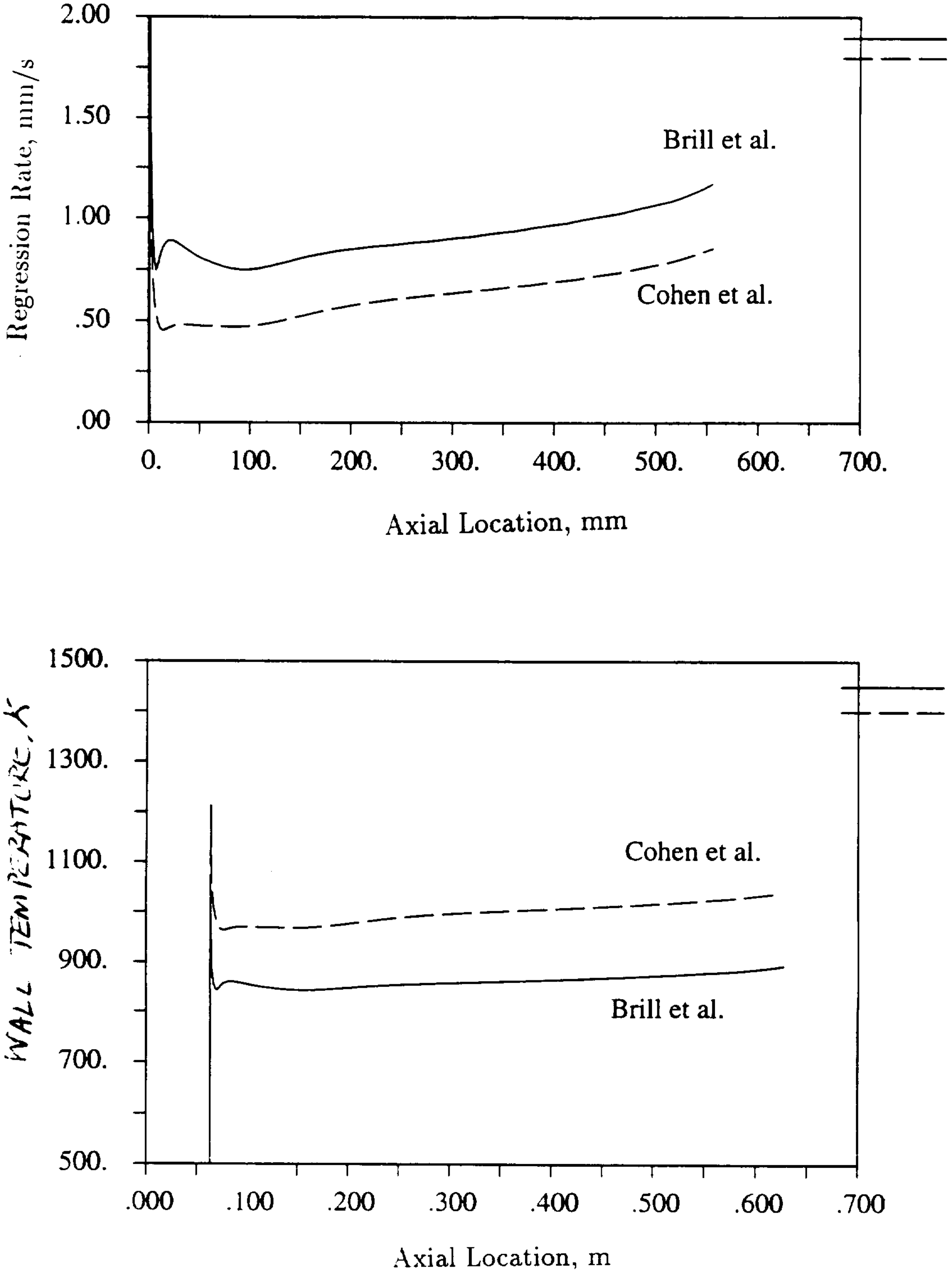

Figure II.3.15 Computed results using two pyrolysis models: (a) Cohen *et al.* [15]. and (b) Brill *et al.* [16].

3·15

Figure II.3.16 shows the results for the three test conditions examined earlier using the 'optically thick' radiative transfer model. Regression rate predictions are observed to be qualitatively similar to the 'optically-thin' result, though there are some quantitative differences. The radiative fluxes shown below reveal that radiative transfer is now a function of the flow conditions, a trend that is markedly different from the 'optically thin' case. The reason for this behaviour becomes obvious when it is noted that, for optically thick media, the radiative transfer is modelled as a diffusive term (Eqn. 2.13). Thus, the radiative flux depends on the flow rate in much the same manner as does the convective flux.

With the optically-thick approximation, therefore, the radiative contribution to the total fuel surface heat flux tends to be more or less constant with changes in the flow rate. We note that this is not the case in the experimental estimates of the radiative contribution. We noted earlier that radiation tends to be more prominent at low flow rates and becomes negligibly small at high flow rates. The 'thick' model of radiation does not reflect this trend. Therefore, modeling the entire medium as optially thick is not a good approximation under the circumstances of interest here. However, as we noted earlier, it is likely that some regions of the flow field are optically thick. The presence of optically thick regions in the flowfield becomes a particularly important issue when we consider how radiative effects scale up with size.

II.4 Comparison with Other Test Data

As a further further step in the validation of the computational model, we use the test results of Strand *et al.* [3,4]. These experimental results are restricted to somewhat lower specific flow rates (up to about 0.15 $lbs/in^2 - s$ or about 100 $kg/m^2 - s$). Computational results for $G = 20N/m^2 - s$ are shown in Fig. II.4.1. In the computations, we continue to use the geometry of the experimental slab burner configuration. Other conditions are also taken to be the same as those used in the previous computations.

The regression rate corresponding to this lower specific flow rate (Fig. II.4.1a) is about 0.4 mm/s at the mid-location of the fuel slab. Experimental measurements of the global regression rate (time and space averaged) is about 0.3 mm/s for this specific flow rate. Considering that the computations did not attempt to model the experimental conditions or the thruster configuration precisely, the agreement is quite good. The corresponding

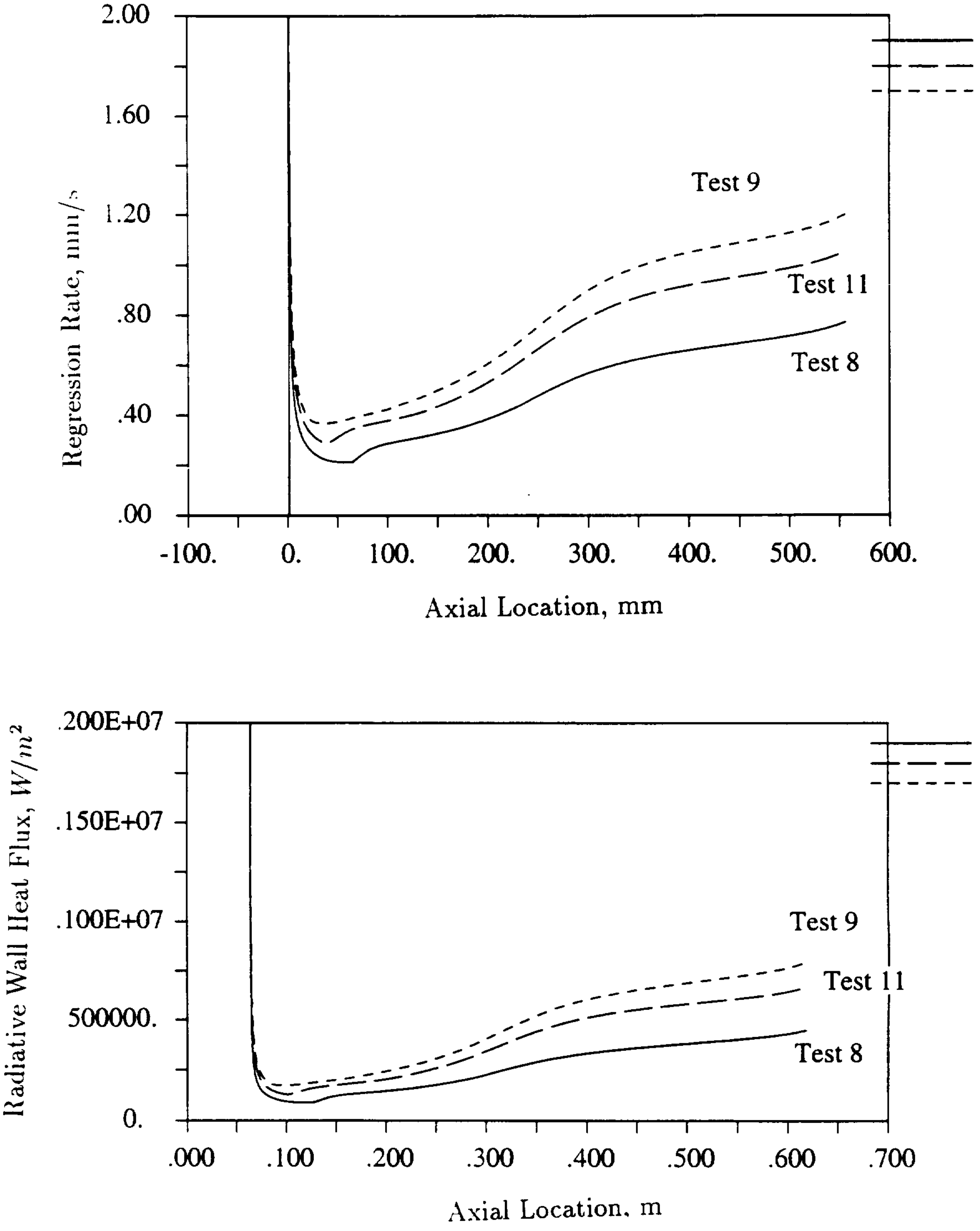

Figure II.3.16 Computed results with an optically thick radiative approximation. Conditions correspond to Tests 8, 9 and 11.

3'6

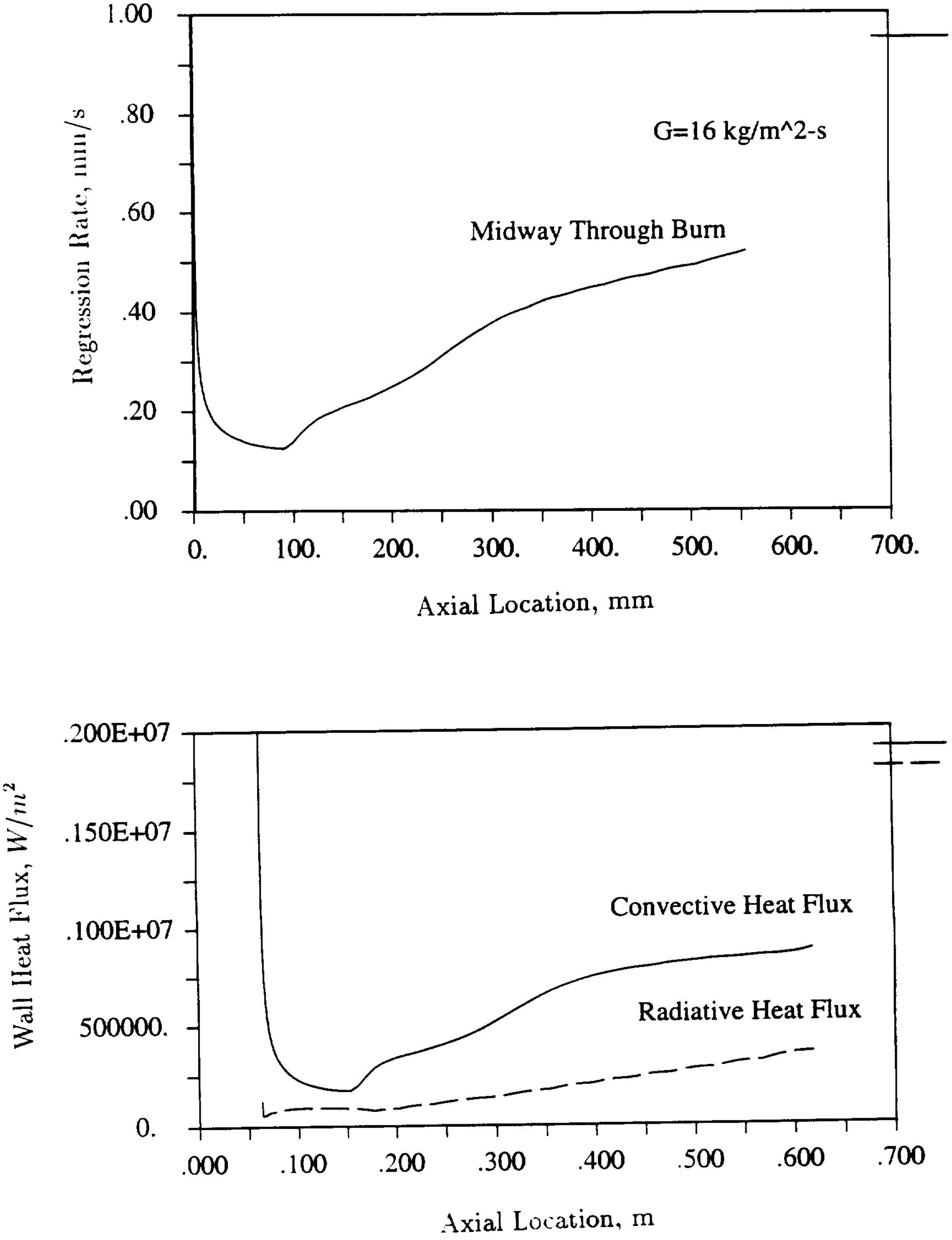

Figure II.4.1 Computed results for a specific flow rate $G = 16kg/m^2 - s$: (a) fuel surface regression rate, (b) convective and radiative wall fluxes.

4.1

convective and radiative fluxes are given in Fig. II.4.1b. Under these operating conditions, the radiative fluxes contribute about 25-30% of the total wall heat flux, which agrees reasonably well with measurement estimates of the total radiation flux on the fuel surface [4].

Computational predictions of the regression data are also compared with global regression rate data obtained from other sub-scale motor tests. These results are summarized in Fig. II.4.2, where the regression rate is plotted against the specific flow rate G. Computational data are shown along with measurement data from General Dynamics-Thiokol-Rocketdyne [1], and the JPL tests [3,4]. All data are for HTPB/GOX. Computational results are shown using solid symbols. We note that good general agreement between predictions and measurements is obtained, without any changes being made to the computational model. These results provide a measure of confidence regarding the applicability of the computational model for further parametric testing.

II.5 COMPARISON BETWEEN PLANAR AND AXISYMMETRIC CONFIGURATIONS

An important step in applying lab-scale measurements to practical configurations is to be able to understand how the results obtained in a planar, slab burner geometry (such as those used in Refs. 3, 4 and 6) would differ from results obtained in an 'equivalent' axisymmetric configuration. There are several potential procedures that can be used for this purpose. The computational model allows us to test these procedures to see which works best, and, more importantly, to understand what the differences are. Further, understanding the differences between planar and axisymmetric configurations may also suggest some of the differences to be expected in the case of the more irregularly shaped ports of practical hybrid configurations (such as the "spoke" sections of "wagon-wheel" grains).

The most obvious method for scaling slab burner results to axisymmetric ports is to set the cross-sectional area and the burning surface area of the axisymmetric geometry equal to those in the slab burner. We will refer to this as configuration A. The rationale behind this selection rests in the assumption that if the same specific flow rate G were maintained in the two configurations, classical boundary layer theory would imply equal surface regression rates (since $r_b \approx G^n$). Maintaining the same G would, in turn, keep the

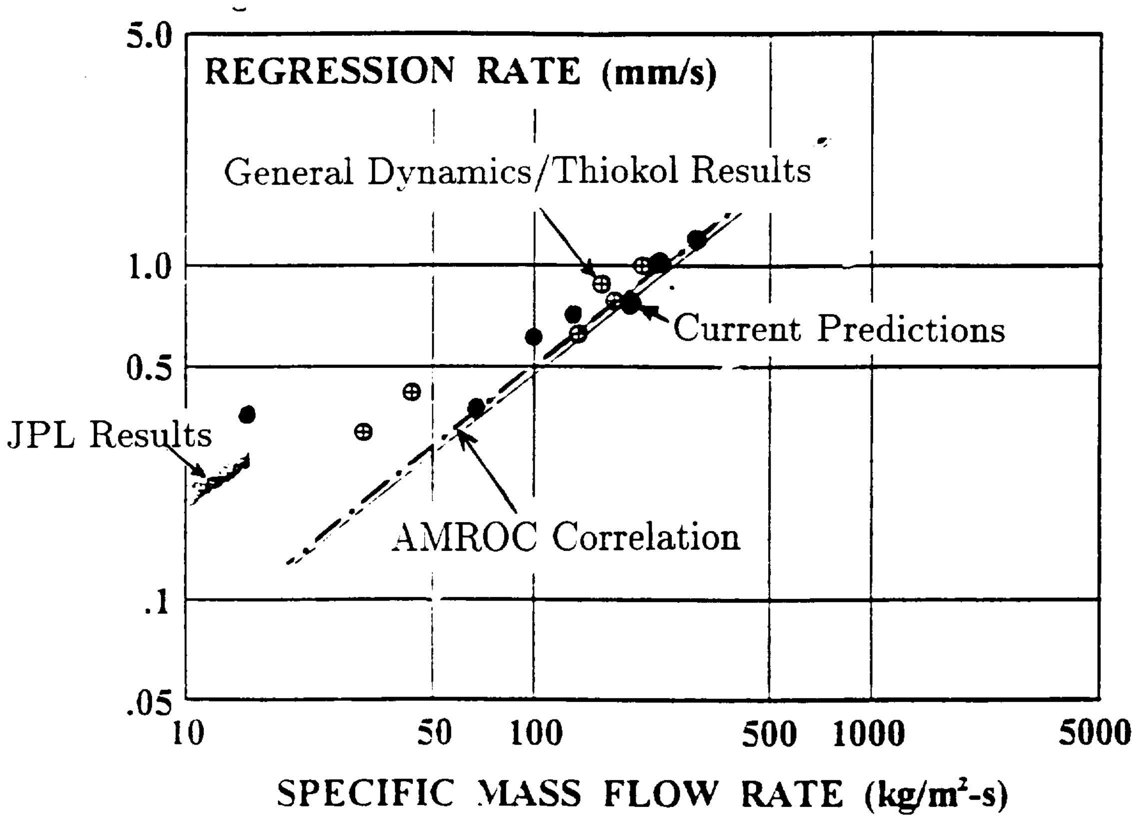

Figure II.4.2 Regression rate vs specific flow rate: comparison of predictions with other test data. G-T-R refers to data reported by General Dynamics, Thiokol and Rocketdyne [1]. JPL refers to the results of Strand *et al.* [3.4]. Test data shown are extracted from Ref. [5].

oxidizer-to-fuel ratio fixed in the two configurations.

In configuration A. we therefore select the radius of the axisymmetric combustion chamber by equating the cross-sectional area of the port with that of the slab burner.

$$\pi r^2 = h \times b \tag{5.1}$$

where r is the axisymmetric port radius, while h is the port height and b the port width of the slab burner port. Note that in this configuration, for the same G. the inlet mass flow rate of the oxidizer is also maintained constant. The second condition of keeping the fuel surface areas equal (at the start of the test) fixes the length of the axisymmetric fuel slab.

$$2\pi r L_{\text{axi}} = 2bL_{\text{2D}} \tag{5.2}$$

where L_{axi} and L_{2D} are the lengths of the axisymmetric and planar fuel slabs.

An alternate axisymmetric configuration, refered to as configuration B, is one in which the distance from the fuel surface to the centerline is the same in both geometries. In other words, the radius of the axisymmetric port is chosen to be equal to the channel half-width,

$$r = \frac{1}{2}h \tag{5.3}$$

This selection, in a sense, maintains a closer geometric/size similarity with the planar configuration. Note. however, that configuration B does not provide the same oxidizer mass flow rate for the same specific flow rate G because the cross-sectional areas are different. In order to maintain the same overall O/F ratio under the same specific flow rate G, we choose the ratio of burning surface area to cross-sectional area to be the same for the two configurations. This condition then specifies the length of the fuel slab.

$$\frac{2\pi r L_{\text{axi}}}{\pi r^2} = \frac{2bL_{\text{2D}}}{h \times b} \tag{5.4}$$

Once again, the design criterion for configuration B assumes that for the same G. the fuel surface regression rate would be the same for the planar and axisymmetric configurations. One of the issues of the present computational study seeks to address is whether such a design strategy is sufficiently accurate.

Regression rate results for both of these axisymmetric configurations (A and B) are given in Fig. II.5.1 along with the corresponding planar result. The inlet specific flow

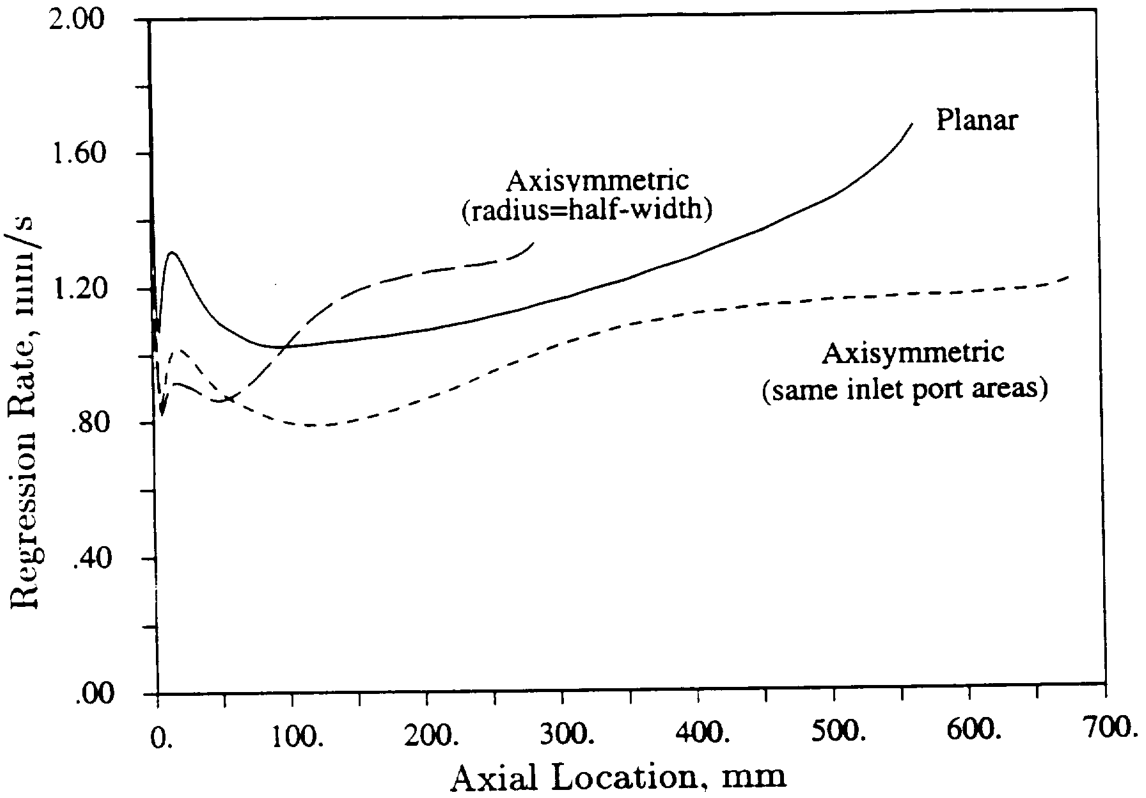

Figure II.5.1 Computed results of surface regression rates for two axisymmetric configurations and the experimental planar configuration. In all cases, $G = 130 kg/m^2 - s$ $(0.18 lbs/in^2 - s)$.

rate, G, for all three cases is $130 kg/m^2 - s$ (or $0.2 lbs/in^2 - s$). As can be seen from the results in Fig. II.5.1, neither of the two choices results in the same fuel surface regression rate in the axisymmetric port as in the slab geometry, a result that is contrary to our initial design assumption. The regression rate for case A is about 25% lower than the planar result, while that for case B is about 25% higher. These results show that the regression rate depends not only on the flow rate parameter G but also on the shape and size of the port configuration. The indication is that boundary layer theory, while capable of providing reasonable qualitative measure of trends within a given configuration, cannot account for differences in port shape and may lead to misleading trends between different configurations. In terms of obtaining reliable design estimates of hybrid combustor performance, it then becomes necessary to use a more comprehensive model such as the present analysis. In the following section, we extend the parametric studies to evaluate how these results scale with size.

II.6 SIZE SCALE-UP STUDIES

The effects of chamber sizing on the regression rate is very important in the design of hybrid rocket motors. Once the oxidizer mass flux and the overall O/F ratio of the motor have been set, the regression rate dictates the port dimensions. A reliable understanding of the effect of size scale-up on the regression rate is imperative if current experimental and test results are to be used to build larger, full-size motors. Our analysis in this section considers the effects of size scale-up between different axisymmetric sizes. The results of these analyses lead to some interesting observations that are not contained in the simpler boundary layer analysis.

Classical hybrid motor theory [1,7] based upon a boundary layer model of the combustion process indicates that the surface regression rate is proportional to the specific oxidizer flow rate, G, taken to some power, n. This relationship is generally expressed as $r_b = G^n$. The analysis further indicates that the regression rate is independent of the pressure. The boundary layer results then suggest that the fuel surface regression rate is the same for all port sizes and shapes, which leads to the natural conclusion that size scale-up is not an issue in hybrid motors. The results of the present complete Navier-Stokes analysis show that the boundary layer analysis omits some important effects. The port size is, in fact, an important parameter in determining the surface regression rate.

To compare the more complete CFD predictions against boundary layer theory, computational results are presented for three different axisymmetric motor sizes. For all three configurations, the non-dimensional chamber length was held constant at $L/D = 35$, the oxidizer flow rate was fixed at the value, $G = 565 kg/m^2/s$ (or $0.8 lb/in^2 - s$), and chamber pressure was set at 900 psia. We refer to the three sizes as the "lab-scale", the "intermediate-scale", and the "full-scale" motors. The respective dimensions of these cases are $L = 23 in$ and $D = 0.66 in$ for the lab-scale motor; $L = 100 in$ and $D = 2.86 in$ for the intermediate-scale motor: and $L = 350 in$ and $D = 10 in$ for the full-scale motor. The length chosen for the sub-scale motor is the same as that used in the companion planar slab burner experiments. It should be noted that keeping the L/D fixed for the three sizes not only ensures geometric smilarity but also maintains the same O/F ratio in the three combustors, provided, that the regression rates are independent of size. The results of this parametric study are summarized in the following sections.

II.6.1 Fuel Surface Regresssion Rate

The predicted surface regression rates for the three motor sizes are presented in Fig. II.6.1 as a function of the actual physical distance from the upstream end. For clarity, the same result is plotted versus the non-dimensional axial distance x/L in Fig. II.6.2. The predictions show that the regression rate decreases significantly as the port dimension is increased. At the mid-point location on the slab (x/L = 0.5), the regression rate is about 3 mm/s for the lab-scale, 2.5 mm/s for the intermediate geometry, and about 2.2 mm/s for the full-scale configuration. An explanation of why the CFD model predicts the regression rate decreases with motor size requires a more detailed consideration of the coupling between the solid-phase pyrolysis process and the gas-phase turbulent diffusion flame. Before we consider this coupling, however, we first check the present predictions with the previous results.

The lab-scale predictions contained in Figs. II.6.1 and II.6.2 are for a similar motor size (albeit an axisymmetric configuration) as those in the previous planar slab burner results in Fig. 3.5. By comparing the present results with the earlier ones, we immediately see that the regression rates here are about two and one-half times greater than the measurements and predictions in Fig. 3.5. The reason, however, is explained by looking at the flow rates. The oxidizer flow rate is also about two and one-half times greater than the largest values

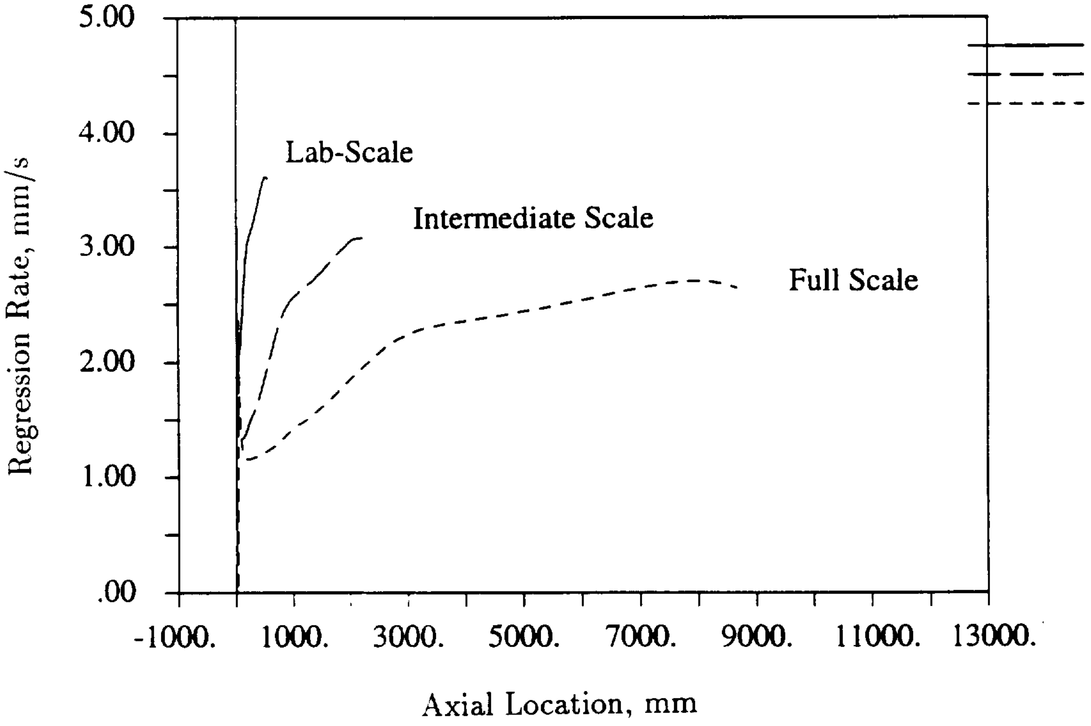

Figure II.6.1 Surface regression rates for the lab scale, intermediate and full scale configurations plotted against physical length along the fuel slabs.

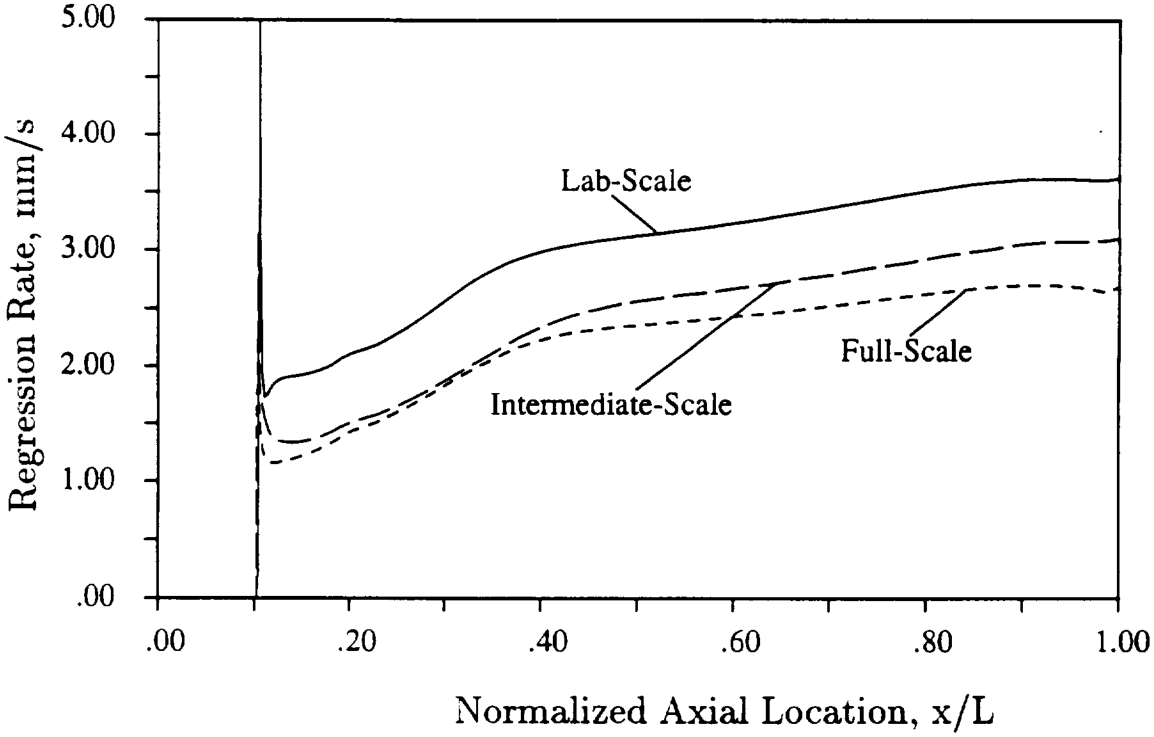

Figure II.6.2 Surface regression rates for the lab scale, intermediate and full scale configurations plotted against non-dimensional axial distance along the fuel slabs.

used in Fig. 3.5. This comparison then suggests that the power-law scaling from boundary layer theory works reasonably well for the two motors of the same size, the differences being accounted for by the planar versus the axisymmetric configurations. Thus, this scaling justifies the higher regression rates predicted for this case. In addition, experiemntal data form other subscale motor firings [1.2] also suggest that the present predictions are reasonable.

II.6.2 Convective and Radiative Fluxes

For an explanation of why the regression rates in Fig. II.6.1 and II.6.2 decrease with size, we need to consider the convective and radiative contributions to the fuel surface heat flux. To obtain an initial understanding of how size affects these fluxes, we first compare the relative flame locations for the three motor sizes. Temperature contours for the three different sizes are given in Fig. II.6.3. The flame location may be approximately identified from the peak temperature. Note that although the plots are labeled in physical units (meters), they have all been scaled to the same size for comparison. The temperature contours in the lab-scale solution show that the flame reaches the centerline before the end of the duct ($x/D = 35$), indicating nearly complete consumption of the oxidizer. by contrast, for the two larger sizes, the flame remains confined to the near wall region and a portion of the core gas remains unburned. This suggests that the flame is nearer to the wall in non-dimensional terms in the larger scale motors, although it is *farther* from the wall in dimensional terms, as noted later. Additionally, this also indicates that the larger motors do not burn as efficiently as the subscale motor. Both of these observations are consistent with the slower surface regression rates that were seen in Figs. II.6.1 and II.6.2 for the larger motor.

To understand these trends better, it is important to examine the relative contribution between the convective and radiative fluxes to the wall heat flux. These components are shown separately in Fig. II.6.4. The qualitative trends are immediately apparent. The convective heat flux decreases with increasing motor size, while the radiative flux increases. The decrease in convective flux is, however, larger so that the net heat flux (the sume of convection and radiation) decreases with size. To better appreciate the behaviour of the radiative and convective contributions, we consider them individually.

The convective heat flux is generally the dominant contributor to the energy balance

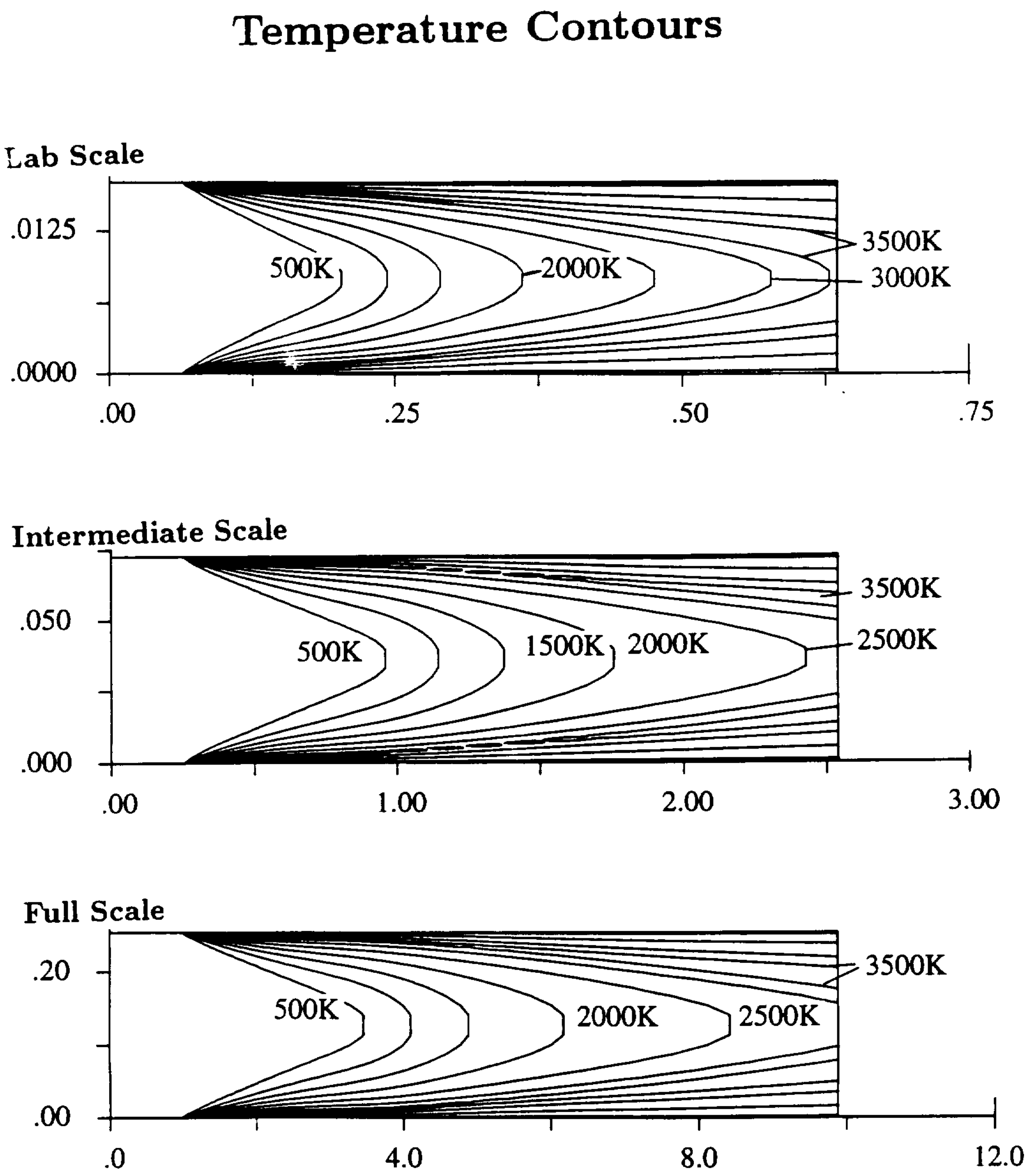

Figure II.6.3 Temperature contours for the lab scale, intermediate and full-scale configurations. In all cases, $G = 565 kg/m^2 - s$ (or $0.18 lbs/in^2 - s$), P=60 atm, L/D=35.

63

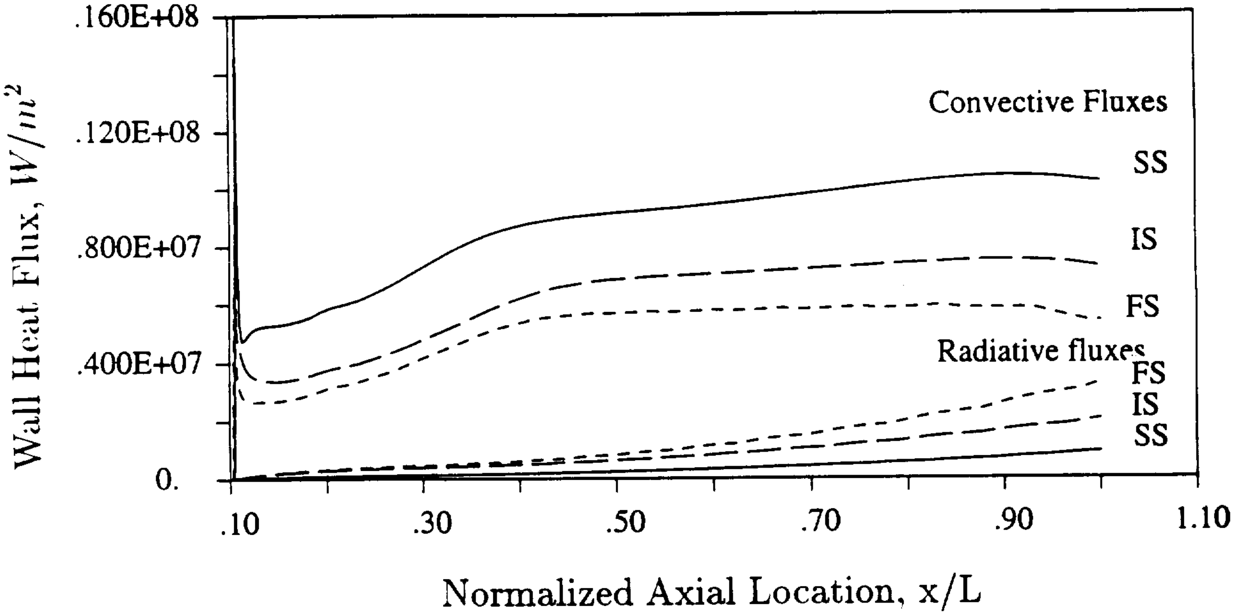

Figure II.6.4 Convective and radiative fluxes for the lab-scale (SS), intermediate (IS) andfull-scale (FS) configurations.

on the fuel surface, and so has the strongest imact on the regression rate. The boundary layer approximation indicates that the convective heat flux depends only on G. This implies that the convective flux would be independent of scale and therefore the 'non-dimensional' (x/D vs. r/D) characteristics of the diffusion flame in different motor sizes should be similar. The temperature contours on Fig. II.6.3 have already shown that the temperature fields are not similar. However, assuming that the temperature fields were similar in non-dimensional space, the non-dimensional temperature gradient would be the same, but the corresponding dimensional temeprature gradient would decrease linearly with motor size. Hence, the convective heat flux at the surface would be smaller for larger motors and would result in lower regression rates in larger motors.

This effect can be clarified by looking at the temperature profiles at a given normalized location ($x/L = 0.5$) in the three different-sized motors. Figure II.6.5 shows the temperature profile at this location versus the normalized distance from the wall, y/D. The three temperature profiles are similar in shape, but the non-dimensional location of the flame is different for the three sizes as was noted in Fig. II.6.3. Consequently, it is clear that the flame location does not scale with motor size. The flame in the lab-scale is located the farthest from the wall in a non-dimensional sense. this is in agreement with our earlier observations.

The convective heat flux to the wall, however, depends on the dimensional (i.e., physical) temperature gradient and not on the non-dimensional temperature gradient. Accordingly, in Fig. II.6.6, we present the same temperature profiles as a function of the physical distance from the fuel surface. These results immediately show that the full-scale configuration has a relatively shallow temerpature gradient at the wall (the flame isfarthest from the wall), while the lab-scale configuration has the steepest gradient (the flame is closest to the wall). Thus, the convective heat flux decreases with increasing motor size as noted in Fig. II.6.4 and the lab-scale motor has the highest regression rate and the full-scale motor has the slowest regression. Overall, the flame location is neither the same in non-dimensional space nor in dimensional space. Its actual location lies between these two extremes, and the 'compromise' results in the size scaling effects that were observed.

The convective heat flux, however, does not represent the total heat flux to the wall. Even though convection is dominant, the radiative heat flux also impacts size scale-up and, as noted earlier, it scales oppositely to the convective flux. As size increases, the radiative component increases so that it becomes more significant in larger motors. This effect

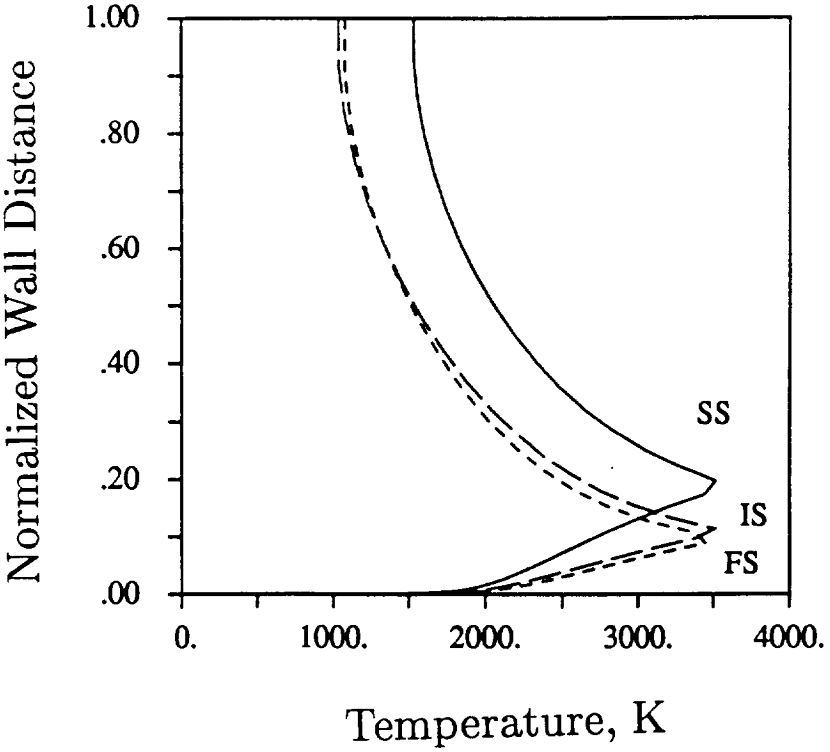

Figure II.6.5 Temperature profiles vs. normalized distance from the fuel surface for the lab-scale (SS). intermediate (IS) and full-scale (FS) configurations.

6.5

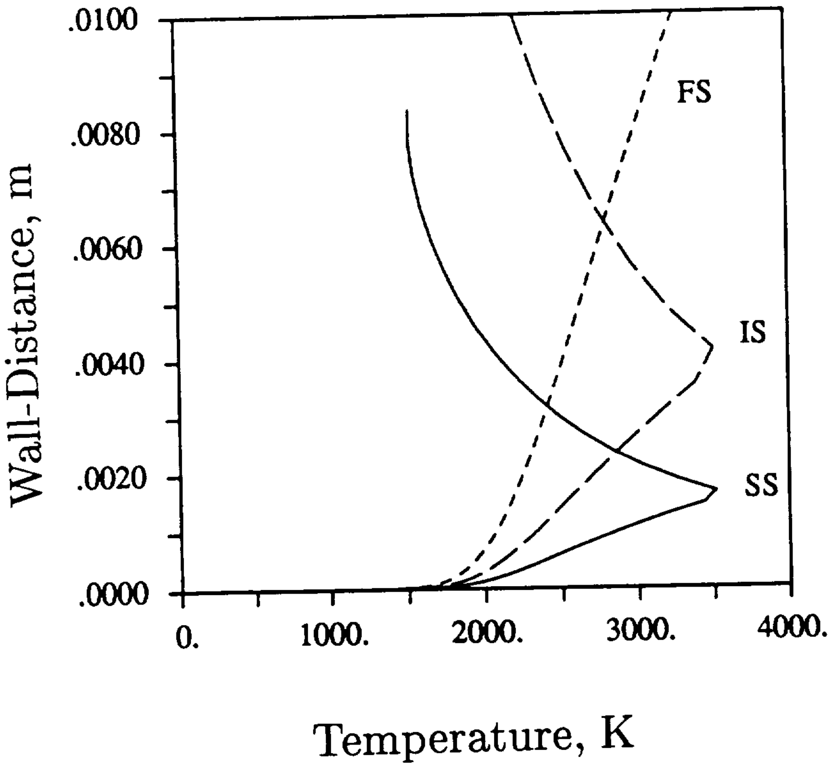

Figure II.6.6 Temperature profiles vs. actual physical distance from the fuel surface for the lab-scale (SS), intermediate (IS) and full-scale (FS) configurations.

66

thus acts to counteract the reduction in regression rate caused by the convective effects. Without radiation, the results in Figs. II.6.1 and II.6.2 would decrease considerably more rapidly with motor size.

The reason that the radiation increases with size is because it has been modelled in the present computations as a volumetric source, whose contribution depends on th volume-to-surface ratio. Larger motors, which have larger volume-to-surface ratios, will therefore have larger radiative fluxes. Further, the radiative flux is also controlled by the temperature field, which we have seen is dependent on the size to a certain extent. In terms of the percent contribution that radiation makes to the total energy budget, we note that it is less than 10% for the lab-scale and it grows to more than 30% for the full scale. It may be anticipated that, using this model, radiation would eventually become the dminant heat transfer mode.

The strict scaling of radiation with volume must, however, be treated with some caution. The approximation is only valid in optically thin or non-participating media. Alternately, if radiation were modelled using the optically thick approximation, the radiative transfer becomes a diffusion-like term. In the optically thick limit, the radiative contribution would then decrease with increasing size like the convective flux. However, this model is not appropriate since it is unlikely that the entire gaseous medium is optically thick. In practice, most of the medium is likely to be optically thin with small embedded optically thick regions. The latter would probably be due to the presence of soot in the flame. In that situation, radiation would be a volumetric term over most of the flowfield and a diffusive term in the 'sooty' regions of the flame. In this regard, the present results, wherein the radiation is treated entirely as a volumetric source, probably overestimate the impact of radiation at the larger sizes. In that case, the actual decrease in regression rate with increasing motor size is likely to be even larger than that shown in Figs. II.6.1 and II.6.2. The present model is capable of representing radiative effects only in a qualitative fashion. For more precise estimates, improved modeling of radiative properties, including soot concentrations, would be necessary.

II.7 CONCLUSIONS

In the theoretical portion of this study, a comprehensive computational model of hybrid combustion has been developed and applied to study parametric characterization of the fuel regression rate and effects of size scale-up and geometric configuration. The analysis has been closely integrated with the experimental study reported in Part I. Experimental measurements of the instantaneous and averaged local regression rate have been used to calibrate as well as verify the computational model. The validated model is then used to evaluate the effects of going from a planar to an axisymmetric configuration and scale-up from lab-scale geometries to full-scale thruster sizes. The computational studies reveal that the surface regression rate is determined by the heat flux to the fuel surface and is a complicated function of flow rate, configuration size and shape. Simplified boundary layer analyses fail to address these issues properly, thereby necessitating a comprehensive analysis such as the present one.

The computational model is based upon the full unsteady Navier-Stokes equations with additional transport equations for chemical species and turbulence. The model is capable of analyzing quasi-steady flowfields to assess regression rates and combustion efficiencies as well as unsteady flowfields necessary for combustion instability studies. The gas-phase equations are solved coupled to the solid fuel-phase using interfacial balances of mass and energy. Solid-phase pyrolysis is represented by an Arrhenius expression suggested by Brill *et al.* [16] for HTPB fuel. Gas-phase combustion is treated by means of a two-step global combustion model in the current study. Turbulence is handled by the standard $k-\epsilon$ turbulence model. Radiative transfer is treated in phenomenological fashion by means of a simple emission model. The radiative absorption coefficient is obtained by calibrating the computational results against the experimental data.

Detailed computations of several of the experimental test cases have been performed and comparisons of the instantaneous and averaged regression rates have been carried out. In all cases, very good general agreement is obtained. In particular, the regression rate dependence on the flow rate is well-captured. Further, the model indicates that radiation is important at low flow rates, while it becomes negligible at higher flow rates. These trends are in good qualitative agreement with estimates of radiative contribution obtained from experimental correlations developed in Part I of this study. Additional comparisons with test data from the General Dynamics-Thiokol-Rocketdyne sub-scale tests [1] and the JPL tests [3,4] also indicate good general agreement.

Both the experimental and computational results point to the inadequacy of boundary layer correlations to determine regression rate. Experimental correlations developed in Part I of this report demonstrate that it is not possible, in general, to fit the experimental data to a correlation of the form $r_b \approx G^n$. The computations likewise reveal that the the hybrid combustor flowfield develops very rapidly and resembles a boundary layer only near the leading edge of the fuel slab. This is due to strong local acceleration of the core gases and diffusive and radiative effects from the flame.

The computational model has been applied to address size scale-up issues on hybrid rocket motors. These studies enable us to determine the critical issues in extending small-scale test results to full-size thrusters. The results indicate that large chambers regress more slowly than smaller ones because the size scaling changes the location of the flame with respect to the fuel surface. The flame location causes the convective heat fluxes to decrease resulting in slower regression rates. Radiative heat transfer tends to offset this decrease, but since convective fluxes dominate the radiative fluxes, the former still control the problem. However, the increased importance of radiation in larger size motors may point to the need for more detailed radiative transfer modeling. Computational studies of planar and axisymmetric hybrid combustor configurations likewise show that the regression rate is influenced by the geometrical configuration as well.

The present study has been useful in ascertaining the controlling issues for sub-scale and full-scale hybrid motors. The computational model has been validated and tested for hybrid rocket flowfields. It should prove useful as the basis for future development work, particularly in the area of studying more practical hybrid configurations, such as wagon-wheel type fuel grains. Computational analysis would be a useful tool for obtaining design estimates of regression rate and combustion efficiency for full-scale thruster configurations. Furthermore, the present model is capable of solving unsteady problems and would be a suitable tool for the analyses of combustion instability issues in hybrid rocket motors.

REFERENCES

[1] General Dynamics-Thiokol-Rocketdyne, "Hybrid Propulsion Technology," Final Report. NASA CR 183972-183973-183974-183975, November, 1989.

[2] Boardman, T. A., Carpenter, R. L., Goldberg, B. E. and Shaeffer, C. W., "Development and Testing of 11- and 24-Inch Hybrid Motors Under the Joint Government/Industry IR&D Program," AIAA 93-2552, 29th Joint Propulsion Conference, June, 1993, Monterey, CA.

[3] Strand, L. D., Ray, R. L. and Cohen, N. S., "Hybrid Rocket Combustion Study,"

AIAA 93-2412, 29th Joint Propulsion Conference. June. 1993, Monterey, CA.

[4] Strand. L. D.. Jones. M. D.. Ray, R. L. and Cohen. N. S., "Characterization of Hybrid Rocket Internal Heat Flux and HTPB Fuel Pyrolysis," AIAA 94-2876, 30th Joint Propulsion Conference. June. 1994, Indianapolis. IN.

[5] Lengelle. G., Fourest. B., Godon. J. C. and Guin. C., "Condensed Phase Behaviour and Ablation Rate of Fuels for Hybrid Propulsion," AIAA 93-2413, 29th Joint Propulsion Conference, Monterey, CA.

[6] Carpenter, R.L., Boardman, T.A., and Claflin, S.E., "Hybrid Propulsion for Launch Vehicle Boosters: A Program Status Update," AIAA Paper 95-2688, 31st AIAA/ASME/SAE/ASEE Joint Propulsion Conference and Exhibit, July 1995.

[7] Sutton, G. P., Rocket Propulsion Elements, 6th edition, New York, Wiley, 1992.

[8] Jarymowycz, T. A., Yang, V. and Kuo, K. K., "A Numerical Study of Solid Fuel Combustion under Supersonic Crossflows," AIAA 90-2076, 26th Joint Propulsion Conference, Orlando, FL.

[9] Cheng, G. C., Farmer, R. C., Jones, H. S. and McFarlane, J .S. "Numerical Simulation of the Internal Ballistics of a Hybrid Rocket Motor," AIAA 94-0554, 32nd Aerospace Sciences Meeting and Exhibit, January, 1994, Reno, NV.

[10] Loh, H. T. and Golafshani, M. , "Computation of Viscous, Chemically Reacting Flows in Hybrids Rocket Motors using an Upwind LU-SSOR Scheme," AIAA Paper 90-1570, AIAA 21st Fluid Dynamics, Plasma Dynamics and Lasers Conference, June, 1990.

[11] Westbrook, C. K. and Dryer, F. L., "Simplified Reaction Mechanisms for the Oxidation of Hydrocrabon Fuels in Flames," *Combustion Science and Technology*, 27, pp. 31-43.

[12] Jones, W. P. and Lauder, B. E., "The Prediction of Laminarization with a Two-Equation Model of Turbulence," International Journal of Heat and Mass Transfer, Vol .15, pp. 301-314.

[13] Chien, K. "Predictions ofChannel and Boundary Layer Flows with a Low Reynolds Number Model turbulence Model," *AIAA Journal*, Vol. 20, No. 1, pp. 33-38.

[14] Sigel, R. and Howell, J. R., Thermal Radiation Heat Transfer, 3rd edition, Hemisphere Publishing Corporation, 1992.

[15] Cohen, N. S., Fleming, R. W. and Derr, R. L., "Role of Binders in Solid Propellant Combustion," AIAA Journal, Vol. 12, No. 2, pp. 212-218.

[16] Arisawa. H. and Brill. T. B., "Flash Pyrolysis of Hydroxyl-Terminated Polybutadienne

(HTPB) II: Implications of the Kinetics to Combustion of Organic Polymers," submitted to Combustion and Flame.

[17] Choi, Y-H. and Merkle, C. L.,"The Application of Preconditioning to Viscous Flows," Journal of Computational Physics, Vol. 105, 1993, pp. 207- 223.

[18] Venkateswaran, S., Deshpande, M. and Merkle, C. L., "The Application of Preconditioning to Reacting Flow Computations," 12th AIAA CFD Conference, June, 1995, San Diego, CA.

REPORT DOCUMENTATION PAGE

Form Approved
OMB NO. 0704-0188

1. AGENCY USE ONLY *(Leave blank)*

2. REPORT DATE
July 1996

3. REPORT TYPE AND DATES COVERED
Final Report (4/1/94 - 6/30/96)

4. TITLE AND SUBTITLE
Fundamental Phenomena on Fuel Decomposition and Boundary-Layered Combustion Processes with Applications to Hybrid Rocket Motors

5. FUNDING NUMBERS
Contract No: NAS8-39945

6. AUTHOR(S)
Part I: Kenneth K. Kuo, Yeu-Cherng Lu, Martin J. Chiaverini, David K. Johnson, Nadir Serin, and Grant A. Risha
Part II: Charles L. Merkle and Sankaran Venkateswaran

7. PERFORMING ORGANIZATION NAMES(S) AND ADDRESS(ES)
The Pennsylvania State University
140 Research Building East
University Park, PA 16802-2320

8. PERFORMING ORGANIZATION REPORT NUMBER

9. SPONSORING / MONITORING AGENCY NAME(S) AND ADDRESS(ES)
NASA/Marshall Space Flight Center
Marshall Space Flight Center, AL 35812

10. SPONSORING / MONITORING AGENCY REPORT NUMBER

11. SUPPLEMENTARY NOTES
The views, opinions and/or findings contained in this report are those of the author(s) and should not be construed as an official NASA/MSFC position, policy or decision, unless so designated by other documentation.

12a. DISTRIBUTION / AVAILABILITY STATEMENT
Approved for public release; distribution unlimited.

12 b. DISTRIBUTION CODE
NASA

13. ABSTRACT *(Maximum 200 words)*

This final report summarizes the major findings obtained from the NASA Contract NAS8–39945 on the subject of "Fundamental Phenomena on Fuel Decomposition and Boundary–Layer Combustion Processes with Applications to Hybrid Rocket Motors", performed from 1 April 1994 to 30 June 1996. Both experimental results from Task I and theoretical/numerical results from Task II are reported here in two parts. Part I covers the experimental work performed and describes the test facility setup, data reduction techniques employed, and results of the test firings, including effects of operating conditions and fuel additives on solid fuel regression rate and thermal profiles of the condensed phase. Part II concerns the theoretical/numerical work. It covers physical modeling of the combustion processes including gas/surface coupling, and radiation effect on regression rate. The numerical solution of the flowfield structure and condensed phase regression behavior are presented. Experimental data from the test firings were used for numerical model validation.

14. SUBJECT TERMS
Hybrid rocket propulsion; regression rate; x-ray radiography; ultrasonic pulse echo; reacting boundary layer; solid fuel; HTPB; gaseous oxygen; experimental; numerical; surface temperature; combustion; pyrolysis

15. NUMBER IF PAGES
168

16. PRICE CODE

17. SECURITY CLASSIFICATION OR REPORT	18. SECURITY CLASSIFICATION OF THIS PAGE	19. SECURITY CLASSIFICATION OF ABSTRACT	20. LIMITATION OF ABSTRACT
UNCLASSIFIED	UNCLASSIFIED	UNCLASSIFIED	UL